NUMERICAL INVESTIGATION ON HEAT TRANSFER CHARACTERISTICS IN CORRUGATED TUBE WITH TAPERED TWISTED TAPE INSERT
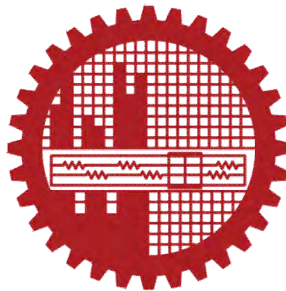
by

Sadman Hassan Labib

A thesis has been submitted in partial fulfillment of the requirement for the degree of

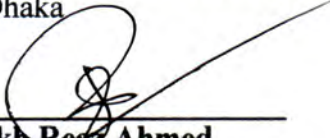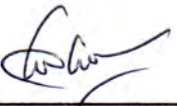MASTER OF SCIENCE IN MECHANICAL ENGINEERING

Department of Mechanical Engineering

BANGLADESH UNIVERSITY OF ENGINEERING AND TECHNOLOGY

July 2021

I

The thesis titled **"Numerical Investigation on Heat Transfer Characteristics in Corrugated Tube with Tapered Twisted Tape Insert"** submitted by **Sadman Hassan Labib**, Roll No.: **1017102039 P**, Session: **October 2017** has been accepted as satisfactory in partial fulfillment of the requirement for the degree of **Master of Science in Mechanical Engineering** on **25 July 2021**.

BOARD OF EXAMINERS

Dr. Mohammad Nasim Hasan
Professor
Department of Mechanical Engineering
BUET, Dhaka

Chairman

(Supervisor)

Dr. Shaikh Reaz Ahmed
Professor and Head
Department of Mechanical Engineering
BUET, Dhaka

Member

(Ex-officio)

Dr. Mohammad Arif Hasan Mamun
Professor
Department of Mechanical Engineering
BUET, Dhaka

Member

Dr. Mohammad Mamun
Professor
Department of Mechanical Engineering
BUET, Dhaka

Member

Dr. A.T.M. Hasan Zobeyer
Professor and Head
Department of Water Resources Engineering
BUET, Dhaka

Member

(External)

CANDIDATE'S DECLARATION

It is hereby declared that this thesis or any portion of the work contained in this thesis has not been submitted in support of an application for another degree or qualification of this for any other University or Institution of learning.

_____

July 2021   **Sadman Hassan Labib**

CERTIFICATE OF RESEARCH

This is to certify that the work presented in this thesis has been carried out by the author under the supervision of **Dr. Mohammad Nasim Hasan**, Professor, Department of Mechanical Engineering, Bangladesh University of Engineering and Technology, Dhaka.

_____   _____

Dr. Mohammad Nasim Hasan   **Sadman Hassan Labib**

ACKNOWLEDGEMENTS

ABSTRACT

A numerical investigation has been carried out to study the combined effect of insertion of the tapered twisted tapes inside the helically outward corrugated tubes as a compound method, on the heat transfer augmentation, pressure drop characteristics, flow behavior, and overall performance of a heat exchanger, for turbulent flow. A 3-D computational model has been developed with the SST k-ω turbulence model, from a comparative study among four different turbulence models against standard empirical correlations. In addition, reported literature discretely asserted the model for the twisted tape inserts and the corrugated tubes. In the present study, the turbulent flow, Reynolds number ranging from 3400 to 21000, inside the straight circular tube (SCT), and the helically outward corrugated tubes (HCT) with two different pitch-length-to-tube-diameter ratios (pl/D = 1 and 1.5), and two different height-length-to-tube-diameter ratios (Hl/D = 0.05 and 0.1), inserted with tapered twisted tapes at two different twist ratios (y/w = 3.5 and 5) and three different tapered angles (θ = 0°, 0.3°, and 0.5°), have been investigated for a constant heat flux. It has been found from the present study that the heat transfer rate enhanced with the decrease of twist ratio, and the pressure drop decreased significantly with the increase of tapered angle. In addition, the corrugated tube with lower (pl/D) and (Hl/D), has been exhibited a higher heat transfer rate compared to other investigated tubes.

Moreover, an Artificial Neural Network (ANN) model has been developed to predict the Nusselt number, normalized Nusselt number, friction factor, normalized friction factor, and the thermal performance factor for the helically corrugated tubes with the pitch-length-to-tube-diameter ratio of 0-1.5, and the height-length-to-tube-diameter ratio of 0-0.1. The predicted values of the performance factors from the trained artificial neural network (ANN) are in good agreement with the results of the computational investigation, with error bands of 2%, 2%, 1%, 1%, and 1% for the Nusselt number, friction factor, normalized Nusselt number, normalized friction factor, and thermal performance factor, respectively. The modeled (ANN) consequently obtained correlations for Nusselt number, friction factor, and thermal performance factor, which have been exhibited ±4%, ±5%, and ±5% error bands respectively, against the computationally analyzed Nusselt number, friction factor, and thermal performance factor. Finally, the results from the numerical study and the artificial neural network predictions, have been revealed that the tapered twisted tape insert (y/w = 3.5 and θ = 0.5°) inserted in the helically corrugated tube (Hl/D = 0.1, pl/D = 1.0) yields better thermal performance factor compared to other investigated cases.

TABLE OF CONTENTS

LIST OF FIGURES

XI

LIST OF TABLES

NOMENCLATURE

A surface area, m^2

D diameter, m

L length of tube, m

Q heat transfer rate, W

V velocity

C_p specific heat of fluid, J/kg-K

T temperature, K

h heat transfer coefficient, W/m^2-K

k thermal conductivity, W/m-K

Re Reynolds number

Nu Nusselt number

Pr Prandtl number

f friction factor

y pitch length of twisted tape, m

w width of the twisted tape, m

pl pitch length of corrugated tube, m

Hl height length of corrugation, m

Greek symbols

ΔP pressure difference across test section, Pa

η thermal performance factor

Subscripts

o   outlet

i   inlet

w   wall

b   bulk

t   turbulent

CHAPTER 1

Introduction

Scientists and researchers have taken a keen interest in the modification of heat-exchanging devices. The reason behind this is that it has broad applications in daily life and industries [1]. Shell and tube heat exchangers, boilers, condensers, radiators, heaters, furnaces, cooling towers, solar collectors, heating, ventilation, and air conditioning (HVAC) equipment and refrigerators [2] are using as heat-exchanging devices. Automotive industries, petrochemical industries [3], aerospace industries [4], and chemical industries [5] are prime beneficiaries of heat exchangers. Every industry, small or large, has heat transfer processes for various operations. The use of heat transfer enhancement techniques makes the heat exchangers more compact and efficient, but at the same time cost increases proportionally. The viable adaptation of heat exchangers is the hotspot for the last three decades. Fig. 1.1 depicts the installed heat exchangers in a power plant.

Source: https://www.sacome.com/en/tubular-heat-exchangers/

Fig. 1.1: Heat exchanger installed at a power plant.

1.1 Enhancement of Heat transfer in the Heat exchanger

Heat transfer enhancement is a process of increasing the heat transfer rate and the thermo-hydraulic performance of a system using various methods. The methods of heat transfer enhancement are employed for increasing the heat transfer without affecting the overall realization of the systems significantly.

Heat transfer enhancement methods exist on three general classifications which are active, passive and compound methods. Active methods require external power to input the process; in contrast, passive methods do not require any additional energy to improve the thermohydraulic performance of the system. Also, two or more passive and active techniques can be used together and that is called compound technique, which is employed to produce a higher augmentation than using one passive or active technique independently [6].

1.1.1 Active Method

The methods of heat transfer enhancement that require an external power supply to maintain the enhancement mechanism are named the active method. Examples of the active method are given as follows:

1.1.1.1 Mechanical Aids

Equipment with a rotating heat exchanger tube is found in commercial practice. They involve gripping the fluid by mechanical means or spin the surface. Mechanical surface scrapers can be applied to the tube flow of gases and viscous liquids in the chemical process industry. Fig. 1.1.1.1 shows a surface scraped heat exchanger.
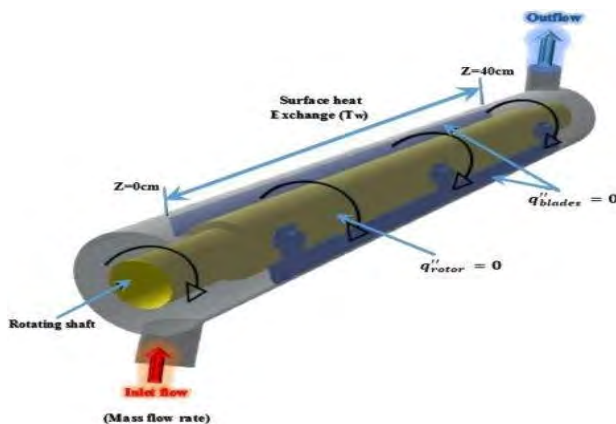
Fig. 1.1.1.1: An illustration of a Surface Scraped Heat Exchanger.

1.1.1.2 Spray

Spray is another active method of heat transfer enhancement used in metal production and processing industries. Usually, the spray is defined as the liquid droplets which are generated by a pressure-assisted atomizer. These droplets spread over the heated surface and evaporate, or form a thin film of liquid impinging on the hot surface. The heated surface gets cooled by the droplets because the droplets are rapidly expelling over the surface. The large surface area of small droplets in contact with the unsaturated ambient air promotes evaporation. As a result, the high latent heat is absorbed from the heated wall by the water drops during evaporation, shown in Fig. 1.1.1.2. Besides, convection heat transfer is increased because droplets act on the liquid film thus mixing the fluid better. When the liquid near the heating wall becomes superheated, heat transfer may be increased by secondary nucleation or boiling which increases the heat transfer coefficient, the evaporation rate, and the turbulence. Spray cooling is very difficult because it depends on many parameters i.e., nozzle-to-heating surface distance, incident angle, droplet size, air pressure, droplet velocity, droplet density, surface roughness and orientation, air pressure, etc.
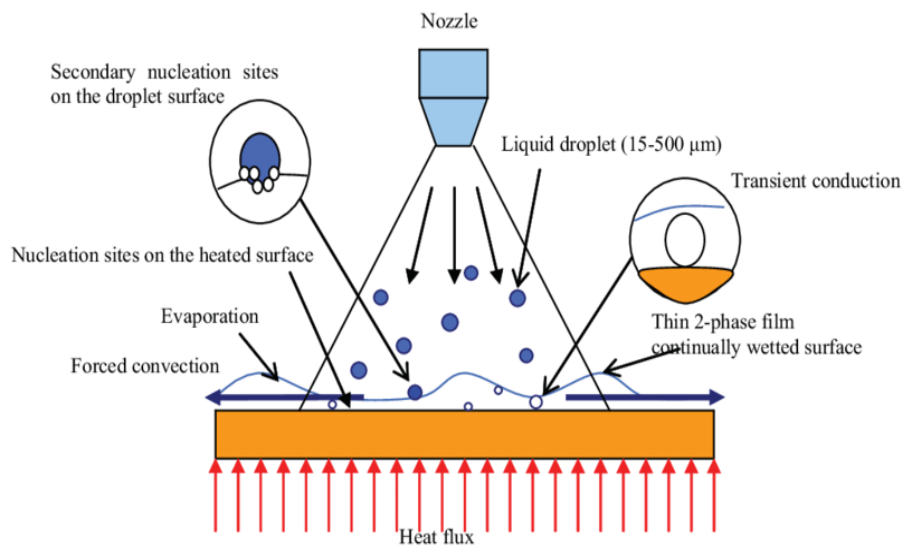
Fig. 1.1.1.2: Heat transfer mechanism by spray cooling.

1.1.1.3 Surface/Fluid Vibration

Surface/fluid vibration is used as an active heat transfer enhancement method in recent technologies as it can achieve a high cooling rate. Sufficiently intense oscillations can improve heat transfer in liquids both by applying surface vibration usually lower than 1000 Hz or inducing

vibration in the fluid itself. The two mechanisms operate quite differently. The vibration of a surface obtained by an electro-dynamic vibrator or a motor-driven eccentric mainly breaks the boundary layer, moving the particles of the fluid in the vicinity of the surface. This can induce "forced" convection in a region otherwise of free convection.

1.1.1.4 Jet Impingement

Jet impingement is used as an active method for heat transfer enhancement. It forces a single-phase fluid flow normally or obliquely towards a surface. Increased projection of the high-velocity fluid has increased the heat transfer coefficient, which eventually enhances the heat transfer. Jet provides a higher heat transfer rate at the stagnation point, see Fig. 1.1.1.4. Jets are used in many industrial applications thermal control of high flux devices such as electronics, X-rays, optics, gas turbines, cooling of internal combustion engines. To cool the surface uniformly and widely, multiple jet impingements are used. Multiple jets enhance heat transfer in many ways. The heat transfer coefficient is greatly high near the impingement zone. Thus, increasing the number of impingement zones improves heat transfer.
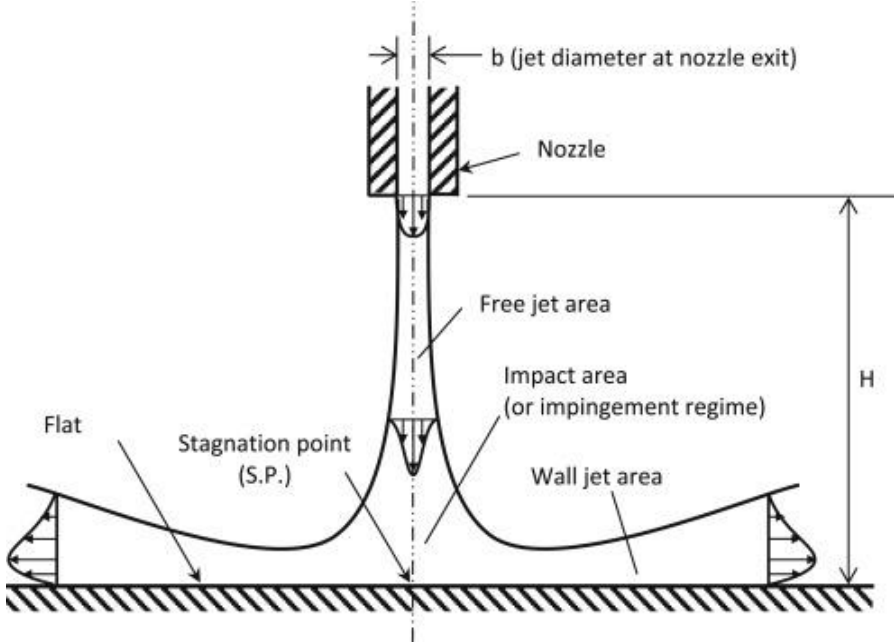
Fig. 1.1.1.4: Heat transfer by Jet impingement.

1.1.2 Passive Method

The passive method of heat transfer enhancement does not require any external power to maintain the enhancement mechanism. In contrast, the geometry or the surface of the flow channel is modified to increase the thermo-hydraulic performance of the system. These modifications are utilized to promote fluid mixing and turbulence in the flow, which results in an increment of the overall heat transfer rate. Passive techniques have also some advantages concerning the other heat transfer enhancement techniques such as low cost, easy production, and installation. Examples of the passive method are given as follows:

1.1.2.1 Extended Surface

The heat conducted through solids, walls, or boundaries, has to be continuously dissipated to the surroundings or environment to maintain the system in steady-state conduction. In many engineering applications, large quantities of heat need to be dissipated from small areas. Heat transfer by convection between a surface and the fluid surroundings can be increased by attaching thin strips of metals called fins to the surface. The fins increase the effective area of the surface, thereby increasing the heat transfer by convection. The fins are also referred to as "extended surfaces". Extended surfaces (fins) are one of the passive methods that are employed extensively to increase heat transfer rates. The rate of heat transfer depends on the surface area of the fin. It increases the contact surface area, for example, a finned tube, see Fig. 1.1.2.1.

Fig. 1.1.2.1: Extruded high finned Copper tube.

1.1.2.2 Treated Surface

The surface with pits, cavities, or scratches, is known as the treated surface. Treated surfaces are primarily used for boiling and condensing duties. In enhanced boiling, treated surfaces provide a large number of stable vapor traps or nucleation sites on the surface for bubble formation. In the case of highly wetting fluids like refrigerants, organic liquids, cryogens, and alkali liquid metals, the normal cavities present on the heated surfaces tend to experience sub-cooled liquid flooding. For high surface tension fluids, coatings of non-wetting material such as Teflon on either the heated surface or its pits and cavities are effective in nucleate boiling. In the condensation of vapor, treated surfaces promote drop-wise condensation which is ideal for preventing surface wetting and break up the condensate film into droplets. This process provides better drainage and a more effective removal of vapor at the cold heat transfer interface.

1.1.2.3 Inserts

Inserts are one of the popular passive heat transfer enhancement methods because of their low manufacturing cost. The types of inserts are twisted tape, wire coils, ribs or corrugated tubes, baffles, plates, helical screw inserts, mesh inserts, convergent-divergent conical rings, winglets, etc., see Fig. 1.1.2.3. Twisted tapes are metallic strips twisted using some of the suitable techniques as per the required shape and dimension, which are inserted in the flow to enhance the heat transfer. The twisted tape inserts are most suitable and widely used in heat exchangers to enhance heat transfer. Wire coil inserts have been utilized as one of the passive enhancement methods and are widely utilized in heat transfer equipment. Corrugated tube is another passive heat transfer enhancement method used in heat exchangers. The converging-diverging area along the flow path helps in better mixing of fluids at the core and the annuli, which results in higher heat transfer. Baffles are also used for better mixing of working fluid in the heat exchanger. In addition, these inserts are working as turbulator which induce turbulence in the fluid flow. Changing different geometric parameters such as twist ratio, tapered angle, and several channels for twisted tape inserts; corrugation pitch length, corrugation height for the corrugated tubes, researchers are working to figure out optimized designs of these inserts.
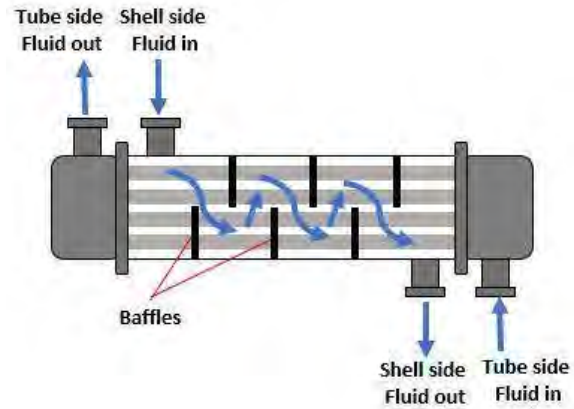
| (a) Twisted Tape | (b) Baffles |

| (c) Corrugated Tubes | (d) Wire coil |

Fig. 1.1.2.3: Illustrations of different types of inserts.

1.1.3 Compound Method

A compound method is the combination of more than one heat transfer enhancement method (active and/or passive) to increase the thermo-hydraulic performance of heat exchangers. It can be employed simultaneously to generate an augmentation that promotes the performance of the system either of the techniques operating independently. Preliminary studies on the compound augmentation techniques of this kind are quite encouraging.

1.2 Motivation for the Present Study

Enhancement methods that have been used for the enhancement of convective heat transfer are upgraded according to technological developments. The first-generation heat transfer methods commonly used bare tubes, the second generation progressed to plain fins, the third generation shifted to vortex generators, and the fourth generation has moved to the compound heat transfer enhancement method [7].

A good number of researchers focused their studies on heat transfer enhancement and fluid friction behavior of circular tubes fitted with various designs of twisted tapes. Straight twisted tape enhances the heat transfer rates by fluid flow swirling caused by the generated centrifugal forces, but with a considerable penalty on pressure loss and the cost of higher pumping power [8,9]. Hence, it is required to optimize the design of the twisted tape.

At present, corrugated tubes of different flow channels are widely used in the industries. Corrugated tubes disturb and reform the flow boundary layer along the flow path which leads to a higher heat transfer rate. Easier fabrication, greater enhancement in thermal performance, and limited increase in flow resistance, over other types of modified surface tubes make the corrugated tube an effective and efficient choice for the researchers. Moreover, researchers are more focused to figure out the optimized design of corrugated tubes. Fig. 1.2, shows the distribution of recent trends of investigation on the different flow channels of corrugated tubes [10].

There have been extensive studies on different twisted tape inserts, and also on different corrugated tubes. The present study introduces a compound enhancement method incorporating two passive methods by inserting tapered twisted tape with different twist ratios and tapered angles inside the helically outward corrugated tubes with different pitch-to-diameter ratios and height-to-diameter ratios to apprehend the heat transfer enhancement in tubular heat exchanger for turbulent flow.
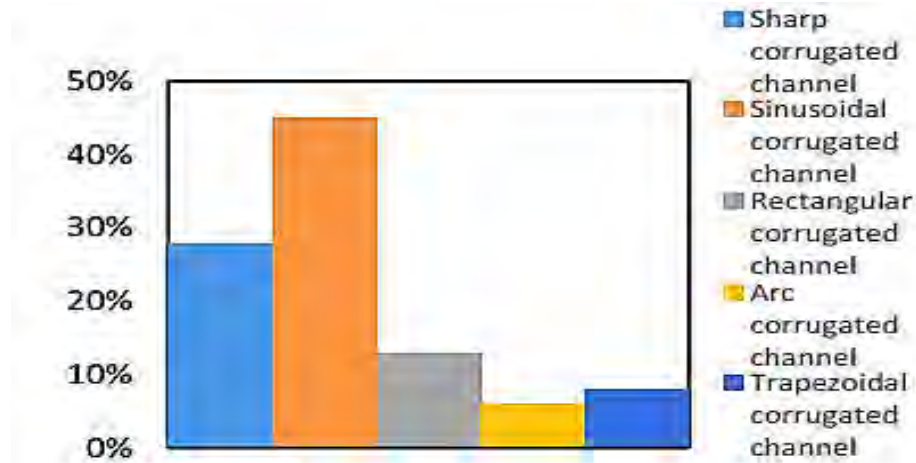
Fig. 1.2: The distribution of recent trends on investigated channels' percentage [7].

1.3 Objectives of the Present Study

The specific objectives of this present study are as follows:

a) To develop a computational model to demonstrate the turbulent heat transfer process through the straight circular tube, and the helically corrugated tubes.

b) To do verification and validation of the developed model through comparison with other model results as well as relevant experimental work.

c) To analyze the effect of the tapered twisted tape inserts of different twist ratios and tapered angles in heat transfer enhancement, and pressure drop, over the conventional twisted tape inserts, both are fitted in the straight circular tube and the corrugated tubes with different pitch-length to diameter ratios and height-length to diameter ratios.

d) To evaluate the thermal performance factor combining the effect of enhanced heat transfer and pressure drop, for the above-mentioned cases to get the optimum passive heat transfer augmentation technique.

In addition, the present study aims to train an Artificial Neural Network (ANN) model with the obtained results from the CFD study to get insight into the effect of different geometric configurations of the model on the performance parameters. Besides, to obtain correlations to determine the Nusselt number, the friction factor, and the thermal performance factor for the developed CFD model, for a wide range of design parameters by applying ANN.

1.4 Thesis outline

The present thesis conducts a numerical investigation, assessing the overall performance characteristics of a heat exchanger adopting a compound heat transfer enhancement technique incorporated with corrugated tubes and twisted tape inserts. An outline of this thesis is presented below,

Chapter- 1: Introduction – a discussion about the key elements of this research, the motivation behind this research work, and research objectives.

Chapter- 2: Literature Review – an account of previous research about the computational and experimental study of heat transfer enhancement using different passive techniques.

Chapter-3: Mathematical Background – comprehends the basics of CFD and different turbulence models of CFD.

Chapter- 4: Computational Model – a description of developing a computational model of the present study, solution procedure, validation, and the verification of the developed model.

Chapter- 5: CFD Results – describes the performance characteristics of the developed model and discussion the results of the study.

Chapter-6: Predictive Modeling using Artificial Neural Network – describes previous research employing ANN in predicting thermal equipment, construction of ANN for the present study, and discussions about the predicted results using ANN.

Chapter- 7: Conclusion – summarizes the outcomes of current research and recommending the future scopes of the present study.

CHAPTER 2

Literature Review

For a long period, researchers have been working with passive heat transfer enhancement methods. Since the passive methods are more economical and there are various ways to improve the design and performance of these methods, researchers carried out both experimental and numerical investigations over the passive methods. In this chapter, several recent scientific studies on different passive heat transfer enhancement methods are discussed.

2.1 Study of Heat Transfer Enhancement with Different Passive Methods

Researchers used helical wire coils [11-13], circular discs [14-16], and fins [17-20] as heat transfer enhancement tools inside heat exchangers. Among these researchers, Panahi and Zamzamian [11] experimentally studied a shell and coiled tube heat exchanger is in which a helical wire has been placed inside the helically coiled tube as a turbulator. In their study, they evaluated the thermal and frictional behavior of the coil tube with a turbulator. Besides, they investigated the overall heat transfer coefficient, effectiveness, and NTU of their studied heat exchanger, and found that insertion of turbulator had increased the overall heat transfer coefficient along with the pressure drop.

Feng et *al.* [12] carried out a numerical investigation to study the laminar liquid flow and coupled heat transfer performance in the rectangular microchannel heat sink (MCHS) equipped with wire coil inserts. They considered the distilled water with temperature-dependent thermophysical properties, as the working fluid to perform simulation. According to the first law and the second law of thermodynamics, they studied the MCHSs. For a constant heat flux of 400 kW/m^2, the long wire coil exhibited better heat transfer enhancement among the studied five configurations of MCHS.

Sajadi et *al.* [13] investigated the boiling heat transfer coefficient and pressure drop of R1234yf flow as a replacement refrigerant for R-134a in horizontal plain and wire-coil inserted tubes. In their study, they found that at the optimum vapor quality the heat transfer coefficient increased significantly with both heat flux and mass velocity. On the other hand, the pressure drop increases linearly with the vapor quality of R1234yf. To some extent, inserting a wire-coil in the tube may

enhance the heat transfer coefficient by as much as 72% while leads up to an 85% increment in the pressure drop.

Yan et *al.* [14] presented a numerical systematic comparison of the fluid flow and heat transfer characteristics between standard and cross-drilled ventilated brake discs incorporating pin-fins to find a superior overall cooling performance providing method. Their investigation found that the cross-drilled holes improved the cooling performance of the pin-finned brake disc. The introduction of cross-drilled holes on the rubbing discs enhances the overall cooling capacity of the pin-finned brake disc by 15–17%. As a result of the axial pressure gradient, the low-momentum boundary-layer fluid near the rubbing surfaces is driven into the ventilated channel through the cross-drilled holes. Consequently, within radial spans of the cross-drilled holes, local heat transfer on the rubbing surfaces is improved.

Aziz et *al.* [15] addressed the heat generation/absorption and slip effects on MHD three-dimensional flow of viscous nano-liquid by a rotating disk. The nanofluid model that had been incorporated in their study consisted of Brownian diffusion and thermophoresis. Velocity, temperature, and concentration slip conditions were utilized in their investigation. Besides, they developed a numerical solution for the obtained nonlinear ordinary differential equation using the NDSolve technique.

Capata and Beyene [16] experimentally evaluated three different compacts branched heat exchangers, measuring, for every single device, the thermal efficiency and the pressure drop for different refrigerant fluids. The tested bench that had been used by them, was assembled using a heating plate with a power of 500 W and a submersible pump, needed for the fluid recirculation, coupled with flowmeters, to control the mass flow rate within a specific range. The data was obtained from several comparative tests that had been analyzed, to determine the optimal solution for each refrigerant among the different heat exchangers.

Ahmed [17] carried out an experimental investigation on heat transfer enhancement by inserting porous twisted tape inserts in a circular tube. Mild steel-made twisted tapes had holes of different diameters. Due to the insertion of the turbulator, the heat transfer had enhanced about 5.5 times, and pumping power enhanced around 1.8 times, compared to a bare tube turbulent flow of air.

Ambreen et *al.* [18] investigated the combined influence of pin-fin shape variation and utilization of nanofluid coolants on heat transfer and fluid flow characteristics of a heat sink through the

Lagrangian-Eulerian approach. The results obtained from their study illustrated that utilizing the nanofluid enhanced the heat exchange capacity of the heat sink regardless of the pin-fin configuration. However, an appropriate pin-fin shape can supersede the advantage of employing nanofluid coolants at the studied particle concentration. At the highest pressure drop, the nanofluid-cooled circular, square, and triangular pin-fins demonstrated a maximum average-Nusselt number enhancement of 23.1%, 16.5%, and 8%, respectively, compared with water-cooled triangular pin-fins.

Haque [19] numerically investigated the forced convection heat transfer over circular and oval tube banks consisting of seven rows of tubes in an inline arrangement with rectangular longitudinal vortex generators placed at the bottom of the channel. To understand the characteristics of average Nusselt number, associated pressure drop, friction factor, area goodness factor, streamline distribution, and temperature contours, etc., are studied numerically with the aid of computational fluid dynamics. The heat transfer had enhanced nearly 26%, while the pumping power increased about 69%, for fluid flow in the region from Reynolds number 550 to 1775.

Sadeghianjahromi et al. [20] examined some novel improvements in association with the airside performance of wavy fin-and-tube heat exchangers. The effects of waffle height, adding slits on wavy fins and vortex generators on the thermal resistance of wavy fin-and-tube heat exchangers were investigated in their study. The fabrication method of the helically coiled tube which contains turbulator and also the effects of turbulator on thermal and frictional characteristics of the heat exchanger are presented in this paper.

In a numerical study, Omidi et al. [21] used lobed cross-section helical coils to adopt passive heat transfer enhancement. The study was considered for the laminar flow, where the Reynolds number changed from 1300 to 2500, with a constant wall temperature of 373K. It was found that the helical coil with the maximum number of lobes results in the highest Nusselt number and the lowest friction factor, and thus enhances the rate of heat transfer. Moreover, it was observed that the coil diameter had the greatest effect in comparison to the other geometrical parameters.

Yadav and Sahu [22] investigated the heat transfer from water to air in a double pipe heat exchanger where helical surface discs are used as turbulators with different pipe diameter to disc diameter ratios. They conducted the for three diameter ratios, three-helix angles, and Reynolds number was varied between 3500–10,500. Besides, all the tests were conducted for the constant

wall temperature condition. From the experiments, it was observed that the smallest diameter ratio gives the higher thermal performance for the heat exchanger.

Researchers also investigated the use of nanofluids to enhance the performance of heat exchangers [23-25]. Cui et *al.* [23] investigated a numerical simulation on the flow of nanofluids in a circular tube was carried out. Besides, the simulations have two parts. Firstly, the pressure drop of pure water (single-phase base fluid) flowing in a circular tube was calculated to verify the correctness of the simulation model with experimental results. Secondly, numerical simulations for nanofluids were conducted with consideration of different mass fractions of nanoparticles.

Baba et *al.* [24] reported an experimental study of forced convective heat transfer in a double tube counter-flow heat exchanger with multiple internal longitudinal fins using Fe_3O_4–water nanofluid. The convective heat transfer enhancement and pressure drop were investigated in their study, for the nanofluid flowing in a horizontal circular tube with internal longitudinal fins under turbulent conditions ($5300 < Re < 49,200$) and the volumetric concentration of Fe_3O_4 nanoparticles were in the range of $0 < \varphi < 0.4\%$. The obtained results indicated that the heat transfer rate was 80–90% more in the finned tube heat exchanger compared to the plain tube heat exchanger for the higher volumetric concentration of nanofluid.

The stability, thermophysical properties, heat transfer performance, and possible reduction of the effective area of a shell-and-tube heat exchanger operating with CuO/water nanofluid, were investigated by Said et *al.* [25]. Nanoparticle concentrations of 0.05, 0.1, and 0.3 vol% were used in that investigation. In addition, a theoretical model was also developed along with the experimental study to validate the results. The results showed that the convective heat transfer coefficient obtained in the case of operation with nanofluid was slightly higher compared to the base-fluid for the same fluid inlet temperatures and mass flow rates. Experimental outcomes the conducted study highlighted the improvement of heat transfer due to nanofluids. Overall heat transfer coefficient increased by 7%, convective heat transfer increased by 11.39%, and a reduction in the area of 6.81% was achieved, from that study.

Using the Al_2O_3/water nanofluid, Han et *al.* [26] experimentally found that the heat transfer performance increases with an increase in the nanoparticle concentration in the nanofluid. The experimental setup consisted of a double tube heat exchanger with nanofluids on the cold side which was used in turbulent regime with Reynolds numbers ranging from 20,000 to 60,000.

Results from their study showed that the heat transfer had increased with the increased temperature and volume concentration of nanoparticles.

Ravi et *al.* [27] used the Fe_3O_4/water nanofluid in a heat exchanger along with inserted twisted tapes as the heat transfer enhancement device and found an improved thermal performance from the heat exchanger than a basic heat exchanger without the twisted tapes. The convective heat transfer, friction factor, effectiveness, and the number of transfer units (NTU) of $Fe3O4$/water nanofluids, flow in a double pipe U-bend heat exchanger and with twisted tape inserts were estimated experimentally by them. The experiments were conducted in the Reynolds number range from 16,000 to 32,000, particle volume concentrations range from 0.005% to 0.06%, and twisted tape inserts of $H/D = 10$, 15, and 20 were used. The Nusselt number of nanofluids had increased with the increase of particle volume concentrations and Reynolds number and it further increased with the decrease of twist ratio of the twisted tape inserts.

2.2 Study of Enhanced Heat Transfer Using Twisted Tape Inserts

Extensive studies have been carried out both experimentally and numerically to assess the effectiveness of using twist tapes as a heat transfer enhancement method in a heat exchanger [28-41]. An inserted twisted tape stimulates the fluid transfer between the tube wall and the tube nucleus which improves the mixing of fluid across the cross-section of the tube [29,30] and makes the thickness of the boundary layer thinner [33,34]. These phenomena have made the modified heat exchanger advantageous over the basic heat exchanger with enhanced heat transfer rate and thermal efficiency as reported in the mentioned research papers.

A numerical investigation was conducted by Eiamsa-ard et *al.* [28], using twisted tape inserts with clearance ratios of 0.0, 0.1, 0.2, and 0.3, in a circular tube, where twisted tape inserts with lower clearance ratios resulted in higher heat transfer rate in the heat exchanger. In their study, they evaluated Nusselt number, friction factor, and thermal performance factor, for twisted tapes at two different twist ratios of 2.5 and 5.0. The simulation was conducted to gain an understanding of the physical behavior of the thermal and fluid flow in the tube fitted with loose-fit twisted tape under constant wall temperature conditions in the turbulent flow regime for the Reynolds number ranging from 3000 to 10,000.

Sarada et *al.* [29] obtained an experimental investigation of the augmentation of turbulent flow heat transfer in a horizontal tube through varying width twisted tape inserts with air as the working fluid. To reduce excessive pressure drops associated with full width twisted tape inserts, with a less corresponding reduction in heat transfer coefficients, reduced width twisted tapes of widths ranging from 10 mm to 22 mm, which were lower than the tube inside diameter of 27.5 mm were used, in the conducted study. Experiments were carried out for plain tubes with/without twisted tape inserts at constant wall heat flux and different mass flow rates. The twisted tapes of three different twist ratios (3, 4, and 5) each with five different widths (26-full width, 22, 18, 14, and 10 mm) respectively, were investigated in this study where the Reynolds number was varied from 6000 to 13,500.

Bas and Ozceyhan [31] experimentally assessed the results of the heat transfer rate and pressure drop in a heat exchanger fitted with twisted tapes with a lower clearance ratio of 0.0178 and 0.0357, whilst the twist ratios were 2, 2.5, 3, 3.5, and 4. All these configurations were studied in the range of Reynolds number from 5132 to 24,989. From this study, it was reported that not only the heat transfer rate enhanced with the lower clearance ratio twisted tapes, but the pressure-drop also increased consequently which eventually affect the thermal performance of the heat exchanger. Furthermore, they had developed empirical correlations based on the experimental results, to predict the heat transfer (Nu), friction factor (f), and heat transfer enhancement (ζ).

Eiamsa-ard et *al.* [32] described the heat transfer enhancement attributed to the helically twisted tapes where these tapes were fabricated by twisting a straight tape to form a typical twisted tape then bent the twisted tape into a helical shape in their work. The experiments were performed using HTTs with three twist ratios of 2, 2.5, and 3, three helical pitch ratios of 1, 1.5, and 2 for Reynolds numbers between 6000 and 20,000. They observed in their study that the heat transfer rate and the friction factor had increased as the tape twist ratio and helical pitch ratio were decreased, while the thermal performance showed an opposite trend. The highest thermal performance factor of 1.29 was achieved by utilizing the tape with the largest twist ratio (y/W = 3) and helical pitch ratio (p/D = 2) at Reynolds number of 6000, from their investigations.

Chowdhury [33] conducted a numerical investigation on thermal performance of nanofluid in circular tube coupled with rib and rotating twisted tape inserts. They had found that the internally ribbed circular tube provided nearly 8.4% higher heat transfer rate compared to bare circular tube. In their study, the observed that with higher rotating speed of twisted tape had increased the heat

transfer rate by 13.5% compared to smooth circular tube. Using of nanofluid, had also contributed in enhancing the heat transfer rate by 13.4% compared to water. They concluded that their conducted study was suitable for the lower Reynolds number than the higher Reynolds number.

Ji et *al.* [34] made a comprehensive literature survey on the thermal-hydraulic performance of liquid flow and heat transfer in pipes with internal integral-fins, twisted tape inserts, corrugations, dimples, and compound enhancement techniques. It was found that for turbulent heat transfer the enhancement ratio of experimental Nusselt number over Dittus–Boelter equation for the internal integral-finned tube was generally in the range of 2–4; twisted tape insert was 1.5–6; the corrugated tube was 1.5–4 and the dimpled tube was 1.5–4, including the compound enhancement techniques. Besides, For the twisted tape inserts, the pressure drop was remarkably increased at the turbulent flow, and most of the data have lower efficiency than the other three types of tube, while it was found to be effective in laminar and transition flow and higher viscosity fluid.

Mashoofi et *al.* [35] tried to investigate the ways to reduce the pressure drop and consequently increase the thermal performance enhancement factor (TEF) of a heat exchanger equipped with twisted tapes. In this context, axial perforated twisted tapes (PTTs) with various hole-diameters were used instead of simple twisted tapes (STTs). Experimentally it was found that axially perforated twisted tapes exhibit higher thermal performance than simple twisted tape, for the turbulent fluid flow of Reynolds number ranging from 6000 to 25,000. However, the use of perforated twisted tape led to a reduction in pressure drop and heat transfer rate.

Kunlabud et *al.* [36] numerically studied the heat transfer and the flow behaviors in three-dimensional circular tubes with loose-fit multiple channels twisted tapes. This investigation was carried out for Reynolds numbers ranging from 5,000 to 15,000, by using air as testing fluid. The effects of the multiple channel number (2,3, and 4), clearance ratio (0.00, 0.025, 0.05, and 0.075). As for the performance measuring parameter, the heat transfer enhancement and the flow friction were evaluated. The numerical results indicated that the tubes with loose-fit multiple channels twisted tapes performed higher heat transfer rates than the plain tube. Moreover, the enhanced heat transfer rate is escorted with a larger pressure drop. Both heat transfer and pressure drop increase with increasing multiple channel number and decreasing clearance ratio.

Tushar et *al.* [38] carried out a three-dimensional computational conjugate heat and mass transfer study to investigate the effect of the insert's twist ratio on the heat transfer and fluid flow

performance. This investigation was carried out for airflow at 300K and Reynolds number ranging from 3642 to 21,857 through a tube with a constant wall heat flux of 8000 W/m^2 to investigate the effect of the insert with twist ratio 3.46 and 7.6 on Nusselt number, friction factor, and the thermal performance factor of the tube. From this study, they concluded that the twisted tapes provided better heat transfer enhancement at a relatively lower Reynolds number and twist ratio.

Saysroy and Eiamsa-ard [39] had introduced a multi-channel twisted tape insert as a heat transfer enhancement device in a numerical study. The twisted tapes were varied on a number of channels (2 to 8) and twist ratios (2 to 4) for both laminar and turbulent flow fields. For laminar flow, twisted tape with two channels and a 2.5 twist ratio exhibited better thermal performance, and for the case of turbulent flow, twisted tape with two channels and the twist ratio of 3 resulted in the most enhanced heat transfer rate.

Abolarin et *al.* [40] had explored an experimental analysis to understand the heat transfer and pressure drop characteristic for a heat exchanger using clockwise and counter-clockwise twisted tapes. The tapes were twisted to obtain a twist ratio of 5 and 12 strips were joined longitudinally so that a clockwise direction twisted tape insert was connected to a counter-clockwise direction twisted tape. The assembling was at connection angles of 0°, 30°, and 60°. Water was used as the test fluid and experiments were conducted at constant heat fluxes of 1.35, 2, 3, and 4 kW/m^2 between Reynolds numbers of 300 and 11,404. Comparing the effect of different connection angles, it was found that an increase in connection angle enhanced the heat transfer in the transitional flow regime.

Ramakumar et *al.* [41] numerically investigated the turbulent flow through a smooth tube with twisted tape inserts. In their study, they inserted twisted tapes with the twist ratio of 3.0 and the five different tapered angles i.e., 0.0, 0.3, 0.5, 0.6, and 0.7 degrees. In addition, they conducted their investigation for three different Reynolds numbers in the regime from 8500 to 13500. They concluded that the tapered twisted tape with the tapered angle of 0.5 degree exhibited 17% higher overall enhancement compared to other investigated twisted tapes.

2.3 Study of Enhanced Heat Transfer Using Corrugated Tube

Corrugated tubes, which are representative of second-generation enhanced heat transfer technology, are widely used and investigated owing to their advantages such as easier fabrication, bilateral enhanced heat transfer, and minor pressure drop compared with other special-shaped

pipes. Recently, several studies have considered various factors such as corrugation shapes [42,43], geometrical parameters [44–46], working conditions (Re) [47–50], and fluid properties (Pr) [51], to study the mechanism of heat transfer enhancement and obtain the best design parameters for different types of corrugated tubes.

Zang et *al.* [42] investigated the applied performance of the four typical enhanced tubes and parameters such as flow pressure drop, the friction factor, enhanced heat transfer, and anti-fouling performance in their study of enhanced tubes. The Nu increased as the roughness height and width and the Re increased and as the roughness pitch decreased. The highest performance evaluation criterion was achieved for height-to-diameter ratio Hl/D = 0.025, pitch-to-tube diameter ratio pl/D = 0.5, and width-to-tube diameter ratio wl/D = 0.2.

Water was used as the working fluid, for internal transverse corrugated tubes of various corrugation shapes (square, rectangular, triangular, and trapezoidal), and geometrical parameters, which were numerically analyzed by Manca et *al.* [43]. This investigation was carried out on turbulent water forced convection in a ribbed channel, Reynolds number ranging from 20,000 to 60,000. In addition, the external walls were heated at a constant heat flux during the experiments.

A numerical is conducted by Mohammad et *al.* [44] to study the effects of various geometrical parameters on the thermal and flow fields through transversely corrugated circular tubes with Re in the range of 5000–60,000 and a heat flux of 50 W/cm^2. The optimization through nineteen transversely corrugated (roughened) tubes, having 10 mm inner diameter, were studied by changing the dimensions of roughness such as relative roughness height in the range of 0.025–0.1, relative roughness pitch in the range of 0.5–1.5, and relative roughness width in the range of 0.05–0.2. For water as a working fluid, heat transfer can be increased with optimal roughness dimensions and maximum performance evaluation criterion (PEC). From this study, the results had shown that the corrugated tube performance was greatly influenced by the geometrical parameters.

Dong et *al.* [45] carried out three-dimensional numerical simulations and experimental investigations of airflow and heat transfer characteristics over the wavy fin heat exchangers to understand the enhancement heat transfer mechanism and optimization design for wavy fin-and-flat tube heat exchangers. The numerical simulation results were compared with the wind tunnel test data, the results showed that the numerical simulation results were in good with the test. The experimental results showed that, in the range of Re = 1000–5500, the standard k-ε mode (SST) is

more suitable to predict the airflow and heat transfer of wavy fin. From their study, it was found that the waviness amplitude had a distinct effect on the heat transfer and pressure drop of the wavy fin, while the wavy fin profile (Triangular, Sinusoidal, and Triangular round corner) had little effect on the heat transfer performance.

Stel et *al.* [46] numerically investigated the turbulent flow in d-type corrugated pipes of various aspect ratios in terms of flow pattern and friction factor, for Reynolds numbers ranging from 5000 to 100,000. Their numerical analysis suggested that d-type behavior exists for groove aspect ratios up to w/k = (groove width/rib height) = 2 independent of the pitch. However, for a ratio of w/k = 3, an important change found in the flow pattern occurs so that the pressure drag exerted by the groove walls became important. It was found that the friction factor was independent of the groove height as long as the flow is similar to a flow in a d-type corrugated pipe.

Li et *al.* [47] experimentally investigated the mechanism of turbulent convective heat transfer enhancement by measuring the heat transfer in two-dimensional roughness tubes with different roughness heights at various Reynolds numbers. From their investigation, it was found that the water as working fluid, heat transfer hardly increased when the roughness height was lower than the thickness of the viscous sublayer, and both heat transfer and flow friction began to increase when the roughness height was higher than the viscous sublayer. Furthermore, when the roughness height was more than five times the viscous sublayer thickness, the flow friction began to increase sharply but heat transfer slowly enhanced. So, they concluded that the best heat transfer enhancement for a given pumping power was reached when the roughness height was about three times the viscous sublayer thickness.

Meng et *al.* [48] carried out experiments on the convection inside a novel alternating elliptical axis tube and found that the mechanism for heat transfer enhancement occurred due to the effect of the multi-longitudinal vortices induced by the cross-sectional change in the alternating elliptical axis tubes. The experiments were carried out in the flow regime, where Reynolds numbers ranging from 500 to 50,000. From the experimental results, the researchers had obtained empirical correlations.

Khoeini et *al.* [49] performed an experimental study to investigate the condensation heat transfer coefficient of R-134a flow inside the corrugated tubes with different inclinations. Different inclinations of test condenser ranging from − 90° to + 90° and various flow mass velocities in the

range of 87 to 253 [kg/m2s] were considered in their study. The obtained results showed that change in the tube inclination had a significant effect on condensation heat transfer behavior. Consequently, at low mass velocities, and low vapor qualities, the highest condensation heat transfer coefficient was obtained for α = + 30° which was 1.41 times greater than the least one obtained for α = − 90°.

Rozzi et al. [50] carried out a study of convective heat transfer and friction losses in helically enhanced tubes for both Newtonian and non-Newtonian fluids. In their work, four fluid foods, namely, whole milk, cloudy orange juice, apricot and apple puree, are tested in a shell and tube heat exchanger as working fluids. From their experimental results, it was found that helically corrugated tubes were particularly effective in enhancing convective heat transfer for generalized Reynolds numbers ranging from about 800 to the limit of the transitional flow regime.

Vicente et al. [51] carried out an experimental study on turbulent heat transfer flow in spirally corrugated tubes. The experiments were carried out for a family consisting of 10 corrugated tubes. The artificial roughness was characterized by the rib height to diameter ratio ranging from 0.02 to 0.06 and the spiral pitch height to diameter ratio from 0.6 to 1.2, for a wide range of turbulent fluid flow conditions: Reynolds number from 2000 to 90,000 and Prandtl number from 2.5 to 100.

Harleß et al. [52] conducted an experimental study on gas-liquid heat exchangers with cross-corrugated tubes. The greatest heat transfer enhancement was obtained for a corrugation height of 1.86 mm and corrugation angle of 38.4°; the optimal corrugation angle was expected to be between 20° and 30° within the high range of the Nusselt number (Nu) augmentation and for a moderate increase in the friction factor. The simulations showed that the average Nu increases as the Re and Hl/D increase, and they are at most equal to 2.6 times that of the smooth tube results.

Stel et al. [53] numerically studied d-type corrugations (roughly square cavities) in a tube with an inner diameter of 25.9 mm. They focused on the effect of the geometry corrugation on the friction factor but did not investigate the heat transfer problem. According to them, the friction factor increased with increases in the groove length.

Zachar [54] studied steady heat transfer in helically coiled-tube heat exchangers and compared the simulation results with experimental values. He performed a 3-D simulation of the flow, although it was restricted to the laminar regime. His results showed that the heart rate in smooth helical tubes was lower than that transferred in HX coils with helically corrugated walls. More recently,

Haervig et *al.* [55] numerically studied sinusoidally spirally corrugated tubes with Reynolds numbers above 5×10^3. They focused on the re-circulation flows that might appear around the corrugated surfaces and their effect on the heat transfer and pressure drop. The experiments were carried out varying the corrugation, the height of corrugation, and the length between two successive corrugated sections to diameter ratios was varied in the ranges 0–0.16 and 0–2.0 respectively. Constant wall heat flux was applied in their study, in the turbulent fluid flow regime of Reynolds number 10,000. Besides, they observed that for certain corrugation lengths, there was an optimal corrugation depth that maximized the Nusselt number.

From the fore mentioned studies, it is noticed that a good number of researchers focused their studies on heat transfer enhancement and fluid friction behavior of circular tubes fitted with various designs of twisted tapes. Twisted tape design with perforations, multi-channels, winglets, etc. helped with further enhancement of heat transfer, but with a considerable penalty on pressure loss. In addition, these modified twisted tapes are complex for manufacturing. It is reported that tapered twisted tape inserts reduce the pressure drop at the cost of lower heat transfer enhancement [41]. Subsequently, it is found from the above-discussed literature that there are several advantages to using the corrugated tube as a heat transfer enhancement technique. Easier fabrication, greater enhancement in thermal performance, and limited increase in flow resistance, over other types of modified surface tubes make the corrugated tube an effective and efficient choice for the researchers. Therefore, the present study intends to investigate the thermal and hydrodynamic characteristics of turbulent fluid flow through the helically corrugated tubes with tapered twisted tape inserts.

Computational fluid dynamics is a popular field of study in academic research as well as in industrial applications. Its famous acronym CFD was only known to high technology engineering areas at an early age. However, it is now a widely adopted methodology in solving complex engineering problems. In this present study, the CFD tool Ansys Fluent is used to explore different performance characteristics of the turbulent flow through the twisted tapes inserted in corrugated tubes.

3.1 Governing Equations

CFD is fundamentally based on the mathematical representation of conservation laws of physics in terms of governing equations of fluid dynamics. It predicts and analyzes fluid motion and heat transfer behavior by adopting the following physical laws:

- The mass of fluid is conserved
- The rate of change of momentum of fluid equals the sum of forces acting on it, Newton's second law.
- The rate of change of energy equals the sum of the rate of heat addition and the rate of work done on the fluid, the First law of thermodynamics.

Ansys Fluent solves the mass conservation equation and the momentum conservation equation for all fluid flows. Besides, it solves energy equations where the fluid flow is associated with heat transfer. For turbulent fluid flow, additional transport equations are solved. The governing equations in Cartesian coordinates for incompressible flow are given below [58]

Mass conservation equation

$$\frac{\partial u}{\partial x} + \frac{\partial v}{\partial y} + \frac{\partial w}{\partial z} = 0 \tag{1}$$

Momentum equation

$$\frac{\partial u}{\partial t} + \frac{\partial (uu)}{\partial x} + \frac{\partial (vu)}{\partial y} + \frac{\partial (wu)}{\partial z} = \frac{\partial}{\partial x}\left[(\vartheta + \vartheta_T)\frac{\partial u}{\partial x}\right] + \frac{\partial}{\partial y}\left[(\vartheta + \vartheta_T)\frac{\partial u}{\partial y}\right] + \frac{\partial}{\partial z}\left[(\vartheta + \vartheta_T)\frac{\partial u}{\partial z}\right] + \left(S_u = -\frac{1\partial p}{\rho \partial x} + S_u'\right) \tag{2}$$

$$\frac{\partial v}{\partial t} + \frac{\partial(uv)}{\partial x} + \frac{\partial(vv)}{\partial y} + \frac{\partial(wv)}{\partial z} = \frac{\partial}{\partial x}\left[(\vartheta + \vartheta_T)\frac{\partial v}{\partial x}\right] + \frac{\partial}{\partial y}\left[(\vartheta + \vartheta_T)\frac{\partial v}{\partial y}\right] + \frac{\partial}{\partial z}\left[(\vartheta + \right.$$

$$\left. \vartheta_T)\frac{\partial v}{\partial z}\right] + \left(S_v = -\frac{1}{\rho}\frac{\partial p}{\partial y} + S_v'\right) \tag{3}$$

$$\frac{\partial w}{\partial t} + \frac{\partial(uw)}{\partial x} + \frac{\partial(vw)}{\partial y} + \frac{\partial(ww)}{\partial z} = \frac{\partial}{\partial x}\left[(\vartheta + \vartheta_T)\frac{\partial w}{\partial x}\right] + \frac{\partial}{\partial y}\left[(\vartheta + \vartheta_T)\frac{\partial w}{\partial y}\right] + \frac{\partial}{\partial z}\left[(\vartheta + \right.$$

$$\left. \vartheta_T)\frac{\partial w}{\partial z}\right] + \left(S_w = -\frac{1}{\rho}\frac{\partial p}{\partial z} + S_w'\right) \tag{4}$$

Energy Equation

$$\frac{\partial T}{\partial t} + \frac{\partial(uT)}{\partial x} + \frac{\partial(vT)}{\partial y} + \frac{\partial(wT)}{\partial z} = \frac{\partial}{\partial x}\left[\left(\frac{\vartheta}{Pr} + \frac{\vartheta_T}{Pr_T}\right)\frac{\partial T}{\partial x}\right] + \frac{\partial}{\partial y}\left[\left(\frac{\vartheta}{Pr} + \frac{\vartheta_T}{Pr_T}\right)\frac{\partial T}{\partial y}\right] + \frac{\partial}{\partial z}\left[\left(\frac{\vartheta}{Pr} + \right.\right.$$

$$\left.\left. \frac{\vartheta_T}{Pr_T}\right)\frac{\partial T}{\partial z}\right] + S_T \tag{5}$$

In the above-mentioned equations, u, v, and w are the velocity component in the x-, y-, and z-direction respectively, ρ is the fluid density, ϑ in the kinematic viscosity, T is the temperature, and Pr is the Prandtl Number. Moreover, the additional source terms in the momentum equation S_u', S_v', and S_w' are comprised of pressure and non-pressure gradient terms such as gravity which influence the fluid motion. Another Source term S_T mentioned in the energy equation, contains sources and sinks in the fluid domain.

3.2 Turbulence Modeling

Turbulence is associated with the existence of random fluctuations in the fluid. It can be defined as the sudden disordered changes of pressure and velocity in the fluid flow field. This behavior can be amplified when the fluid flows over or between rough surfaces such as a corrugated tube. At high Reynolds number, the inertia force dominates the viscous force which induces fluctuation in the streamline. Then the velocity and all other properties act chaotically. These fluctuations mix transported quantities such as momentum, energy, and species concentration, and cause the transported quantities to fluctuate as well. Since these fluctuations can be of small scale and high frequency, they are too computationally difficult to simulate directly in practical engineering calculations.

A turbulence model is a semi-empirical equation relating the fluctuating correlation to mean flow variables with various constants provided from experimental investigations. These models are developed based on experimental data obtained from relatively simple flows under a controlled environment. That in turn limits the range of applicability of turbulence models. When this equation is expressed as an algebraic equation, it is referred to as the zero-equation model. When partial differential equations are used, they are referred to as one-equation or two-equation models, depending on the number of PDEs used. Some models employ ordinary differential equations, in which case they are referred to as half-equation models. Finally, it is possible to write a partial differential equation directly for each of the turbulence correlations in which case they compose a system of PDEs known as the Reynolds stress equations. Some turbulence models are there to match the conditions like

i. Reynolds Averaged Navier-Stokes (RANS) model
ii. v^2-f model
iii. Reynolds Stress Model (RSM)
iv. Detached Eddy Simulation (DES) model
v. Large Eddy Simulation (LES) model

3.2.1 Reynolds Averaged Navier-Stokes Equations

With modern-day computing power, the time-dependent Navier-Stokes equation can predict the time-averaged properties such as mean pressure, mean velocity, and mean stress of the flow, for high Reynolds-number turbulent flows in complex geometries. To render the Navier-Stokes equations tractable two alternative methods can be employed so that the small-scale turbulent fluctuations do not have to be directly simulated: Reynolds-averaging (or ensemble-averaging) and filtering. Both methods introduce additional terms in the governing equations that need to be modeled to achieve a "closure" for the unknowns.

The Reynolds-averaged Navier-Stokes (RANS) equations govern the transport of the averaged flow quantities, with the whole range of the scales of turbulence being modeled. The RANS-based modeling approach therefore greatly reduces the required computational effort and resources and is widely adopted for practical engineering applications.

Conservation of Mass

$$\frac{\partial \rho}{\partial t} + \frac{\partial \rho u_i}{\partial x_i} = 0 \tag{6}$$

Conservation of momentum

$$\frac{\partial \rho u_i}{\partial t} + \frac{\partial \rho u_i u_j}{\partial x_j} = \frac{\partial}{\partial x_j}\left(\mu \frac{\partial u_i}{\partial x_j} - \rho \overline{u_i u_j}\right) - \frac{\partial P}{\partial x_i} + S_{ui} \tag{7}$$

Conservation of passive scalars (given a scalar T)

$$\frac{\partial \rho c_p T}{\partial t} + \frac{\partial \rho c_p u_j T}{\partial x_j} = \frac{\partial}{\partial x_j}\left(k \frac{\partial T}{\partial x_j} - \rho c_p \overline{u_j t}\right) + S_t \tag{8}$$

After the Reynolds decomposition, there are new unknowns like the turbulent stresses (known as Reynolds stresses, $\rho \overline{u_i u_j}$) and turbulent fluxes. This nonlinear Reynolds stress term requires additional Modelling to close the RANS equation for solving and has led to the creation of many different turbulence models.

Available RANS based two-equation turbulence models in Ansys FLUENT are as follows:

- k-ϵ model
    - Standard k-ϵ model
    - Renormalized -group (RNG) k-ϵ model
    - Realizable k-ϵ model
- k-ω model
    - Standard k-ω model
    - Shear-stress transport (SST) k-ω model

3.2.1.1 Standard k-ϵ model

The standard k-ϵ model is a semi-empirical model based on model transport equations for the turbulence kinetic energy (k) and its dissipation rate (ϵ). The model transport equation for (k) is derived from the exact equation, while the model transport equation for ϵ was obtained using physical reasoning and bears little resemblance to its mathematical counterpart. In the derivation of the k-ϵ model, the assumption is that the flow is fully turbulent, and the effects of molecular viscosity are negligible. The standard k-ϵ model is therefore valid only for fully turbulent flows.

The turbulence kinetic energy (k) and the rate of dissipation (ϵ), are obtained from the following transport equations:

$$\frac{\partial}{\partial t}(\rho k) + \frac{\partial}{\partial x_i}(\rho k u_i) = \frac{\partial}{\partial x_j}\left[\left(\mu + \frac{\mu_t}{\sigma_k}\right)\frac{\partial k}{\partial x_j}\right] + G_k + G_b - \rho\epsilon - Y_M + S_k \qquad (9)$$

$$\frac{\partial}{\partial t}(\rho\epsilon) + \frac{\partial}{\partial x_i}(\rho\epsilon u_i) = \frac{\partial}{\partial x_j}\left[\left(\mu + \frac{\mu_t}{\sigma_\epsilon}\right)\frac{\partial \epsilon}{\partial x_j}\right] + C_{1\epsilon}\frac{\epsilon}{k}(G_k + C_{3\epsilon}G_b) - C_{2\epsilon}\rho\frac{\epsilon^2}{k} + S_\epsilon \quad (10)$$

In these equations, G_k represents the generation of turbulence kinetic energy due to the mean velocity gradients, calculated as mentioned in equation (9). G_b is the generation of turbulence kinetic energy due to buoyancy, calculated as described in equation (10). Y_M represents the contribution of the fluctuating dilatation incompressible turbulence to the overall dissipation rate, $C_{1\epsilon}$, $C_{2\epsilon}$, and $C_{3\epsilon}$ are constants. σ_k and σ_ϵ are the turbulent Prandtl numbers for k and ϵ, respectively. S_k and S_ϵ are user-defined source terms.

The turbulent viscosity (μ_t) is computed by combining k and ϵ,

$$\mu_t = \rho C_\mu \frac{k^2}{\epsilon} \qquad (11)$$

where C_μ is a constant.

The model constants $C_{1\epsilon}$, $C_{2\epsilon}$, C_μ, σ_k and σ_ϵ have the following default values which have been determined from experiments with air and water for fundamental turbulent shear flows including homogeneous shear flows and decaying isotropic grid turbulence. They have been found to work fairly well for a wide range of wall-bounded and free shear flows.

$C_{1\epsilon} = 1.44$, $C_{2\epsilon} = 1.92$, $C_\mu = 0.09$, $\sigma_k = 1.0$, $\sigma_\epsilon = 1.3$

3.2.1.2 RNG k-ϵ model

The RNG-based k-ϵ turbulence model is derived from the instantaneous Navier-Stokes equations, using a mathematical technique called "renormalization group" (RNG) methods. A rigorous statistical technique from the Renormalized group theory refines the standard k-ϵ model and derived the RNG k-ϵ model. In this model, an additional term ϵ is added in the equation that significantly improves the accuracy for rapidly strained flows. The effect of swirl on turbulence is included in the RNG k-ϵ model, enhancing accuracy for swirling flows. Besides, The RNG theory provides an analytical formula for turbulent Prandtl numbers, while the standard k-ϵ model uses user-specified, constant values. The transport equations for the RNG k-ϵ model is given as follows:

$$\frac{\partial}{\partial t}(\rho k) + \frac{\partial}{\partial x_i}(\rho k u_i) = \frac{\partial}{\partial x_j}\left(\alpha_k \mu_{eff} \frac{\partial k}{\partial x_j}\right) + G_k + G_b - \rho\epsilon - Y_M + S_k \qquad (12)$$

$$\frac{\partial}{\partial t}(\rho\epsilon) + \frac{\partial}{\partial x_i}(\rho\epsilon u_i) = \frac{\partial}{\partial x_j}\left(\alpha_\epsilon \mu_{eff} \frac{\partial\epsilon}{\partial x_j}\right) + C_{1\epsilon}\frac{\epsilon}{k}(G_k + C_{3\epsilon}G_b) - C_{2\epsilon}\rho\frac{\epsilon^2}{k} - R_\epsilon +$$

$$S_\epsilon \qquad (13)$$

Turbulence, in general, is affected by rotation or swirl in the mean flow. The RNG model in Ansys Fluent provides an option to account for the effects of swirl or rotation by modifying the turbulent viscosity appropriately. The modification takes the following functional form:

$$\mu_t = \mu_{t0}\, f\left(\alpha_s, \Omega, \frac{k}{\epsilon}\right) \qquad (14)$$

where μ_{t0} is the value of turbulent viscosity calculated without the swirl modification using equation (11), Ω is a characteristic swirl number evaluated within Ansys Fluent, and α_s is a swirl constant that assumes different values depending on whether the flow is swirl-dominated or only mildly swirling.

The main difference between the RNG and standard k-ϵ models, lies in the additional term in the ϵ equation given by

$$R_\epsilon = \frac{C_\mu \rho \eta^3(1 - \eta/\eta_o)}{1 + \beta\eta^3}\frac{\epsilon^2}{k} \qquad (15)$$

here, $\eta \equiv \frac{S_k}{\epsilon}$, $\eta_0 = 4.38$, $\beta = 0.012$

3.2.1.3 Realizable k-ϵ model

The realizable k-ϵ model is a relatively recent development and differs from the standard k-ϵ model in two important ways:

1. The realizable k-ϵ model contains a new formulation for the turbulent viscosity.

2. A new transport equation for the dissipation rate, ϵ, has been derived from an exact equation for the transport of the mean-square vorticity fluctuation.

The term "realizable" means that the model satisfies certain mathematical constraints on the Reynolds stresses, consistent with the physics of turbulent flows. Neither the standard k-ϵ model nor the RNG k-ϵ model is realizable.

An immediate benefit of the realizable k-ϵ model is that it more accurately predicts the spreading rate of both planar and round jets. It is also likely to provide superior performance for flows involving rotation, boundary layers under strong adverse pressure gradients, separation, and recirculation.

3.2.1.4 Standard k-ω model

This two-equation model includes one equation for the turbulent kinetic energy (k), as developed previously, and a second equation for the specific turbulent dissipation rate (ω). The standard k-ω model is an empirical model based on model transport equations for the turbulence kinetic energy (k) and the specific dissipation rate (ω), which can also be thought of as the ratio of ϵ to k. As the k-ω model has been modified over the years, production terms have been added to both the k and ω equations, which have improved the accuracy of the model for predicting free shear flows.

The turbulence kinetic energy, k, and the specific dissipation rate, ω, are obtained from the following transport equations:

$$\frac{\partial}{\partial t}(\rho k) + \frac{\partial}{\partial x_i}(\rho k u_i) = \frac{\partial}{\partial x_j}\left[\Gamma_k \frac{\partial k}{\partial x_j}\right] + G_k - Y_k + S_k \tag{16}$$

$$\frac{\partial}{\partial t}(\rho \omega) + \frac{\partial}{\partial x_i}(\rho \omega u_i) = \frac{\partial}{\partial x_j}\left[\Gamma_\omega \frac{\partial \omega}{\partial x_j}\right] + G_\omega - Y_\omega + S_\omega \tag{17}$$

In these equations, G_k represents the generation of turbulence kinetic energy due to mean velocity gradients. G_ω represents the generation of ω. Γ_k and Γ_ω represent the effective diffusivity of k and ω, respectively. Y_k and Y_ω represent the dissipation of k and ω due to turbulence. All of the above terms are calculated as described below. S_k and S_ω are user-defined source terms.

The effective diffusivities for the k-ω model are given by

$$\Gamma_k = \mu + \frac{\mu_k}{\sigma_k} \tag{18}$$

$$\Gamma_\omega = \mu + \frac{\mu_\omega}{\sigma_\omega} \tag{19}$$

where σ_k and σ_ω are the turbulent Prandtl numbers for k and ω, respectively.

3.2.1.5 Shear Stress Transport (SST) k-ω model

The shear-stress transport (SST) k-ω model was developed to effectively blend the robust and accurate formulation of the k-ω model in the near-wall region with the free-stream independence of the k-ϵ model in the far-field. To achieve this, the k-ϵ model is converted into a k-ω formulation. The SST k-ω model is similar to the standard k-ω model, but includes the following refinements:

1. The standard k-ω model and the transformed k-ϵ model both are multiplied by a blending function and both models are added together. The blending function is designed to be one

in the near-wall region, which activates the standard k-ω model and zero away from the surface, which activates the transformed k-ϵ model.

2. The SST model incorporates a damped cross-diffusion derivative term in the ω equation.
3. The definition of turbulent viscosity is modified to account for the transport of the turbulent shear stress.
4. The modelling constants are different.

The SST k-ω model has a similar form of transport equation to the standard k-ω model:

$$\frac{\partial}{\partial t}(\rho k) + \frac{\partial}{\partial x_i}(\rho k u_i) = \frac{\partial}{\partial x_j}\left[\Gamma_k \frac{\partial k}{\partial x_j}\right] + \tilde{G}_k - Y_k + S_k \tag{20}$$

$$\frac{\partial}{\partial t}(\rho \omega) + \frac{\partial}{\partial x_i}(\rho \omega u_i) = \frac{\partial}{\partial x_j}\left[\Gamma_\omega \frac{\partial \omega}{\partial x_j}\right] + G_\omega - Y_\omega + D_\omega + S_\omega \tag{21}$$

In these equations, $\tilde{G}_k$ represents the generation of turbulence kinetic energy due to mean velocity gradients. G_ω represents the generation of ω. Γ_k and Γ_ω represent the effective diffusivity of k and ω, respectively. Y_k and Y_ω represent the dissipation of k and ω due to turbulence. All of the above terms are calculated as described below. S_k and S_ω are user-defined source terms. D_ω represents the cross-diffusion term.

The effective diffusivities for the SST k-ω model are given by

$$\Gamma_k = \mu + \frac{\mu_k}{\sigma_k} \tag{22}$$

$$\Gamma_\omega = \mu + \frac{\mu_\omega}{\sigma_\omega} \tag{23}$$

where σ_k and σ_ω are the turbulent Prandtl numbers for k and ω, respectively. The turbulent viscosity, μ_t, is computed as follows:

$$\mu_t = \frac{\rho k}{\omega} \frac{1}{\max\left[\frac{1}{\alpha^*}, \frac{SF_2}{\alpha_1 \omega}\right]} \tag{24}$$

where S is the strain rate magnitude.

The wall boundary conditions for the k equation in the k-ω models are treated in the same way as the k equation is treated when enhanced wall treatments are used with the k-ϵ models. This means that all boundary conditions for wall-function meshes will correspond to the wall function approach, while for the fine meshes, the appropriate low-Reynolds-number boundary conditions will be applied.

In the Ansys Fluent, the value of ω at the wall is specified as

$$\omega_w = \frac{\rho(u^*)^2}{\mu} \, \omega^+ \tag{25}$$

The asymptotic value of ω^+ is given by in the turbulent region

$$\omega^+ = \frac{1}{\sqrt{\beta_\infty^*}} \frac{du_{turb}^+}{dy^+} \tag{26}$$

This leads to the value of ω in the wall cell as

$$\omega = \frac{u^*}{\sqrt{\beta_\infty^*}\, ky} \tag{27}$$

CHAPTER 4

Computational Model

The present study aims to do computational analysis for turbulent fluid flow through the straight circular tube and corrugated tubes of different configurations, with twisted tape inserts of different configurations. In this chapter, the development of the computational model and its verification and validation will be discussed.

4.1 Physical model

In the present investigation, a straight circular tube (SCT), and four helically corrugated tubes (HCT) of pitch-to-diameter ratios (ratio of pitch length, pl to pipe diameter, D; $pl/D = 1, 1.5$) and height-to-diameter ratios (ratio of corrugation height length, Hl to pipe diameter, D; $Hl/D = 0.05$, 0.1) are developed. The configuration of these tubes is given in Table 1, and the tubes are shown in Fig. 4.1.1. Besides, tapered twisted tape (TTT) inserts i.e., the width of the tape gradually decreases along the flow direction, with twist ratios (ratio of the pitch length of the tape, y to the tape width w; $y/w = 3.5, 5$), and tapered angles ($\theta = 0^o, 0.3^o$ and 0.5^o), are developed. The configuration of these twisted tapes is given in Table 2, the twisted tapes are illustrated in Fig. 4.1.2. Whilst Fig. 4.1.3 shows the tapered twisted tapes into the tubes. Several computational domains are developed in response to the fluid flowing through the SCT and HCTs, accompanying the TTTs inside the tubes. The total length of the domain is 800 mm with 25.4 mm diameter where the corrugated section and the tapered twisted tape section, both are 600 mm in length. The inserts are placed maintaining a distance of 100 mm from both the inlet and the outlet of the fluid domain, shown in Fig. 4.1.4. Firstly, the fluid domain of cylindrical shape is generated. After that, the twisted tape insert, and the helically corrugated section, are generated within the fluid domain using the Sweep tool. Then the inserted domain is a cutout from the domain, and the helically corrugated groove is united with the domain, using the Boolean operation. The configuration of the total 30 developed 3-D computational fluid domains' configuration is given in Table-3.

Table 1: Geometric dimensions of the tubes considered in the present study

Tube	D (mm)	pl (mm)	Hl (mm)	pl/D	Hl/D
SCT	25.4	0	0	0.0	0.0
HCT-1	25.4	38.1	1.27	1.5	0.05
HCT-2	25.4	38.1	2.54	1.5	0.1
HCT-3	25.4	25.4	1.27	1	0.05
HCT-4	25.4	25.4	2.54	1	0.1

SCT: $(Hl/D) = 0.0$, $(pl/D) = 0.0$

HCT-1: $(Hl/D) = 0.05$, $(pl/D) = 1.5$

HCT-2: $(Hl/D) = 0.1$, $(pl/D) = 1.5$

HCT-3: $(Hl/D) = 0.05$, $(pl/D) = 1.0$

HCT-4: $(Hl/D) = 0.1$, $(pl/D) = 1.0$

pl

Hl
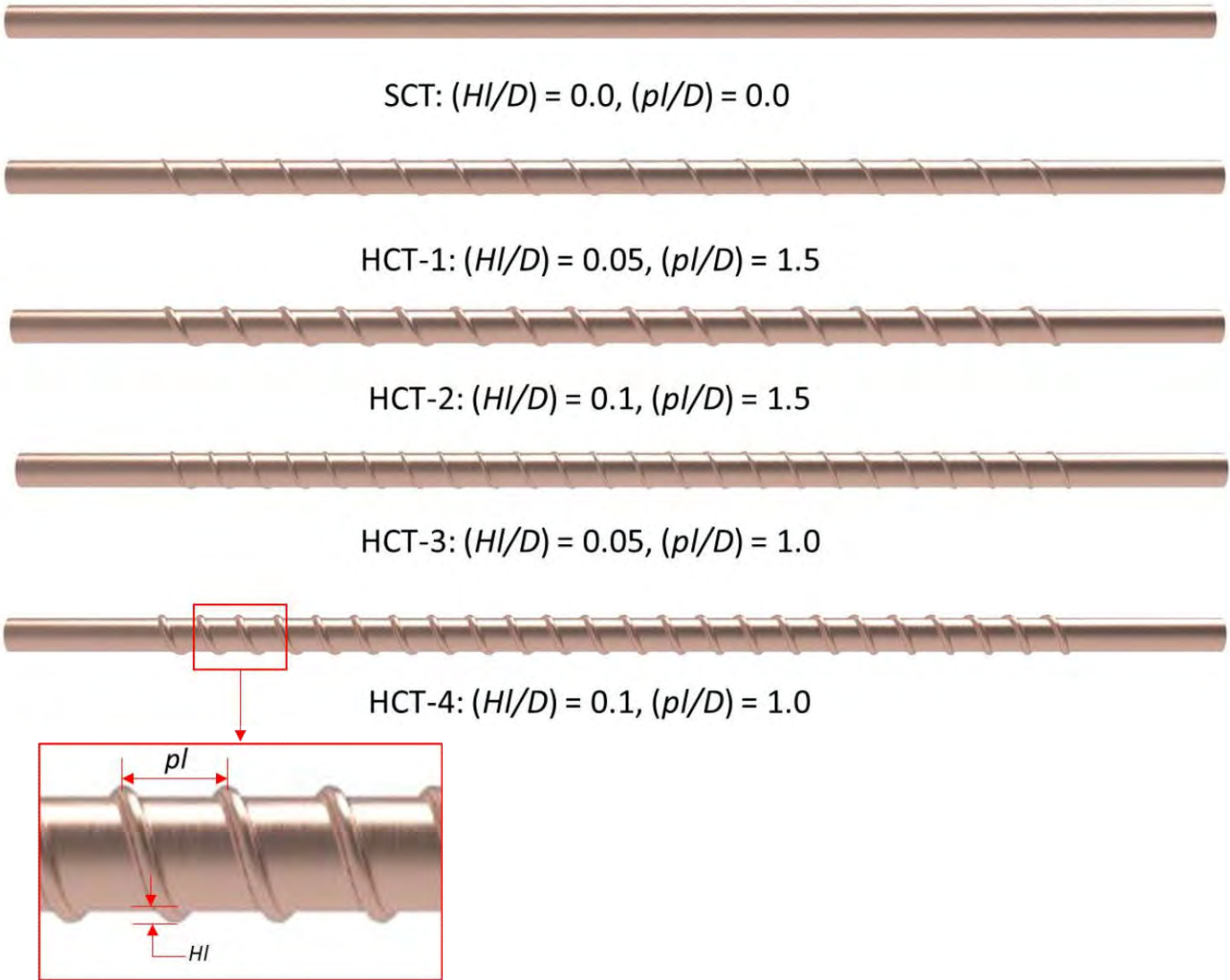
Fig. 4.1.1: Tubes with different configurations

Table 2: Geometric dimensions of different tapered twisted tapes considered in this study

Tape	L (mm)	w (mm)	y (mm)	y/w	θ
TTT-1	600	20	70	3.5	0º
TTT-2	600	20	70	3.5	0.3º
TTT-3	600	20	70	3.5	0.5º
TTT-4	600	20	100	5	0º
TTT-5	600	20	100	5	0.3º
TTT-6	600	20	100	5	0.5º

TTT-1: $(y/w) = 3.5, \theta = 0°$

TTT-2: $(y/w) = 3.5, \theta = 0.3°$

TTT-3: $(y/w) = 3.5, \theta = 0.5°$

TTT-4: $(y/w) = 5, \theta = 0°$

TTT-5: $(y/w) = 5, \theta = 0.3°$

TTT-6: $(y/w) = 5, \theta = 0.5°$

Tapered angle, θ
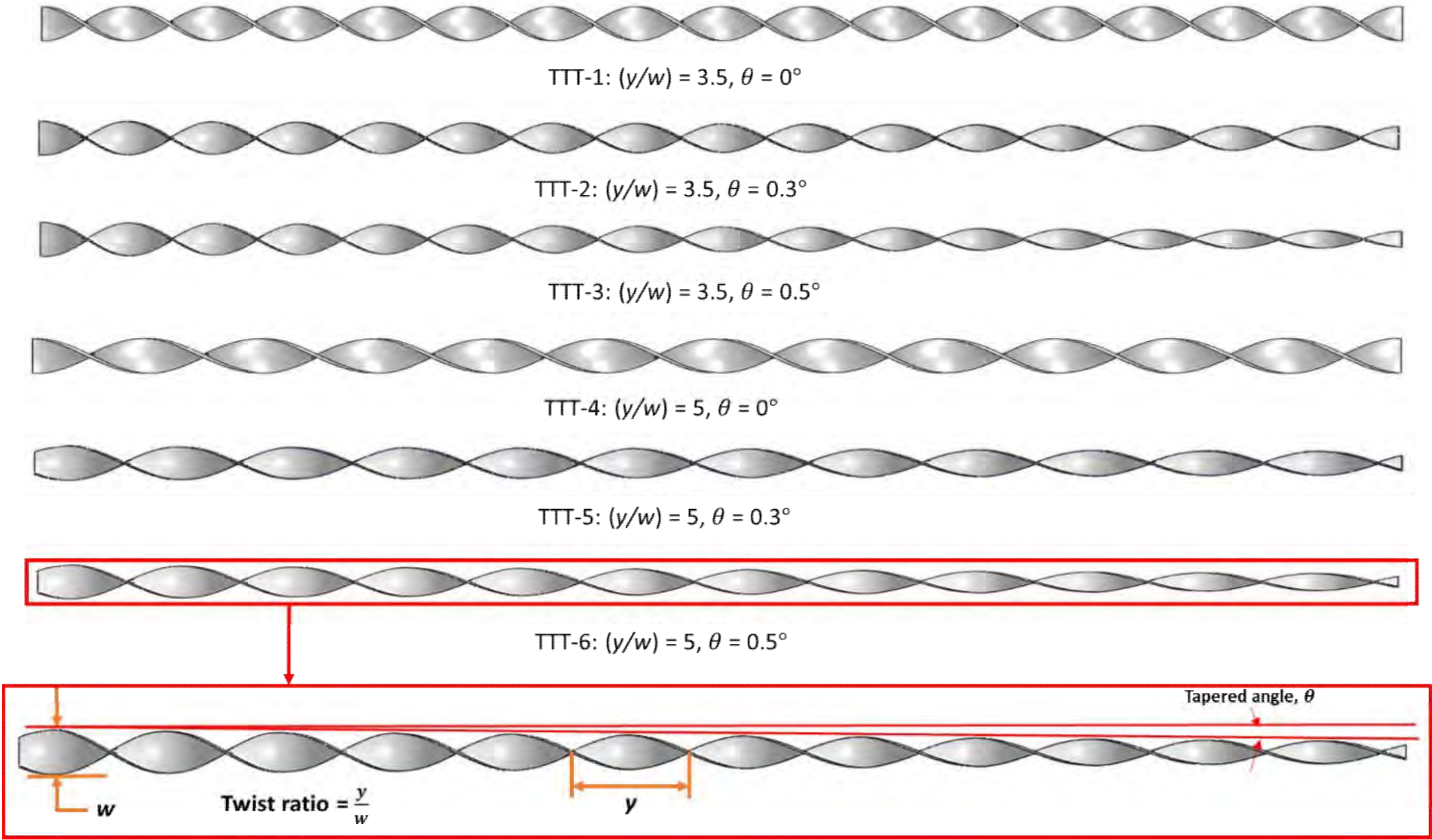
w Twist ratio $= \dfrac{y}{w}$ y

Fig. 4.1.2: Twisted tape inserts with different twist ratios and tapered angles
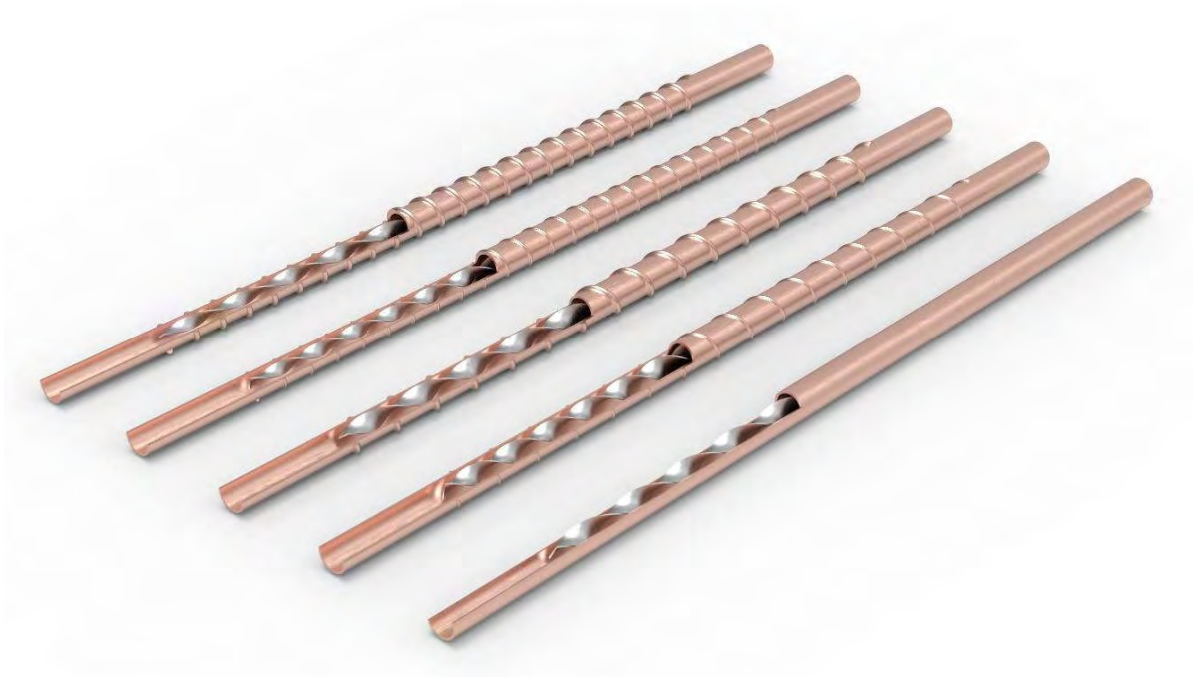
Fig. 4.1.3: Twisted tapes inserted into the tubes
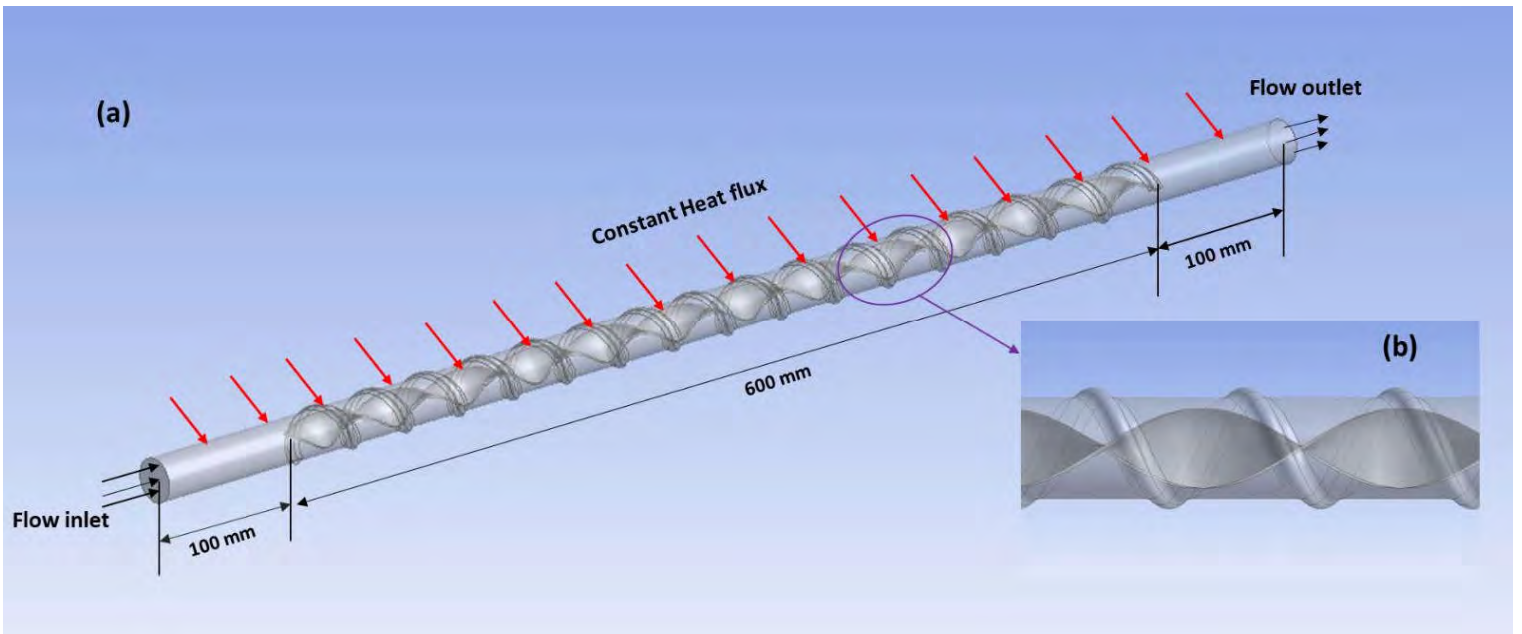
Fig. 4.1.4: Computational model: (a) 3-D view of the fluid domain; (b)side view of the domain.

Table 3: Computational model cases

No. of Cases	TTT*		HCT**	
	y/w	*θ*	*Hl/D*	*pl/D*
Case 1	5	0	0	0
Case 2	5	0	0.05	1.5
Case 3	5	0	0.1	1.5
Case 4	5	0	0.05	1
Case 5	5	0	0.1	1
Case 6	5	0.5	0	0
Case 7	5	0.5	0.05	1.5
Case 8	5	0.5	0.1	1.5
Case 9	5	0.5	0.05	1
Case 10	5	0.5	0.1	1
Case 11	5	0.3	0	0
Case 12	5	0.3	0.05	1.5
Case 13	5	0.3	0.1	1.5
Case 14	5	0.3	0.05	1
Case 15	5	0.3	0.1	1
Case 16	3.5	0	0	0
Case 17	3.5	0	0.05	1.5
Case 18	3.5	0	0.1	1.5
Case 19	3.5	0	0.05	1
Case 20	3.5	0	0.1	1
Case 21	3.5	0.5	0	0
Case 22	3.5	0.5	0.05	1.5
Case 23	3.5	0.5	0.1	1.5
Case 24	3.5	0.5	0.05	1
Case 25	3.5	0.5	0.1	1
Case 26	3.5	0.3	0	0
Case 27	3.5	0.3	0.05	1.5
Case 28	3.5	0.3	0.1	1.5
Case 29	3.5	0.3	0.05	1
Case 30	3.5	0.3	0.1	1

*TTT – Tapered Twisted Tape

**HCT – Helically Corrugated Tube

4.2 Mesh Generation

Mesh generation is the practice of generating a polygonal or polyhedral mesh that approximates a geometric domain. The term "grid generation" is often used interchangeably. The partial differential equations that govern fluid flow and heat transfer are not usually amenable to analytical solutions, except for very simple cases. Therefore, to analyze fluid flows, flow domains are split into smaller sub-domains (made up of geometric primitives like tetrahedral in a 3D domain, shown in Fig. 4.2.1). The governing equations are then discretized and solved inside each of these subdomains. Ansys Fluent uses the Finite Volume Method (FVM) to solve the approximate version of the system of equations. But care must be taken to ensure proper continuity of solution across the common interfaces between two subdomains so that the approximate solutions inside various portions can be put together to give a complete picture of fluid flow in the entire domain. The subdomains are often called elements or cells, and the collection of all elements or cells is called a mesh or grid.

For meshing the model proximity and curvature is used for advanced sizing, for relevance center coarse is used and soothing is kept low to reduce the meshing times. Edge sizing has been done at the inlet and outlet of the fluid domain and also at the insert edges. Fig. 4.2.1 (a), illustrates the meshed geometry of the 3D fluid domain. Closer views at the corrugation section, see Fig. 4.2.1 (b) and (c), show that there is a sufficient number of elements to provide accurate results.
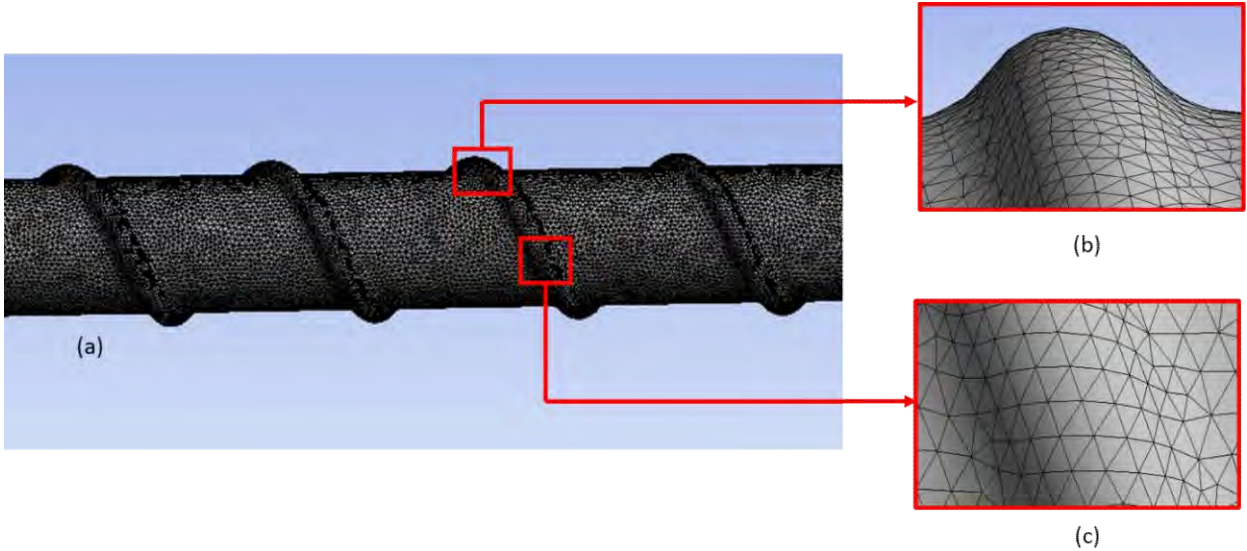
Fig. 4.2.1: Meshed geometry: (a) Front view; (b) and (c) corrugation section of the geometry.

To find the optimum mesh density for an accurate solution with less possible time consumption, the grid-independent test is conducted, see Table 4. Five different mesh densities generated for the corrugated tube (Hl/D) = 0.1 and (pl/D) = 1.0, with tapered twisted tape insert (y/w) = 3.5 and (θ) = 0.5°, at Re = 10433. The results showed that the variation in Nusselt number and friction factor does not exceed 1.48% and 1.89%, respectively when the number of mesh changes from 3,157,652elements to 3,601,783 elements. The mentioned variation is small. So, to consider the time consumption, mesh 4 is selected to solve this model.

Table 4: Grid independence analysis

Mesh	Number of elements	Nusselt number, Nu	Friction factor, f
Mesh - 1	1,668,241	57.66	0.141
Mesh - 2	1,905,389	60.57	0.146
Mesh - 3	2,558,316	63.93	0.151
Mesh - 4	**3,157,652**	**64.23**	**0.158**
Mesh - 5	3,601,783	65.18	0.161

4.3 Discretization

The process of obtaining the computational solution consists of two stages. The first stage involves the conversion of the partial differential equations and auxiliary (boundary and initial) conditions into a system of discrete algebraic equations. This first stage is commonly known as the discretization stage. In the present study, the CFD tool has been used, apply the finite volume method to discretize the governing equations.

4.3.1 Finite Volume Method

The finite-volume method like the finite-element method has the capacity of handling arbitrary geometries with ease. It can be applied to structured, body-fitted, and unstructured meshes. More importantly, this method bears many similarities with the finite-difference method; it is thus simple to apply. Because of the many advantages, one of which is consistent with the concept of the control volume approach, the most common form of discretization in use today for finite-volume applications will be thus emphasized.

The finite-volume method discretizes the integral form of the conservation equations directly in the physical space. The computational domain is subdivided into a finite number of contiguous control volumes, where the resulting statements express the exact conservation of relevant properties for each of the control volumes. At the centroid of each of the control volumes, the variable values are calculated. Interpolation is used to express variable values at the control volume surface in terms of the center values, and suitable quadrature formulae are applied to approximate the surface and volume integrals. An algebraic equation for each of the control volumes can be obtained, in which a number of the neighboring nodal values appear. As the finite-volume method works with control volumes and not the grid intersection points, it can accommodate any type of grid. Here, instead of structured grids, unstructured grids can be employed that allow a large number of options for the definition of the shape and location of the control volumes. Since the grid defines only the control volume boundaries, the method is conservative so long as the surface integrals that are applied at these boundaries are the same as the control volumes sharing the boundary. As with the finite-difference method, a numerical grid must be initially defined to discretize the physical flow domain of interest.

4.3.2 Solver Setting

CFD allows choosing one of the two numerical methods:

   i.   Pressure-based solver
  ii.   Density-based solver

The pressure-based approach was developed for low-speed incompressible flows, while the density-based approach was mainly used for high-speed compressible flow. However, recently both methods have been extended and reformulated to solve and operate a wide range of flow conditions beyond the traditional and original intent. In both methods, the velocity field is obtained from the momentum equations. In the density-based approach, the continuity equation is used to obtain the density field while pressure is determined from the equation of state. On the other hand, in the pressure-based approach, the pressure field is extracted by solving a pressure or pressure correction equation which is obtained by manipulating continuity and momentum equations. Using either method the present CFD tool will solve the governing integral equations for the conservation of mass and momentum and energy and other scalars such as turbulence and chemical species. During this present study, a pressure-based solver has been used.

4.3.3 Discretization Scheme

Density, momentum, turbulent kinetic energy, dissipation rate, and energy equations have First Order Upwind, Second-Order Upwind, QUICK, and Third-Order MUSCL schemes. For all cases, Second-order upwind schemes are selected. When the flow is aligned with the grid (e.g., laminar flow in a rectangular duct modeled with quadrilateral or hexahedral grid) the first-order upwind discretization is acceptable. When the flow is not aligned with the grid (e.g., when it crosses the gridline obliquely), however, first-order convective discretization increases the numerical discretization error (numerical diffusion). For triangular and tetrahedral grids, since the flow is never aligned with the grid, generally, more accurate results are obtained by using second-order discretization. For quadrilateral/hexahedral grids better results using the second-order discretization are obtained, especially for complex flows.

4.4 Boundary conditions

For all simulation scenarios, the velocity inlet condition is used as the inlet boundary condition, and the pressure outlet condition with zero-gauge pressure is used as the outlet boundary condition. The working fluid in this study is air, and the properties of air are listed in Table 5. The air enters the tube at a temperature of 300 K and a velocity that corresponds to the tubes. Simulations are run at a constant heat flux of 2000 W/m^2 at the pipe wall for all the cases [41, 57]. The wall between fluid and insert is assumed adiabatic (no conduction heat transfer). Table 6. shows the details of the boundary conditions. All the specified cases have been studied for the Reynolds number ranging from 3400 to 21000.

Table 5: Properties of working fluid

Variable	Unit	Air
Density, ρ	kg/m^3	1.225
Specific Heat, C_p	$J/(kg.K)$	1006.43
Thermal Conductivity, k	$W/(m.k)$	0.0242
Dynamic viscosity, μ	$kg/m.s$	1.7894×10^{-5}
Prandtl Number, Pr	-	0.707

Table 6: Boundary Conditions

Hydraulic Boundary Conditions

Zone	Boundary condition	Parameters	Equations
Inlet	Velocity inlet	Velocity corresponding to Reynolds number Turbulent intensity 5%	$u = const.$
Outlet	Pressure outlet	Atmospheric pressure	$\frac{\partial u_n}{\partial n} = 0$ P = atm
Wall	no slip		$u = u_w$

Thermal Boundary Conditions

Zone	Boundary condition	Parameters	Equations
Pipe wall	Wall	Constant 2000 W/m^2 heat flux	$\frac{k\partial T}{\partial n} = -q_w$
Inlet	Wall	Constant temperature 300 K	$T = const.$
Outlet	Wall	Convective boundary condition	$\frac{\partial T}{\partial n} = 0$

4.5 Solution Procedure

The time-independent incompressible Navier–Stokes equations and the Shear Stress Transport (SST) k-ω turbulence model, are discretized using the finite volume technique in the current numerical solution. To evaluate the pressure field, the pressure–velocity coupling scheme SIMPLE (Semi Implicit Method for Pressure-Linked Equations) has been selected. For spatial discretization, the second-order upwind has been selected for pressure, momentum, energy, turbulent kinetic energy, and specific dissipation rate. The convergence criteria have been set 10^{-6}. The hybrid initialization method has been selected to initialize the solution. Three parameters of interest for the present work are: (1) Nusselt number, (2) friction factor, and (3) thermal performance factor which are respectively used for characterization of heat transfer rate, friction loss, and effectiveness of heat transfer enhancement in the straight circular tube, and the corrugated tubes with tapered twisted tape inserts for designed geometries and flow conditions. The overview of the solution procedure is depicted in Fig. 4.4.1.
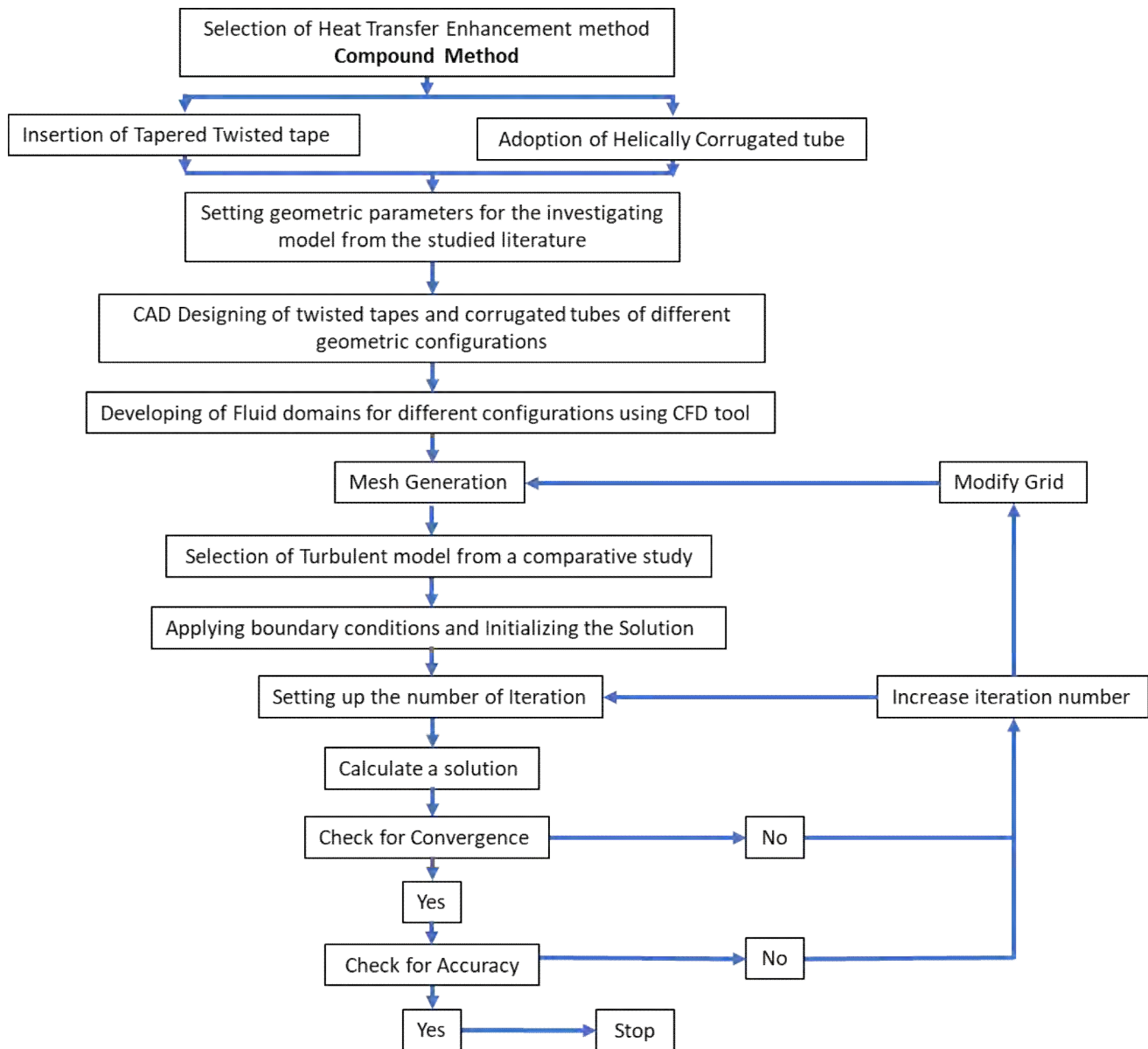
Fig. 4.5.1: Overview of the solution procedure of the present study

4.6 Data Analysis

As the constant wall heat flux (q) boundary condition is applied, the heat flux is obtained from the simulation. The convective heat transfer coefficient is calculated from

$$h = \frac{q}{T_w - T_b} \tag{28}$$

where, T_w is the area-weighted average wall temperature of the tube, and T_b is the mass-weighted average temperature of the fluid.

$$T_w = \frac{1}{A} \int T_{w,x} \partial A \tag{29}$$

$$T_b = \frac{\int \dot{m} C_p T}{\int \dot{m} C_p} \tag{30}$$

The Nusselt number is obtained from

$$Nu = \frac{hD}{k} \tag{31}$$

The friction factor f is determined from the pressure drop ΔP across the tube [33],

$$f = \frac{\Delta P}{\left(\frac{L}{D}\right)\left(\frac{\rho u^2}{2}\right)} \tag{32}$$

Thermal performance factor (η) is the enhancement of heat transfer obtained by using the enhancement method and is the ratio of normalized Nusselt number and normalized friction factor. However, to quantify the energy savings by using the enhancement method it needs to be compared for heat transfer enhancement at equal pumping power to that of the plain tube without adopting any enhancement method, below procedure. According to constant pumping power assessment criteria [40]

$$(\dot{V}\Delta P) = (\dot{V}\Delta P)_o \tag{33}$$

and the relationship between the friction factor and Reynolds number can be given as below:

$$(f Re^3) = (f Re^3)_o \tag{34}$$

$$Re = Re_o \left(\frac{f}{f_o}\right)^{1/3} \tag{35}$$

The thermal performance factor is obtained by

$$\eta = \frac{Nu}{Nu_o} / \left(\frac{f}{f_o}\right)^{1/3}$$ (36)

4.7 Validation of the model

In the present study, the numerical result of the present straight circular tube was obtained using the shear stress transport (SST) k-ω turbulent model. Using other numerical models i.e., standard k-ω turbulent model, standard k-ε turbulent model, and renormalized-group (RNG) k-ε turbulent model Nusselt number (Nu) and friction factor (f) have been calculated for the straight tube. The comparison of the outcomes from the turbulent models with empirical correlations Equation (37) and Equation (38) are shown in Fig. 4.7.1 and Fig. 4.7.2. Dittus-Boelter correlation and Petukhov correlation have been considered as the standard correlation for the Nusselt number and the friction factor respectively [28]. In both cases, the results of the heat transfer in terms of Nusselt number and the pressure drop in terms of friction factor obtained using the shear stress transport (SST) k-ω turbulent model are in good agreement with the empirical correlation. Table 7 shows the percentage of variation of Nusselt number (Nu) and friction factor (f) from the empirical correlations for the different turbulent models. The empirical correlations are given as follows:

$$Nu = 0.023\,Re^{0.8}\,Pr^{\,0.4}$$ (37)

$$f = (0.790\,\ln Re - 1.64)^{-2}$$ (38)
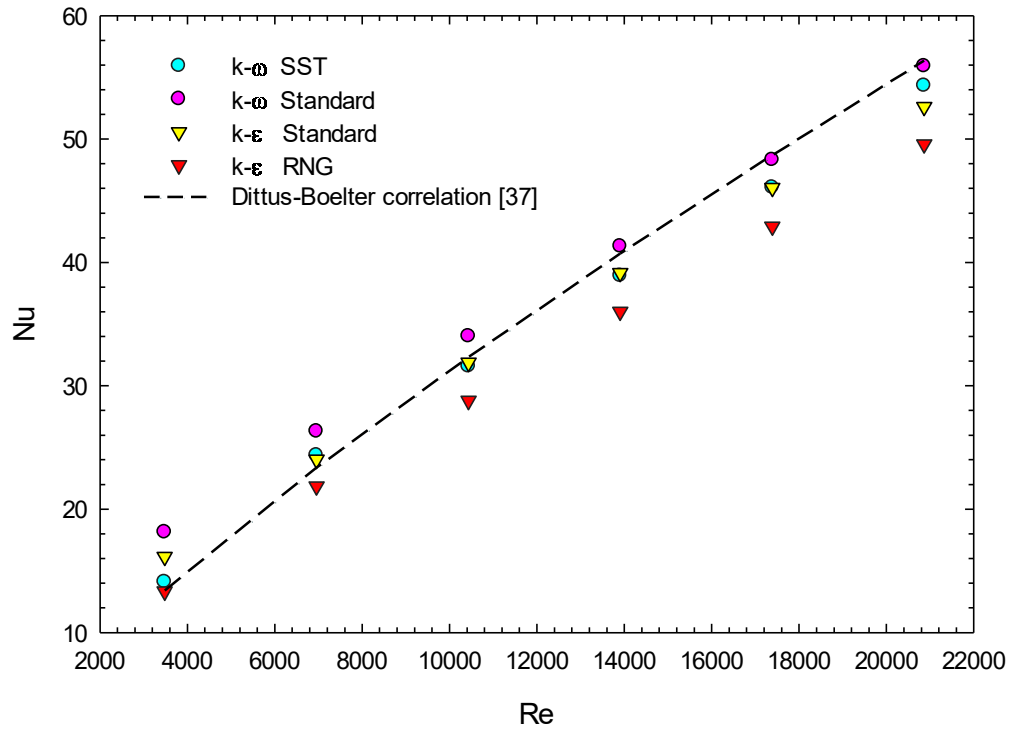
Fig. 4.7.1: Validation test of present CFD model with different turbulence model for Nusselt number.
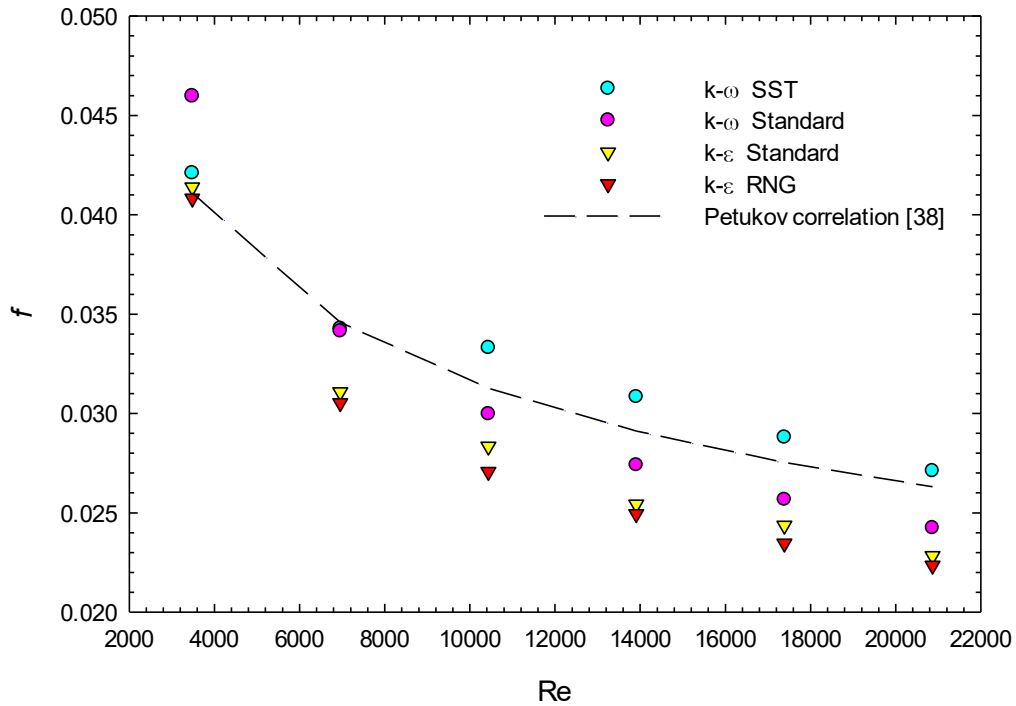
Fig. 4.7.2: Validation test of present CFD model with different turbulence model for friction factor.

Table 7: Percentage of deviation of obtained results from different turbulent models against empirical correlations [28]

Re	Deviation (%)							
	(SST) k-ω		(Standard) k-ω		(Standard) k-ϵ		(RNG) k-ϵ	
	Nu	f	Nu	f	Nu	f	Nu	f
3477	4.91	2.34	35.4	10.6	16.9	0.65	0.67	6.96
6955	4.02	0.91	12.5	1.29	2.63	11.32	7.05	14.33
10433	2.38	6.1	5.17	4.34	1.46	10.34	12.38	15.56
13910	4.64	5.58	1.43	6.21	4.02	14.48	14.11	16.71
17388	5.72	4.44	0.84	7.30	5.79	14.01	14.49	17.38
20866	4.74	2.92	0.83	8.54	7.19	15.25	14.72	17.77

The present numerical model has been compared with Piriyarungrod et *al.* [59] and Ramakumar et *al.* [41] for the tapered twisted tape inserts (y/w = 3.5, θ = 0º) and (y/w = 3.0, θ = 0.3º) inside the straight circular tube and found an average of 4% and 1.63% deviation on the normalized Nusselt number concerning Reynolds number, shown in Fig. 4.7.3. Subsequently, A comparison analysis is also conducted between the present computational model with Wang et *al.* [60] for the corrugated tube (Hl/D = 0.05, pl/D = 1.0), shown in Fig. 4.7.3, where an average of 3.65% deviation is found. Fig. 4.7.4 shows the comparative study of the normalized friction factor with Reynolds number for the present numerical model with Piriyarungrod et *al.* [59], Ramakumar et *al.* [41], and Wang et *al.* [60] for the straight twisted tape inserts (y/w = 3.5, θ = 0º), and tapered twisted tape insert ((y/w = 3.5, θ = 0.3º), inside a straight circular tube, and the corrugated tube (Hl/D = 0.05, pl/D = 1.0) respectively. About an average of 2.8%, 4.16%, and 3.2% deviation has been found on that comparative study for straight twisted tape, tapered twisted tape, and corrugated tube respectively. Thus, this accuracy provides reliable results for the heat transfer and the pressure drop in a straight circular tube, and the helically corrugated tubes with twisted tape inserts in this present study.
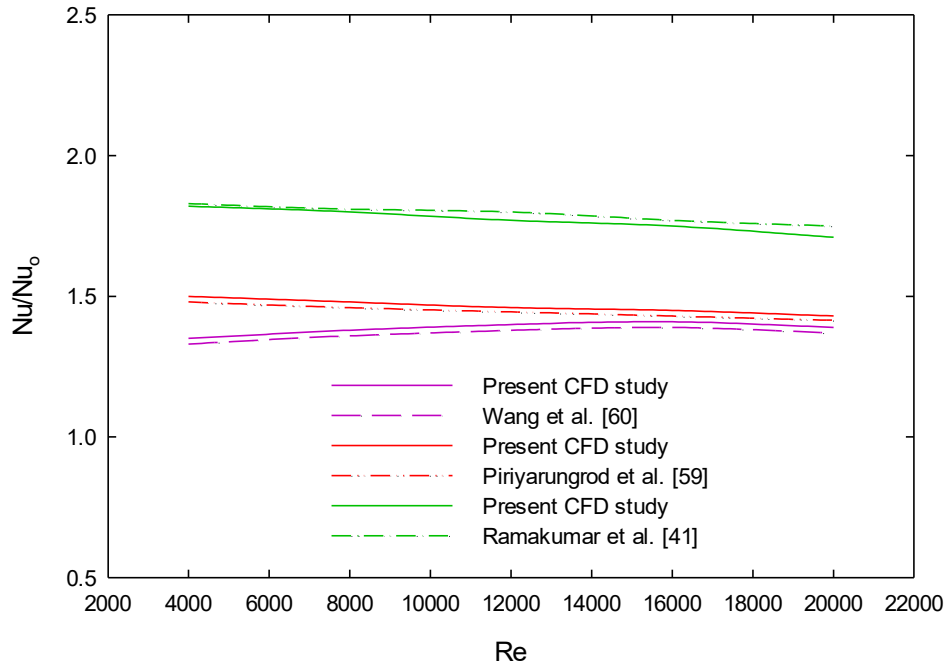
Fig. 4.7.3: Validation of the present CFD model against Wang et al. [60] (corrugated tube; Hl/D = 0.05, pl/D = 1.0), Piriyarungrod et al. [59] (straight twisted tape; y/w = 3.5, θ = 0°), and Ramakumar et al. [41] (tapered twisted tape y/w = 3.0, θ = 0.3°) for normalized Nusselt number.
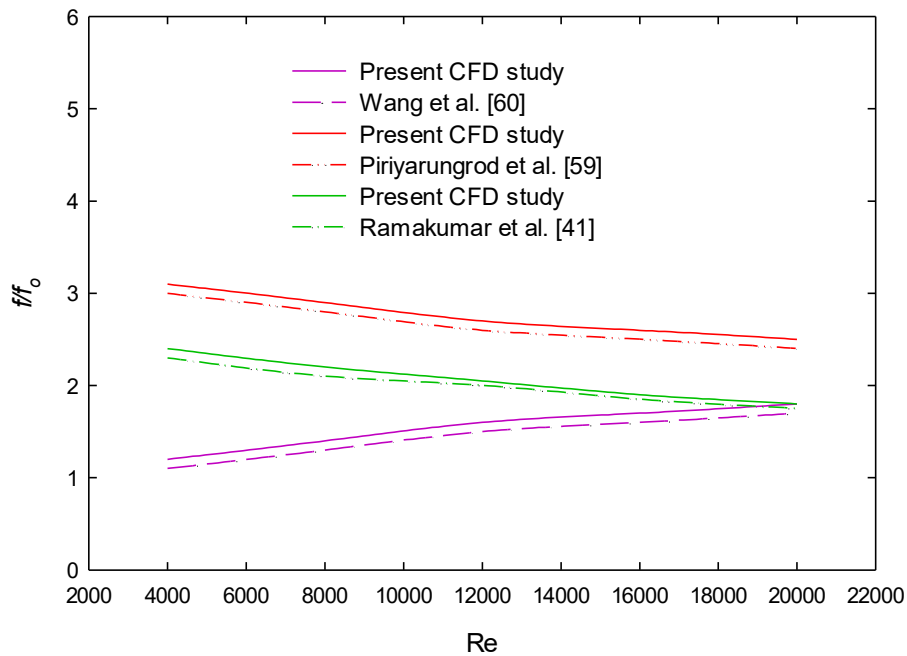
Fig. 4.7.4: Validation of the present CFD model against Wang et al. [60] (corrugated tube; Hl/D = 0.05, pl/D = 1.0), Piriyarungrod et al. [59] (straight twisted tape; y/w = 3.5, θ = 0°), and Ramakumar et al. [41] (tapered twisted tape y/w = 3.0, θ = 0.3°) for normalized friction factor.

CHAPTER 5

CFD Results

Different performance parameters such as flow characteristics, heat transfer characteristics, pressure drop characteristics, and overall performance enhancement characteristics have been investigated for turbulent flow ($3400 < Re < 21000$) through straight and corrugated tubes with twisted tape inserts. In this chapter, the evaluation of the following performance parameters are discussed elaborately.

5.1 Flow Characteristics

The flow structures are represented in the terms of streamline, velocity, and turbulent kinetic energy. In this study, the working fluid is flowing through the straight circular tube and the various corrugated tubes. These corrugated tubes are helically outward corrugated tubes with different pitch-length to tube-diameter ratios and different corrugation height-length to tube-diameter ratios. Moreover, tapered twisted tapes with different twist ratios and different tapered angles, are inserted into those tubes. These devices have made the fluid flow through sudden expanding and converging flow area which eventually results in an adverse pressure gradient region at the tube wall and the twisted tape wall. In the adverse pressure gradient region, centrifugal forces induce secondary flow. Furthermore, due to the frictional grip, a circumferential velocity component develops in the turbulent flow, as does a severely turbulent fluctuation between the fluid elements, which is represented by the turbulent kinetic energy (TKE). The secondary flow is a type of vortex that is separate from the mainstream fluid, whereas the rotational flow, which is primarily caused by the twisted tapes, is a type of flow that is present alongside the mainstream. Owing to this complex flow pattern, the flow resistance and the heat transfer are both improved significantly. To reveal the effect of the corrugation parameters and the twisted tapes parameters on the turbulent flow and other performance characteristics, this investigation has been conducted with the different parameters of twisted tapes and corrugated tubes. Fig. 5.1.1, represents the streamlines with fluid domain vectors for the case-30 ($y/w = 3.5$, $\theta = 0.3°$, $pl/D = 1.0$, $Hl/D = 0.1$) at $Re = 10433$ which has been investigated in this study. The insertion of twisted tapes inside the tubes decreases the flow area of the fluid that increases the fluid velocity, and it also guides the fluid to make a secondary flow by its twisted surface. However, the corrugated tubes are shaped into helically grooved at periodic intervals along the flow direction. These grooves make room for the fluid to

flow around the grooves, so the flow velocity at the grooves is a bit slower than the flow velocity at the annuli as shown in Fig. 5.1.1 by the greener region of the fluid domain. The corrugation on the tube and the twisted tape induces flow disturbance in the fluid domain. The streamline shows the swirl flow of the fluid inside the tubes. It is comprehensible that twisted tape inserts with the smaller twist ratios and the smaller tapered angles exhibit a higher amount of swirl in the fluid domain. Furthermore, it is visible from the Fig. 5.1.1 that the velocity of the mainstream is substantially high in between twisted tape and tube wall since the color of the streamline is denser in that region than the streamline of fluid near the wall.
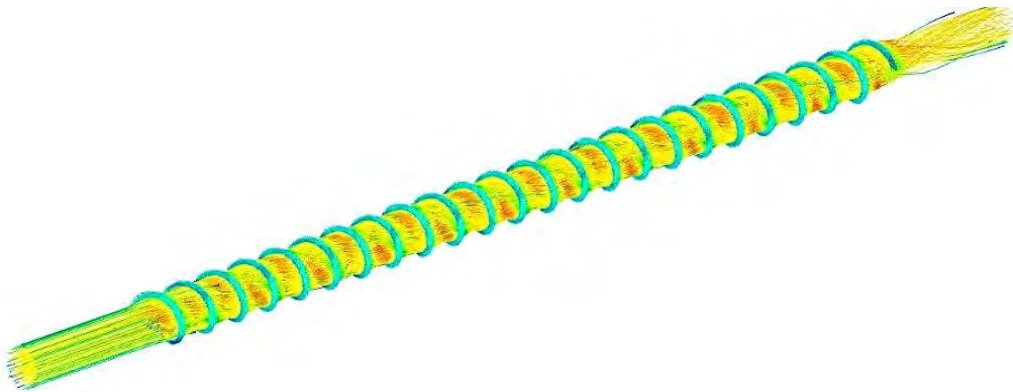
Fig. 5.1.1: Illustration of Streamline through a helically corrugated tube with twisted tape inserts; case-30 ($y/w = 3.5$, $\theta = 0.3°$, $pl/D = 1.0$, $Hl/D = 0.1$) at Re = 10433.

To understand the flow pattern, the velocity contour in the longitudinal section of six considered cases of different parameters among a total of 180 cases in correspondence with thirty different geometrical configurations for six different Reynolds numbers in the region from 3400 to 21000, are shown in Fig. 5.1.2. For all the considered cases the velocity of flow is higher in between the tube wall and the twisted tape surface. However, the velocity of flow is minimum at the near-wall region for all the cases. At the grooved section of the corrugated tube, the fluid flow gets a bit slower. Comparing Fig. 5.1.2 (a) and (d), the main difference of parameters in these two cases is the twist ratio of the twisted tape, and it is comprehensible that with a lower twist ratio the velocity of fluid flow has increased significantly. From Fig. 5.1.2 (b) and (e), it is can be comprehended that with the lower pitch-length-to-tube-diameter ratio of corrugated tube, the velocity of fluid flow at the grooved section gets slower than in the corrugated tube with a higher pitch-length-to-

tube-diameter ratio. A similar phenomenon is also seen for the lower height-length-to-tube-diameter ratio of corrugated tubes in Fig. 5.1.2 (c) and (f). Besides, the rotational flow is flowing through the grooved section of the corrugated tube at a lower velocity than the mainstream fluid flow. From the illustration of Fig. 5.1.2, it is visible that with the increase of tapered angle the velocity of flow reduces as the flow area increases. The maximum flow velocity is observed for the tapered angle 0° and the minimum flow velocity is observed at a tapered angle of 0.5°. Disturbance in the core fluid flow region is found minimal for the lowest tapered and the higher twist ratio. On the contrary, the lower twist ratio and the higher tapered angle of the twisted tape inserts cause maximum disturbance in the fluid flow region.

(a) Case-3: $y/w = 5$, $\theta = 0°$, $pl/D = 1.5$, $Hl/D = 0.1$ (b) Case-15: $y/w = 5$, $\theta = 0.3°$, $pl/D = 1.0$, $Hl/D = 0.1$ (c) Case- 7: $y/w = 5$, $\theta = 0.5°$, $pl/D = 1.5$. $Hl/D = 0.05$

(d) Case-18: $y/w = 3.5$, $\theta = 0°$, $pl/D = 1.5$, $Hl/D = 0.1$ (e) Case: 30 $y/w = 3.5$, $\theta = 0.3°$, $pl/D = 1.0$, $Hl/D = 0.1$ (f) Case-27: $y/w = 3.5$, $\theta = 0.5°$, $pl/D = 1.5$, $Hl/D = 0.05$
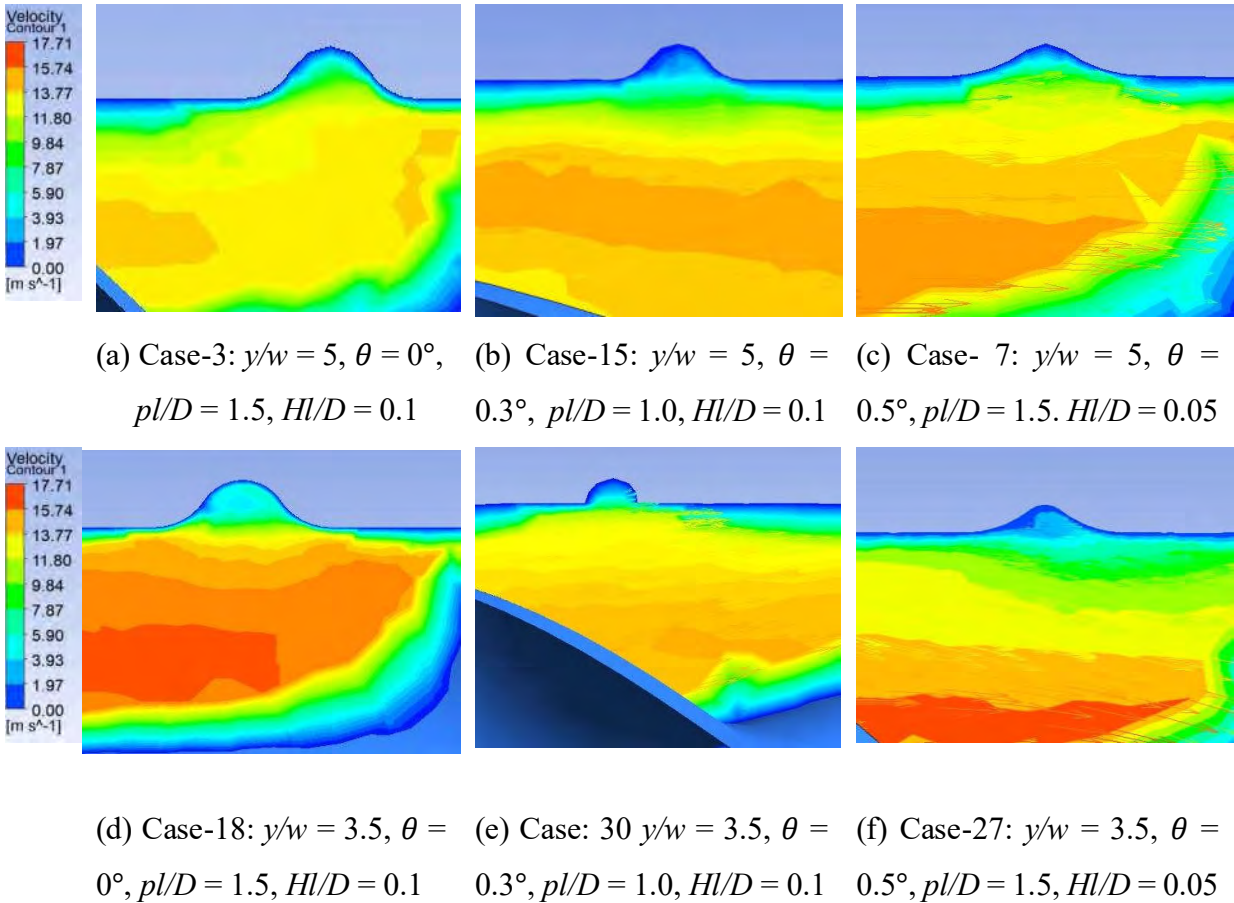
Fig. 5.1.2: Velocity contour at the longitudinal section for different cases at Re = 10433.

Turbulent kinetic energy (TKE) contours of selected cases are displayed in Fig. 5.1.3. Before the corrugation and the twisted tape section, turbulent kinetic energy is minimum at the core of the fluid domain. But the insertion of twisted tape inserts changes the scenario as the turbulent intensity

50

becomes higher in the core region at the twisted tape section of the tube. Moreover, the turbulent intensity gets higher when the fluid leaves the corrugated grooves at the tube surface than the fluid flowing near the smooth tube wall. However, it can be depicted from the figures in Fig. 5.1.3 that the fluid which has just entered the grooved section of the corrugated tube has significantly lower turbulent kinetic energy in all the cases. Higher turbulence indicates higher mixing of fluids at the core and the annuli, which will lead to better heat transfer. The size and height of the grooves of the corrugated tubes influence the disruption of the flow field near the wall which also aids to get higher heat transfer performance. In Fig. 5.1.3 (a) and (d), the difference between these two cases is the twist ratio of the twisted tape inserts. With the lower twist ratio of the tapes, the fluid has more turbulent kinetic energy than the twisted tapes with a higher twist ratio. Since the twisted tape with a lower twist ratio and lower tapered angle has reduced the flow area inside the tube which results in high velocity and high turbulent intensity. Comparing the figures in Fig. 5.1.3, it is easily understandable that with the decrease of tapered angle, the turbulent kinetic energy within the fluid decreased, since the flow area of the fluid has increased. The turbulent kinetic energy of the fluid near the twisted tape wall is higher than other wall adjacent regions. The fluid in the core region has less turbulent intensity and, for the cases of higher tapered angles, the low turbulence intensified regions are larger. Furthermore, the height-length-to-tube-diameter ratio of the corrugated tubes has a higher impact than the pitch-length-to-tube-diameter ratio of the corrugated tube. With a higher height-to-diameter ratio the fluid gets more flow area at the grooved so the velocity gets reduced in that region consequently the turbulent kinetic energy reduces in those regions. Therefore, it can be stated that a higher height-to-diameter ratio of the corrugated tube produces lower turbulent kinetic energy in the grooved sections of the tube.

(a) Case-3: $y/w = 5$, $\theta = 0°$, $pl/D = 1.5$, $Hl/D = 0.1$

(b) Case-15: $y/w = 5$, $\theta = 0.3°$, $pl/D = 1.0$, $Hl/D = 0.1$

(c) Case- 7: $y/w = 5$, $\theta = 0.5°$, $pl/D = 1.5$, $Hl/D = 0.05$

(d) Case-18: $y/w = 3.5$, $\theta = 0°$, $pl/D = 1.5$, $Hl/D = 0.1$

(e) Case: 30 $y/w = 3.5$, $\theta = 0.3°$, $pl/D = 1.0$, $Hl/D = 0.1$

(f) Case-27: $y/w = 3.5$, $\theta = 0.5°$, $pl/D = 1.5$, $Hl/D = 0.05$

Fig. 5.1.3: Turbulent kinetic energy (TKE) contour at longitudinal section for different cases at Re = 10433.
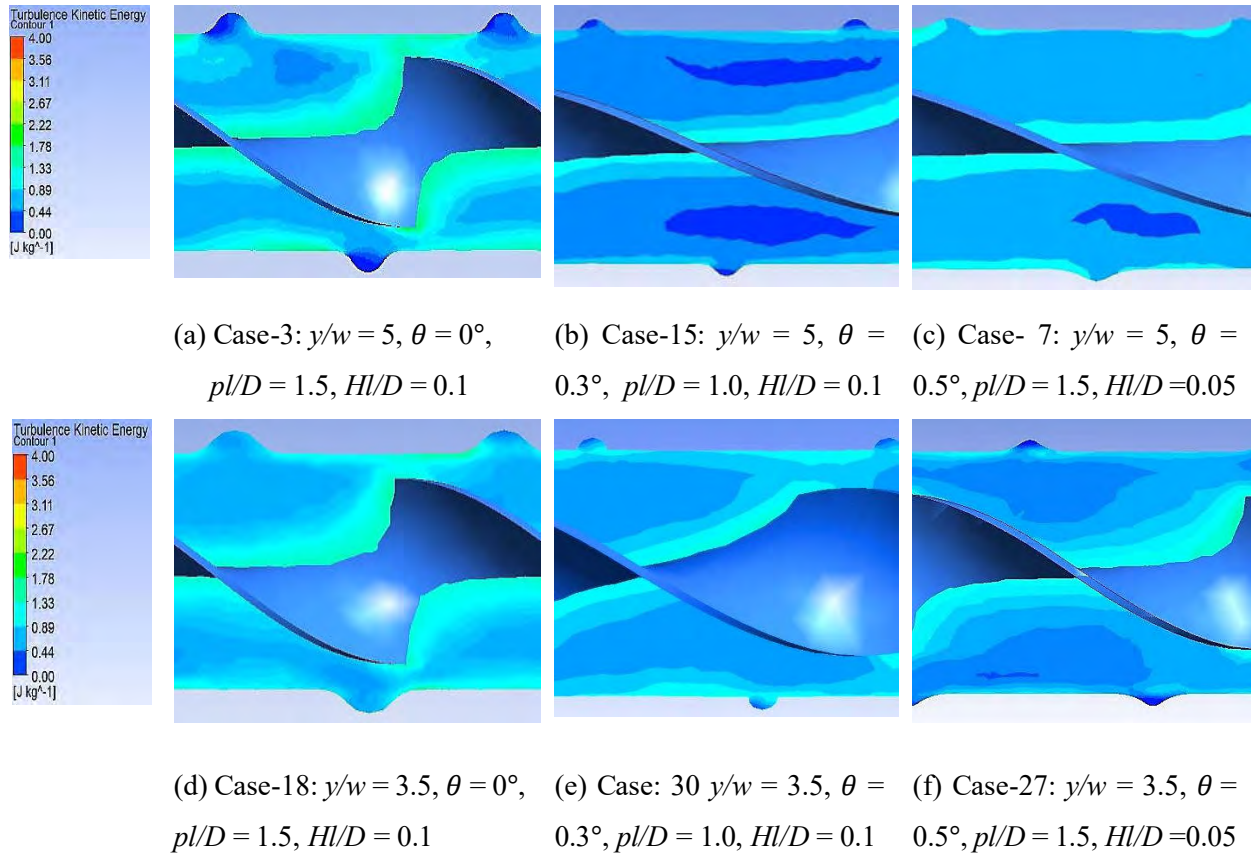
5.2 Heat Transfer Characteristics

A total number of 180 cases corresponding to thirty variations in one insert combination for six different Reynolds numbers from 3400 to 21000 have been studied in this study. The twisted tape inserts of the twist ratios *(y/w)* of 3.5 and 5, along with tapered angles *(θ)* of $0^o, 0.3^o,$ and 0.5^o have been inserted in the straight circular tube, and the corrugated tubes with pitch-length-to-tube-diameter ratios *(pl/D)* of 1.0 and 1.5, and height-length-to-tube-diameter ratios *(Hl/D)* of 0.05 and 0.1. Both twisted tape inserts and corrugated tubes influence the heat transfer enhancement of the heat exchanger. The helically corrugated tubes are shaped into a discrete groove in the tangential direction of the tube at a specific interval along the fluid flow direction. Fig. 5.2.1 represents the variance of normalized Nusselt number (Nu/Nu_o; the ratio of a helically corrugated tube with twisted tape insert's Nusselt number to straight circular tube without any turbulator's Nusselt number) with Reynolds number for twisted tape inserts with the twist ratio 3.5, and the tapered angles of $0^o, 0.3^o,$ and 0.5^o respectively. It can be observed from Fig. 5.2.1 (a) that the normalized Nusselt number is higher at lower Reynolds number for all the corrugated tubes where twisted tapes with the twist ratio of 3.5 and the tapered angle of 0° are inserted. However, with the increment of Reynolds number, the normalized Nusselt number gradually increases for all the studied cases showing a similar trend. The minimum heat transfer enhancement has been found for the straight circular tube (SCT) and the maximum heat transfer enhancement has been observed for the helically corrugated tube with the height-length-to-tube-diameter ratio of 0.1 and the pitch-length-to-tube-diameter ratio of 1.0. Considering Fig. 5.2.1 (b) which depicts the heat transfer enhancement for the twisted tapes with the twist ratio of 3.5 and the tapered angle of 0.3° inserted in all the investigated helically corrugated tubes and the straight circular tube. It can be understood from Fig. 5.2.1 that for the helically corrugated tube with the height-to-diameter ratio of 0.1 and the pitch-to-diameter ratio of 1.0, the heat transfer rate is significantly higher than the all-other cases. The lowest heat transfer enhancement has been found from Fig. 5.2.1 for the helically corrugated tube with the height-to-diameter ratio of 0.05 and the pitch-to-diameter ratio of 1.5. However, at the lowest Reynolds number and the highest Reynolds number, the straight circular tube exhibits the lowest heat transfer enhancement in terms of the normalized Nusselt number. Fig. 5.2.1 (c) shows the heat transfer enhancement for all the helically corrugated tubes and the straight circular tube in which twisted tapes with the twist ratio of 3.5 and the tapered angle of 0.5° are inserted.

Fig. 5.2.1: Variation of normalized Nusselt number with Reynolds number for different twisted tape inserts; (a) Twisted tape (y/w) = 3.5, (θ) = 0°; (b) Twisted tape (y/w) = 3.5, (θ) = 0.3°; (c) Twisted tape (y/w) = 3.5, (θ) = 0.5°.

At the lowest Reynolds number and the highest Reynolds number, the straight circular tube exhibits the lowest heat transfer enhancement in terms of the normalized Nusselt number. Moreover, the lowest heat transfer enhancement has been found from Fig. 5.2.1 for the helically corrugated tube with the height-length-to-tube-diameter ratio of 0.05 and the pitch-length-to-tube-diameter ratio of 1.5. In contrast, for the helically corrugated tube with the height-to-diameter ratio of 0.1 and the pitch-to-diameter ratio of 1.0, the heat transfer rate is significantly higher than the all-other investigated cases. Taking into account the figures in Fig. 5.2.1, it can be stated that with the increment of the height-length-to-tube-diameter ratio and the decrease of the pitch-length-to-tube-diameter ratio of the corrugated tubes, the turbulent heat transfer enhancement increases. On the other hand, a lower heat transfer rate can be found in the helically corrugated tube where the height-length-to-tube-diameter ratio is minimum and the pitch-to-diameter ratio is maximum. Besides, the helically corrugated tubes have exhibited better heat transfer enhancement characteristics over the straight circular tube.

Fig. 5.2.2 depicts the variation of normalized Nusselt number (Nu/Nu_o; the ratio of the helically corrugated tube with twisted tape insert's Nusselt number to straight circular tube without any turbulator's Nusselt number) with Reynolds number for twisted tape inserts with the twist ratio 5, and the tapered angles of 0°, 0.3^o, and 0.5^o respectively. A similar trend has been observed and the reasons are already discussed in context to Fig. 5.2.1. Now comparing the figures of Fig. 5.2.1 and Fig 5.2.2, it has been found that the twisted tapes with lower twist ratios give a higher heat transfer rate than the twisted tapes with relatively higher twist ratios. In this study, twisted tapes with twist ratios of 3.5, and 5, are inserted inside the straight circular tube, and the helically corrugated tubes. For each case, twisted tapes with a twist ratio of 3.5 exhibits a higher heat transfer rate over the twisted tapes with twist ratio 5, this analogy is also analogous to other studies [28-33]. With the lower twist ratio, the number of twists in a twisted tape increase, which eventually leads to higher flow disturbance inside the tube. Moreover, this also induces higher swirling inside the tube, so the fluid stays a bit more time closer to the heated tube wall. Since the fluid gets higher time to be in touch with the heated wall, the fluid can absorb more heat from the wall. In addition, higher swirling results in better mixing of the fluid near the wall, and, the fluid at the core of the tube.
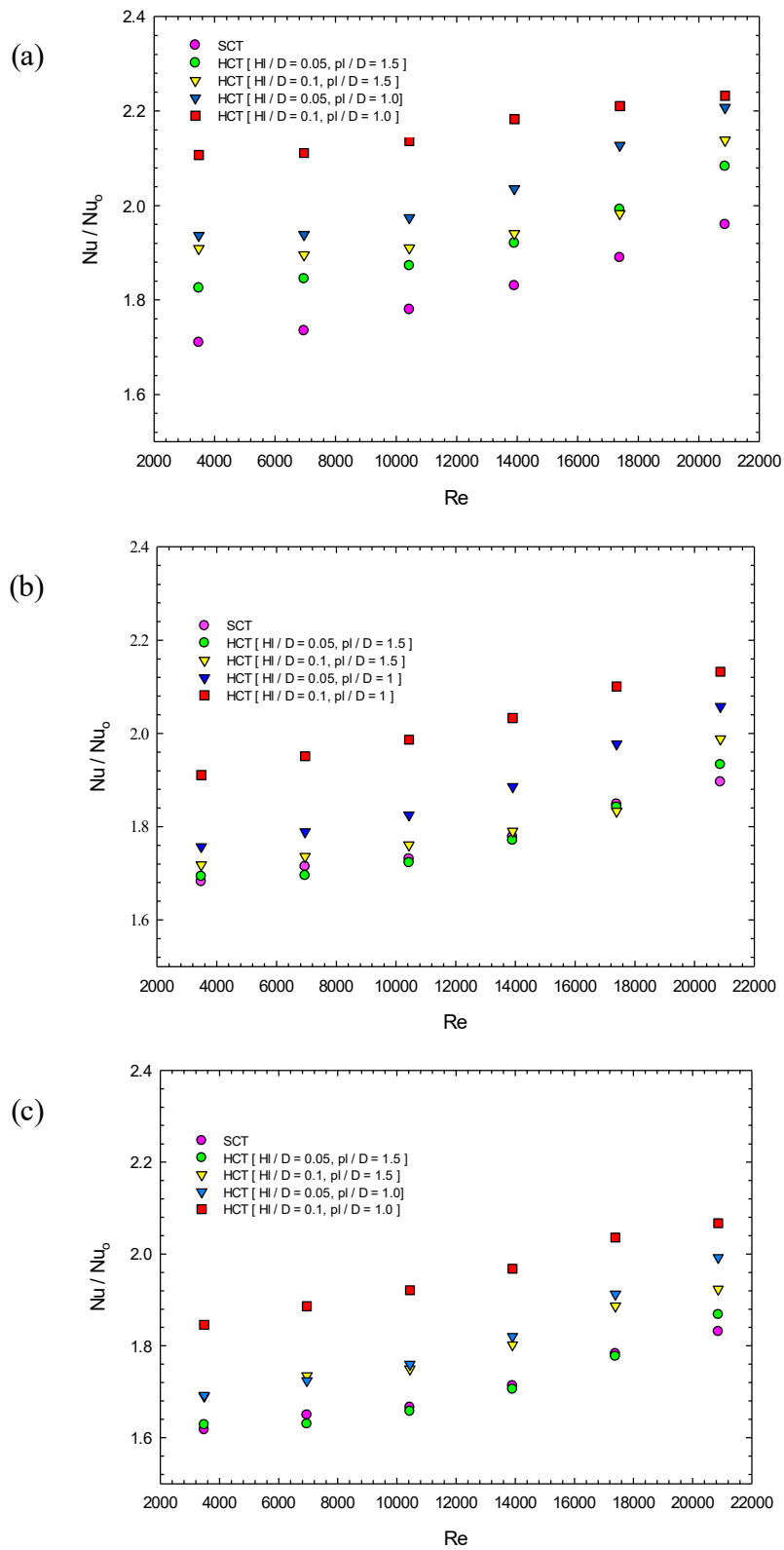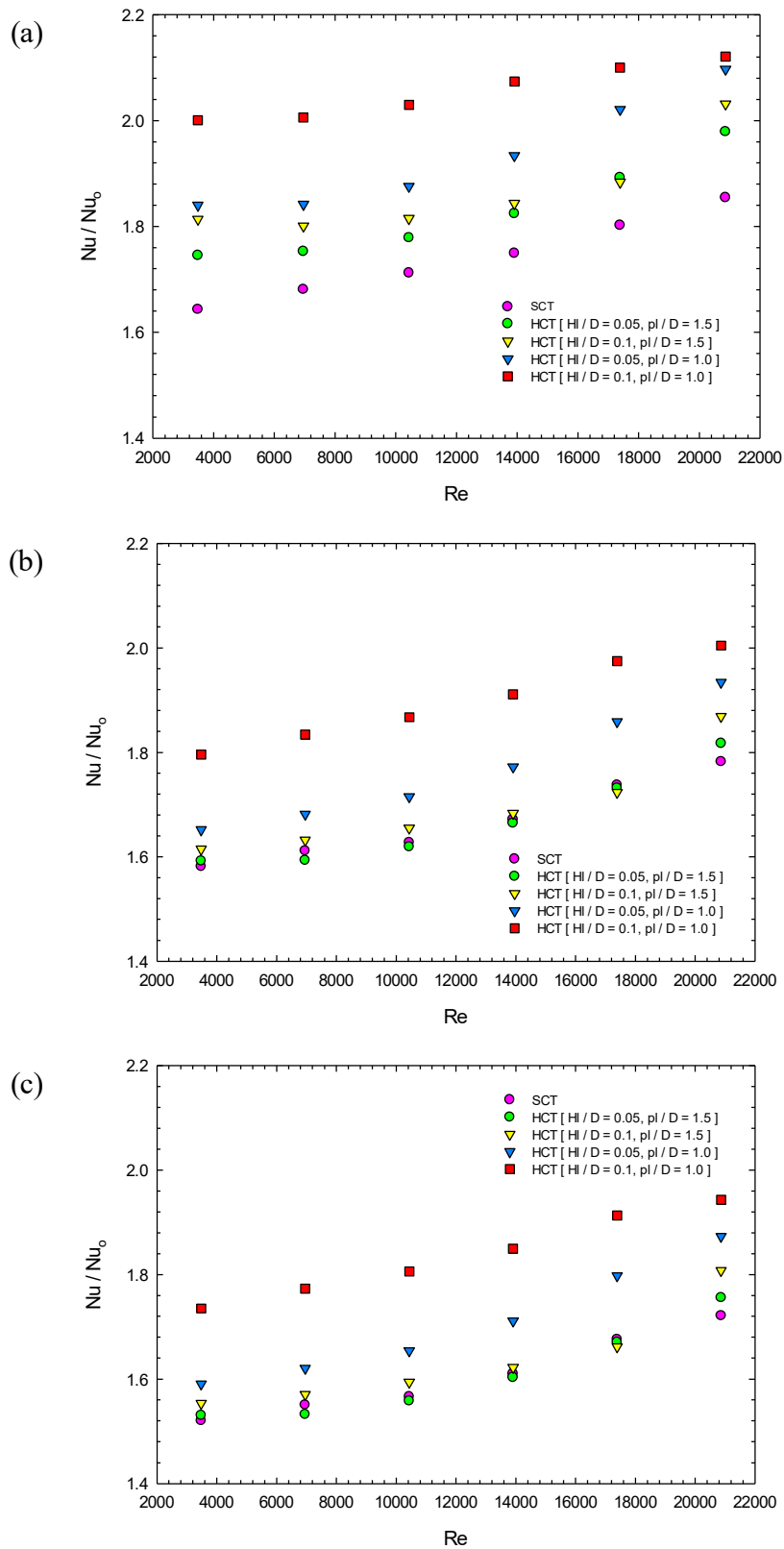
Fig. 5.2.1: Variation of normalized Nusselt number with Reynolds number for different twisted tape inserts; (a) Twisted tape (y/w) = 5, (θ) = 0°; (b) Twisted tape (y/w) = 5, (θ) = 0.3°; (c) Twisted tape (y/w) = 5, (θ) = 0.5°.

The above-mentioned phenomenon can also be figured out from Fig. 5.2.3, where temperature contours in the longitudinal direction at Re = 10433, for six different cases are presented.

(a) Case-3: y/w = 5, θ = 0°, pl/D = 1.5, Hl/D = 0.1

(b) Case-15: y/w = 5, θ = 0.3°, pl/D = 1.0, Hl/D = 0.1

(c) Case- 7: y/w = 5, θ = 0.5°, pl/D = 1.5. Hl/D = 0.05

(d) Case-18: y/w = 3.5, θ = 0°, pl/D = 1.5, Hl/D = 0.1

(e) Case: 30 y/w = 3.5, θ = 0.3°, pl/D = 1.0, Hl/D = 0.1

(f) Case-27: y/w = 3.5, θ = 0.5°, pl/D = 1.5, Hl/D = 0.05
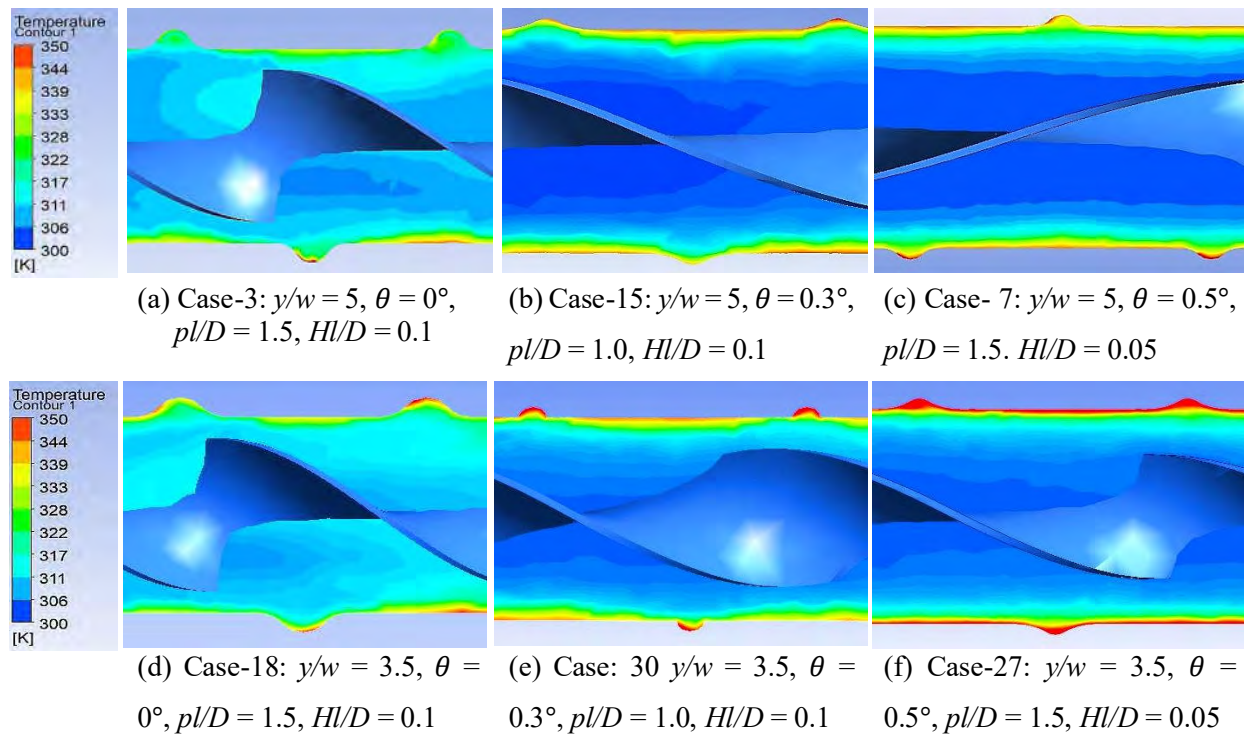
Fig. 5.2.3: Temperature contour at the longitudinal section for different cases at Re = 10433.

From Fig. 5.2.3, the effect of the tapered angles of twisted tapes is visible. The temperature of the fluid at the core of the tube is less than the fluid at the annuli of the tube since the heat is coming from the tube wall. The fluid finds more free space to flow, the tapered angle of the twisted tapes is higher. With smaller tapered angles, the fluid cannot move freely due to the obstruction of the twisted tape. Besides, the mixing of the fluid inside the tube reduces with the increase of the tapered angle of the twisted tapes. As a result, the temperature of the fluid at the center of the tube does not rise high enough that it rises with the smaller the tapered angles. From Fig. 5.2.3, it can be seen that the temperature of the fluid at the center of the tube is higher with the smaller tapered angles, and, lower with the higher tapered angle of the twisted tape. Consequently, it can be seen that the temperature of the fluid is higher with the twisted tape with a twist ratio of 3.5, and, lower with the twisted tapes with a twist ratio of 5. The effect of helically corrugated tubes on heat transfer enhancement is also visible in Fig 5.2.3. Comparing all the figures of Fig 5.2.3, it can be

apprehended that with a higher height-length-to-tube-diameter ratio *(Hl/D)*, the fluid near the wall gets more space and time, to flow around the wall which eventually leads to a higher heat transfer rate. As a result, the temperature of the fluid gets higher in corrugated tubes with a higher height-length-to-tube-diameter ratio *(Hl/D)* compared to the lower height-length-to-tube-diameter ratio *(Hl/D)*. These corrugations on the tube surface, generate a secondary flow that interrupts the thermal boundary layer of the fluid near to wall surface. In consequence, there is better mixing of fluid around the tube wall, and the fluid at the concentric region, which carries out better heat transfer from the heated tube wall to the fluid.

From Fig. 5.2.4, it has been observed that the normalized Nusselt number increases with the increase of turbulence in the fluid flow in terms of Reynolds number. The maximum heat transfer enhancement has occurred in the straight circular tube where the twisted tape inserts with *(y/w)* = 3.5, and $\theta = 0°$, in all the fluid flow regions. For this twisted tape insert, the maximum heat transfer enhancement of (Nu/Nu$_o$) nearly 1.85 has occurred for the maximum Reynolds number of the present investigation. The minimum amount of heat transfer enhancement has found in the straight circular tube where the twisted tape inserts with *(y/w)* = 5, and $\theta = 0.5°$ has been inserted. From Fig. 5.2.4 it is understandable that with the decrease of twist ratio, the heat transfer enhancement increases, and with an increase of twist ratio of the twisted tape inserts the heat transfer enhancement decreases [36-38].
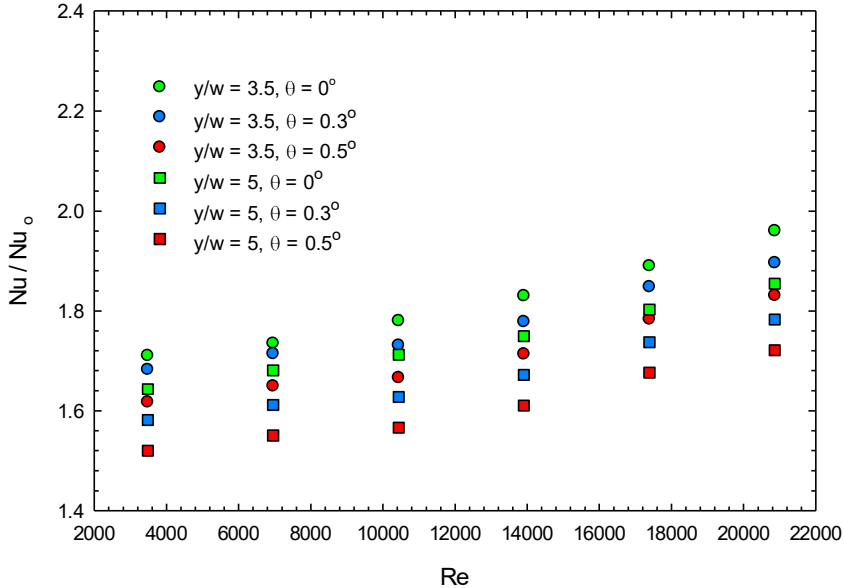

Fig. 5.2.4: Variation of normalized Nusselt number with Reynolds number in Straight Circular Tube (SCT), *(Hl/D)* = 0.0, *(pl/D)* = 0.0.

Fig. 5.2.5 depicts the variation of the normalized Nusselt number in terms of Reynolds number in the helically corrugated tube (HCT-1) with height-length-to-tube-diameter ratio (Hl/D) 0.05, and pitch-length-to-tube-diameter ratio (pl/D) 1.5. The maximum heat transfer enhancement of (Nu/Nu_o) 2.05 has been achieved in the corrugated tube where the twisted tape inserts with (y/w) = 3.5, and $\theta = 0°$, for the maximum Reynolds number in the present study. The minimum amount of heat transfer enhancement has found in this corrugated tube where the twisted tape inserts with (y/w) = 5, and $\theta = 0.5°$ has been inserted. It can be comprehended from Fig. 5.2.5 that with a lower twist ratio (y/w) and lower tapered angle (θ), the heat transfer enhancement is higher. On the contrary, with a higher twist ratio (y/w) and higher tapered angle (θ), the heat transfer enhancement is found lower though the turbulence in the fluid is similar for all the studied cases. Without changing the tapered angles, from Fig. 5.2.5 it is understandable that with the decrease of twist ratio, the heat transfer enhancement increases, and with an increase of twist ratio of the twisted tape inserts the heat transfer enhancement decreases. Subsequently, keeping the twist ratio of the twisted tape inserts unchanged, with the increase of tapered angles the heat transfer enhancement has been found to decrease.

A similar trend has been observed in Fig. 5.2.6, Fig. 5.2.7, and Fig. 5.2.8, where the variation of normalized Nusselt number in terms of Reynolds number have illustrated for HCT-2, HCT-3, and HCT-4, respectively, in context to Fig. 5.2.5. The twisted tape inserts with (y/w) = 3.5, and $\theta = 0°$, have exhibited maximum heat transfer enhancement in all the studied corrugated tubes. The maximum normalized Nusselt numbers of 2.1, 2.2, and 2.25 have been achieved for the HCT-2, HCT-3, and HCT-4, respectively. The reasons have already been discussed in context to Fig. 5.2.5.

Comparing the figures, Fig. 5.2.4, 5.2.5, Fig. 5.2.6, Fig. 5.2.7, and Fig. 5.2.8, it can be stated that the sole effect of the corrugated tube has contributed to the enhancement of heat transfer. Due to the grooves of the corrugated tube, the fluid flowing through the tube gets more space to flow around the tube absorbing more heat from the tube wall. Moreover, it interrupts the thermal boundary layer at the near-wall fluid. Among all the helically corrugated tubes, the turbulent fluid flow through the HCT-4 with height-length-to-tube-diameter ratio (Hl/D) 0.1, and pitch-length-to-tube-diameter ratio (pl/D) 1.0, exhibits maximum heat transfer enhancement in terms of normalized Nusselt number (Nu/Nu_o), for all the studied twisted tape configurations.

Fig. 5.2.5: Variation of normalized Nusselt number with Reynolds number in Helically Corrugated Tube (HCT-1), $(Hl/D) = 0.05$, $(pl/D) = 1.5$.

Fig. 5.2.6: Variation of normalized Nusselt number with Reynolds number in Helically Corrugated Tube (HCT-2), $(Hl/D) = 0.1$, $(pl/D) = 1.5$.
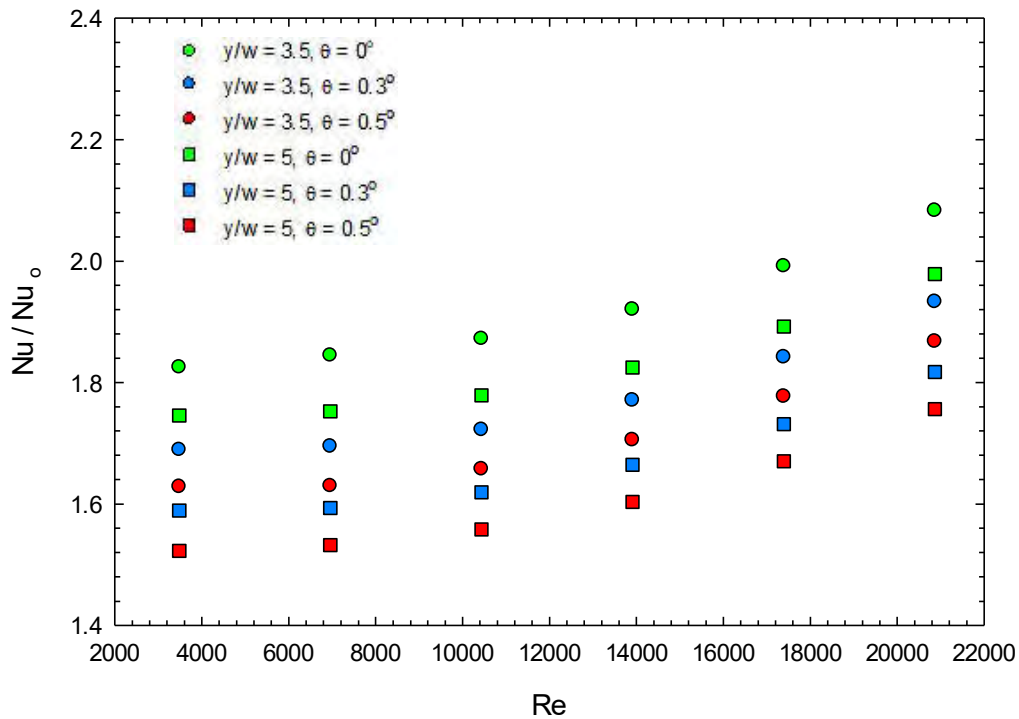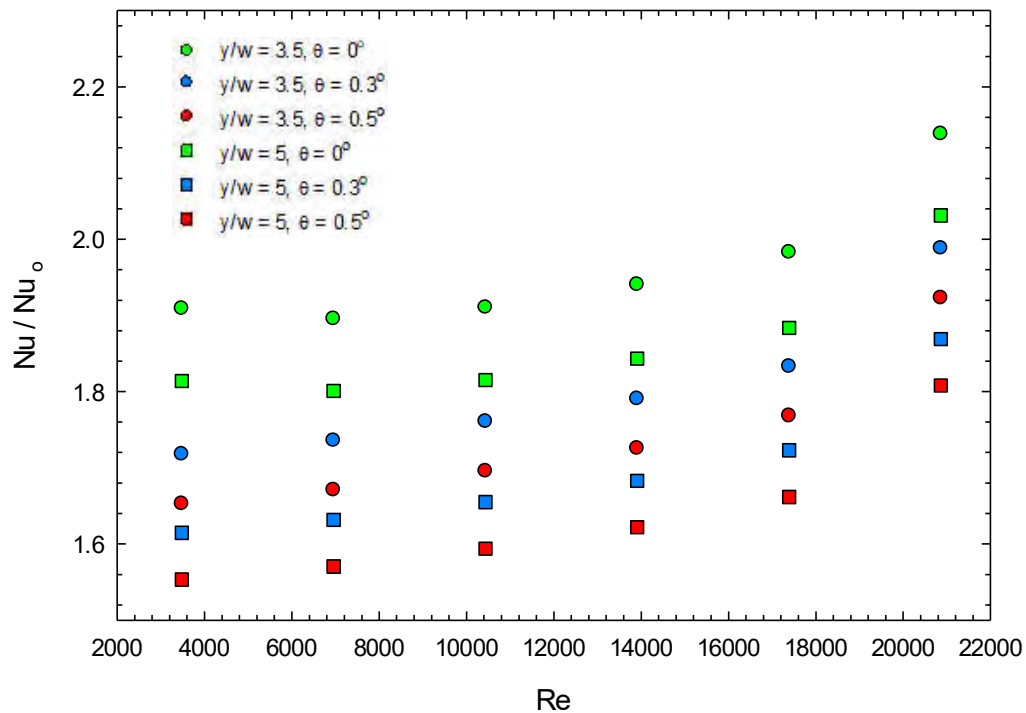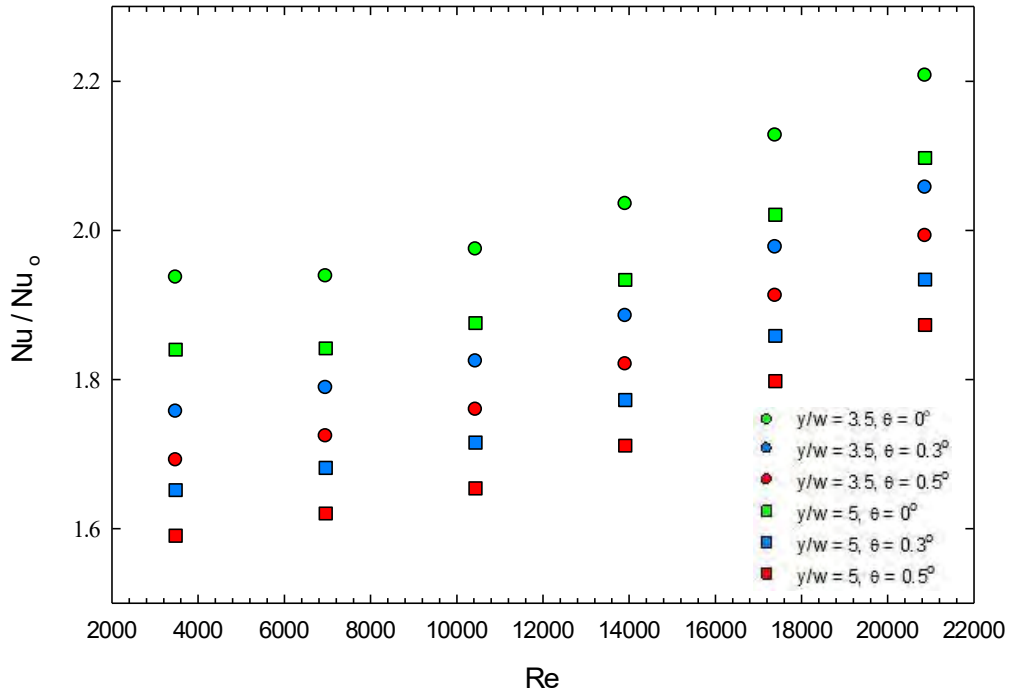
Fig. 5.2.7: Variation of normalized Nusselt number with Reynolds number in Helically Corrugated Tube (HCT-3), (Hl/D) = 0.05, (pl/D) = 1.0.
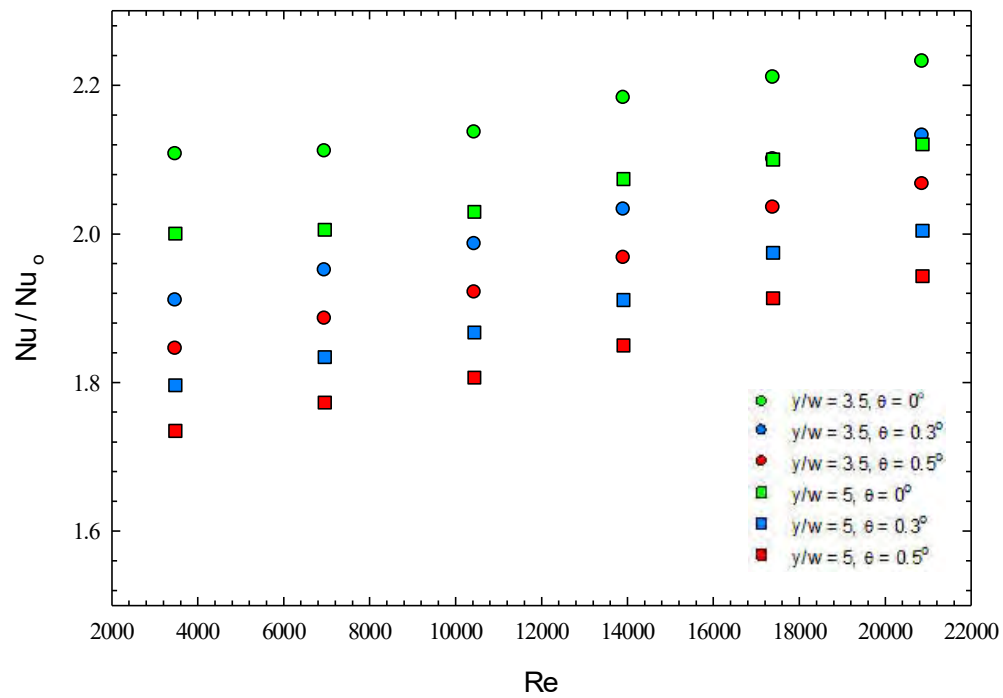

Fig. 5.2.8: Variation of normalized Nusselt number with Reynolds number in Helically Corrugated Tube (Hl/D): 0.1, (pl/D): 1.0.

61

5.3 Pressure Drop Characteristics

The pressure drop that occurs across the tubes has shown in Fig. 5.3.1, due to the congestion of fluid flow at the twisted tape's surface. Since there is no elevation between the inlet and the outlet of the tube, the increase in velocity causes the pressure drop according to Bernoulli's theorem. Earlier it has been discussed that the twisted tape inserts induce higher velocity in the fluid flow, it is also the reason for higher pressure drop across the tube. The insertion of twisted tapes has reduced the flow area inside the tube. From the continuity, it can be stated that with the reduction of flow area, the velocity of fluid increases. Consequently, the pressure drop across the tube increases as the velocity of the fluid has increased. In addition, the corrugated tubes generate swirls in the flow field and block the fluid at regular intervals. From the pressure contour, Fig. 5.3.1, it is visual that the pressure drop is higher at the grooved section of the surface of the corrugated tube. The effect of tapered angles of twisted tape inserts on pressure drop of fluid across the tube can be obtained from the individual comparison of Fig. 5.3.1 (a), (b), and (c), and Fig. 5.3.1 (d), (e), and (f). In the first comparison, in these three cases, the twist ratio of the twisted tapes is fixed, *(y/w)* = 5, but the tapered angles are 0°, 0.3°, and 0.5°, respectively. From Fig. 5.3.1 (a), (b), and (c), it is visual that the pressure drop across the tubes is decreased with the increase of tapered angle. Similarly in the second comparison among Fig. 5.3.1 (d), (e), and (f), where the twist ratio of the twisted tapes is fixed, *(y/w)* = 3.5, the pressure drop across the tubes is decreased with the increase of tapered angle. In addition, from the above-discussed figures, it can be found that the twisted tapes with a twist ratio of 3.5 cause more pressure drop than that the twisted tapes with a twist ratio of 5. Since with a lower twist ratio, the number of twists is higher in the twisted tape, which creates more congestion in the fluid flow area. This higher congestion in the flow area causes the pressure drop in the fluid flow across the tube. The lesser amount of pressure drop occurs where the twisted tape with twist ratio *(y/w)* is 5, and tapered angle *(θ)* is 0.5°, is inserted inside the tubes. Fig. 5.3.2, illustrates the pressure contours at the groove of corrugation at different positions of the corrugated tube in the flow direction. The pressure contour at the groove near the flow inlet, see Fig. 5.3.2 (a), has shown higher pressure by highlighted region. As the distance increases, the pressure at the grooves decreases gradually. Low-pressure region e has been found at the groove of corrugation near the flow outlet.

(a) Case-3: $y/w = 5$, $\theta = 0°$, $pl/D = 1.5$, $Hl/D = 0.1$

(b) Case-15: $y/w = 5$, $\theta = 0.3°$, $pl/D = 1.0$, $Hl/D = 0.1$

(c) Case- 7: $y/w = 5$, $\theta = 0.5°$, $pl/D = 1.5$, $Hl/D = 0.05$

(d) Case-18: $y/w = 3.5$, $\theta = 0°$, $pl/D = 1.5$, $Hl/D = 0.1$

(e) Case: 30: $y/w = 3.5$, $\theta = 0.3°$, $pl/D = 1.0$, $Hl/D = 0.1$

(f) Case-27: $y/w = 3.5$, $\theta = 0.5°$, $pl/D = 1.5$, $Hl/D = 0.05$
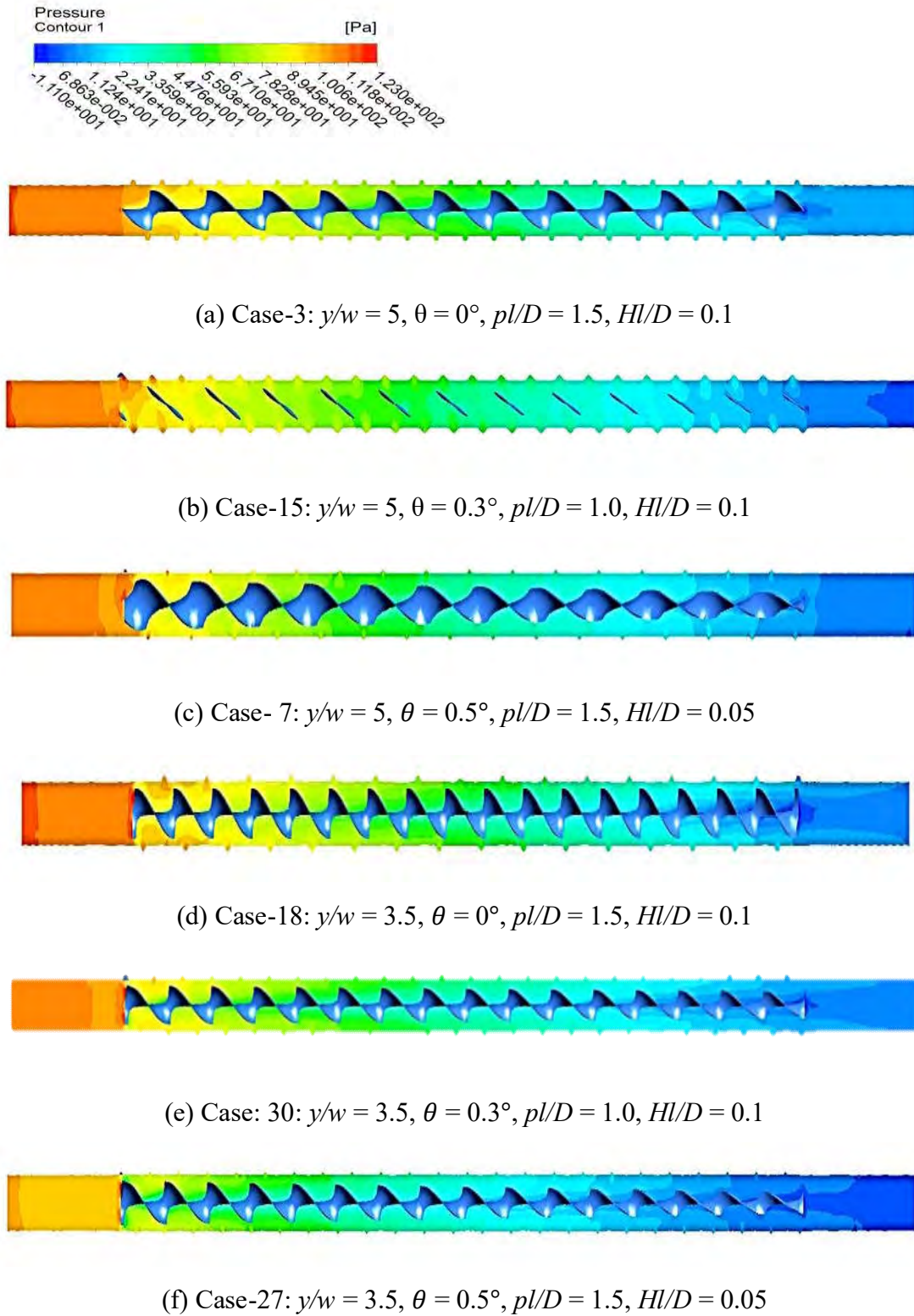
Fig. 5.3.1: Pressure contour at longitudinal section for different cases at Re = 10433.

(a) Distance from flow inlet, x = 125 mm   (b) Distance from flow inlet, x = 275 mm

(c) Distance from flow inlet, x = 525 mm   (d) Distance from flow inlet, x = 675 mm

$y/w = 3.5$, $\theta = 0.5°$, $Hl/D = 0.05$, $pl/D = 1.0$, at Re = 20866
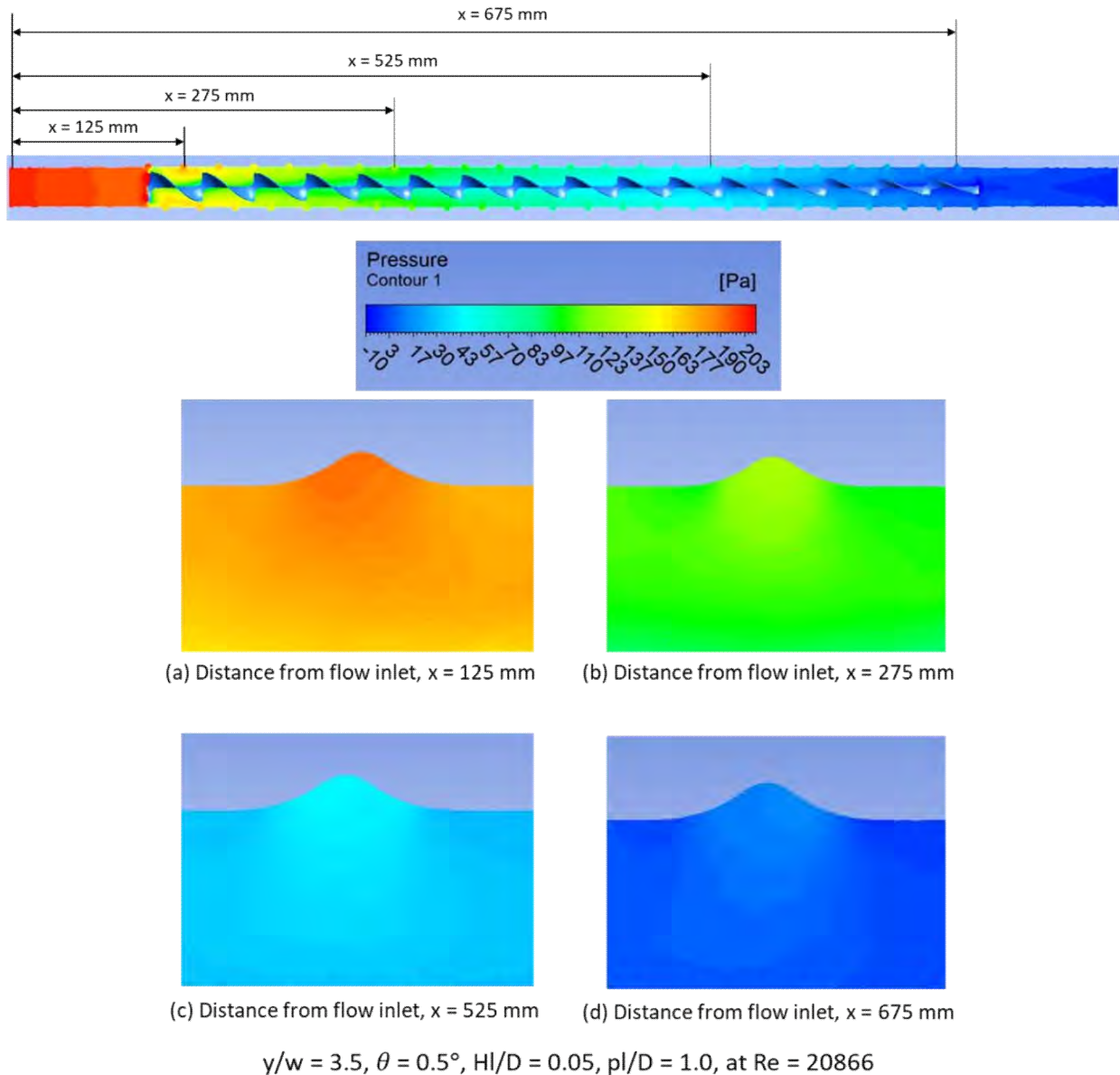
Fig. 5.3.2: Pressure contours at the grooves of the corrugated tube at different positions.

Fig. 5.3.3 represents the variation of normalized friction factor (f/f_o), (ratio of friction factor for helically corrugated tube with twisted tape inserts to the friction factor of the straight circular tube without twisted tape inserts) concerning Reynolds number for the twisted tapes with twist ratio of 3.5 are inserted in the smooth tube and the helically corrugated tubes. Here the friction factor represents the dimensionless pressure drop characteristics and the Reynolds number indicates the level of the fluid's turbulence. The pattern from Fig. 5.3.3, comprehend that the friction factor decreases with the increase of turbulence in the fluid flow. In addition, the effect of the pitch-to-diameter ratio *(pl/D)*, and the height-to-diameter ratio *(Hl/D)* of the corrugated tubes on the friction

factor is indicated in the figure. From Fig. 5.3.3 (a), (b), and (c), the effect of tapered angles of the twisted tapes on friction factor can be interpreted. Fig. 5.3.3 (a) depicts the variation of normalized friction factor to the Reynolds number for the twisted tape with a twist ratio of 3.5, and the tapered angle of 0°. From this figure, it is seen that the corrugated tube with *(Hl/D)* = 0.1 and *(pl/D)* = 1.5 gives a considerable amount of higher normalized friction factor than the other corrugated tubes. The minimum amount of friction factor is produced from the straight circular tube compared to other tubes. The corrugated tube with *(Hl/D)* = 0.1 and *(pl/D)* = 1.5, has the highest height and the pitch length, which causes a maximum friction factor of, nearly 6.8, for the minimum Reynolds number. Besides, the corrugated tube with *(Hl/D)* = 0.05 and *(pl/D)* = 1.5, has shown second-highest friction factor among all the tubes. It can be understood that the higher pitch length to diameter ratio, causes a higher friction factor in the tubes. On the other hand, the corrugated tubes with *(pl/D)* = 1.0, cause a comparatively lower friction factor, though the number of grooves in the tubes is higher. The corrugated tube with *(Hl/D)* = 0.05 and *(pl/D)* = 1.0, has a low impact on inducing friction faction compared to other corrugated tubes. Since in this case, the grooves' height is not much high, and the distance between two grooves is not long enough to causes more friction factors. A similar scenario is found in Fig. 5.3.3 (b) the which illustrates the variation of normalized friction factor to the Reynolds number for the twisted tape with twist ratio 3.5, and the tapered angle of 0.3°, and the Fig. 5.3.3 (c) which shows the variation of normalized friction factor to the Reynolds number for the twisted tape with twist ratio 3.5, and the tapered angle of 0.5°. For Fig. 5.3.2 (b), the maximum friction factor is obtained about 5.6 by the helically corrugated tube with *(Hl/D)* = 0.05 and *(pl/D)* = 1.5, and, the lowest friction factor is achieved nearly 5.9 by the straight circular tube, for Reynolds number 3477. Whereas for the twisted with the same twist ratio

Fig. 5.3.3: Variation of normalized friction factor with Reynolds number for different twisted tape inserts; (a) Twisted tape (y/w) = 3.5, (θ) = 0°; (b) Twisted tape (y/w) = 3.5, (θ) = 0.3°; (c) Twisted tape (y/w) = 3.5, (θ) = 0.5°.

but the different tapered angle of 0.5°, the helically corrugated tube with *(Hl/D)* = 0.05 and *(pl/D)* = 1.5, has obtained friction factor of 4, in Fig. 5.3.3 (c), for the same Reynolds number. From this analogy it can be stated that decreasing the tapered angle of twisted tapes, has significantly reduced the friction factor, thus the overall pressure-drop inside the tube.

Fig. 5.3.4 represents the variation of normalized friction factor *(f/f$_o$)*, (ratio of friction factor for the helically corrugated tubes with twisted tape inserts to the friction factor of the straight circular tube without twisted tape inserts) concerning Reynolds number for different studied configurations, for the twisted tape with twist ratio 5 inserted in the smooth tube and the helically corrugated tubes. In this study, twisted tapes with different tapered angles of 0°, 0.3°, and 0.5°, are introduced inside the helically corrugated tubes, and the straight circular tube. The effect of different tapered angles with the same twist ratio of twisted tape inserts on friction factor is illustrated in Fig. 5.3.4 (a), (b), and (c). The highest friction factor is obtained close to 6.7 by the helically corrugated tube with *(Hl/D)* = 0.1 and *(pl/D)* = 1.5, where twisted tape with the twist ratio 5, and the tapered angle of 0°, from Fig. 5.3.3 (a). The straight circular tube achieved the minimum friction factor of 5.2, for Reynolds number 3477. From the figures, Fig. 5.3.4 (a), (b), and (c), a similar trend in graphs is found, where the friction factor reduces with the increase of Reynolds number. Fig. 5.3.4 (c) depicts that the maximum friction factor is achieved by nearly 4 for the helically corrugated tube with *(Hl/D)* = 0.1 and *(pl/D)* = 1.5, for Reynolds number 3477. Comparing the peak points of Fig. 5.3.4 (a) and (c), it can be stated that simply increasing the tapered angle of the twisted tapes has a prominent effect on reduced friction factor. The friction factor has dropped from 6.8 to 4, by increasing the tapered angle from 0° to 0.5°. This simple modification in the geometry of twisted tape inserts has solved the issue of pressure drop of fluid inside the tubes.

Moreover, comparing all the figures of Fig. 5.3.3 and Fig. 5.3.4, it can be comprehended that, the twisted tape inserts with the twist ratio of 3.5, cause more pressure drop than the twisted tape inserts with the twist ratio of 5. Since, the number of twists in the twisted tape is higher in the twisted tapes with the twist ratio of 3.5, which causes more blockage in the fluid flow region. This ultimately causes a higher friction factor. On the contrary, with lower number twists the twisted tape inserts allow more space for the fluid to flow uninterruptedly. This leads to a lower pressure drop inside the tubes.
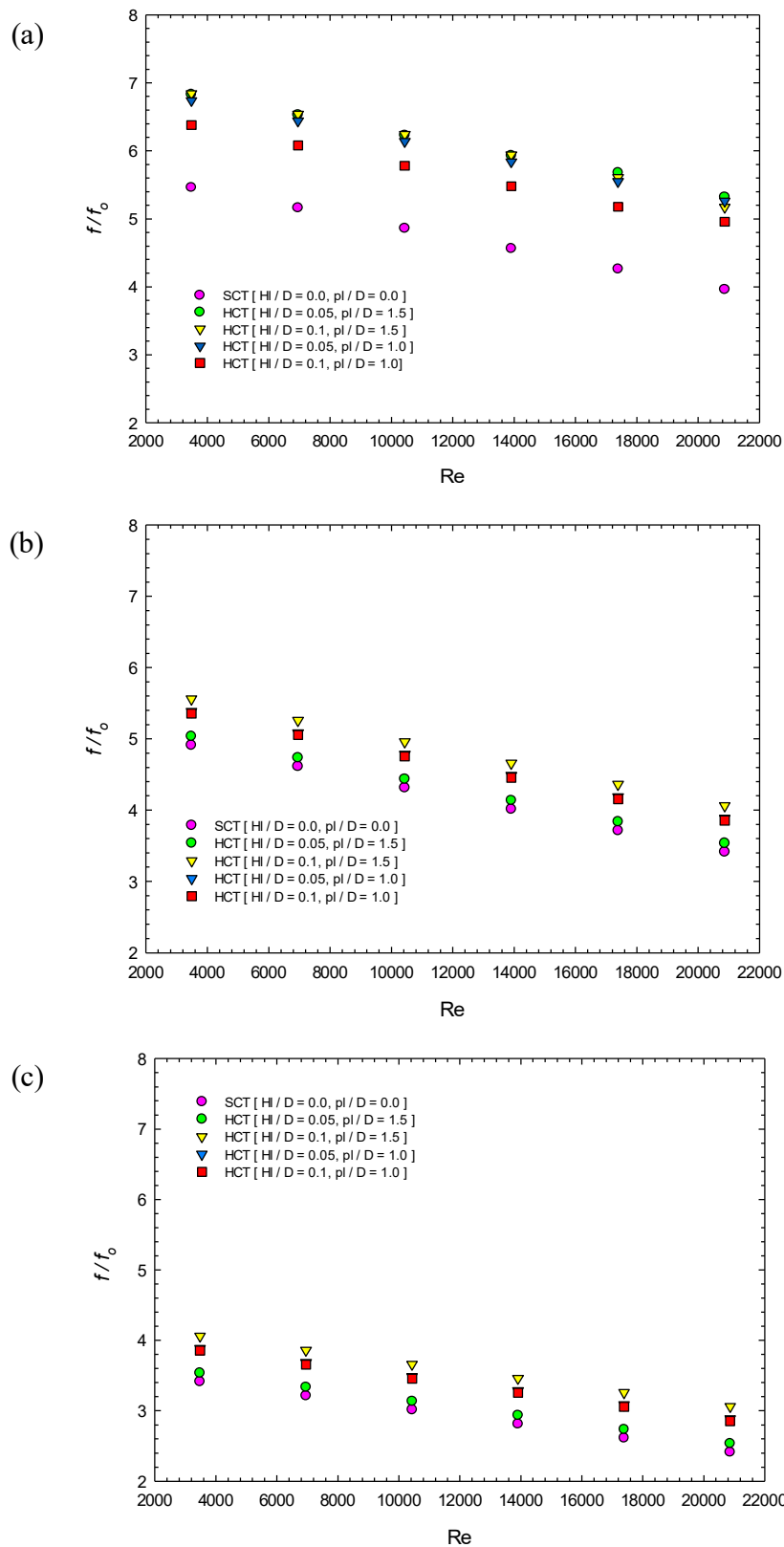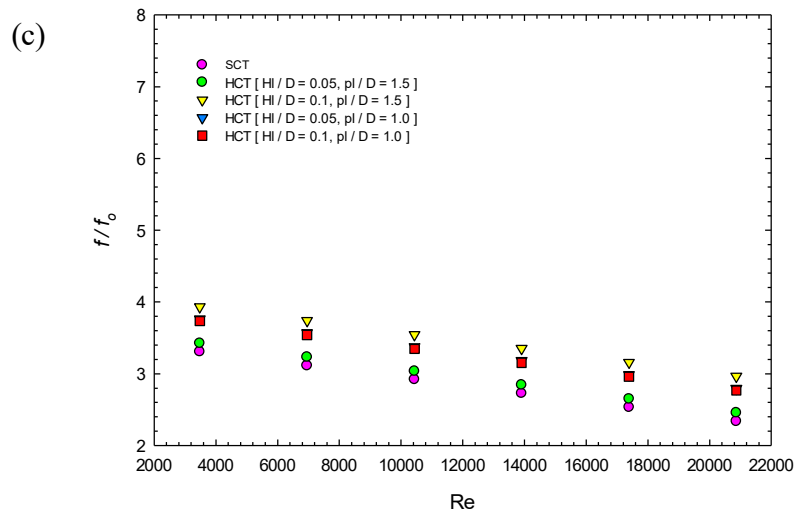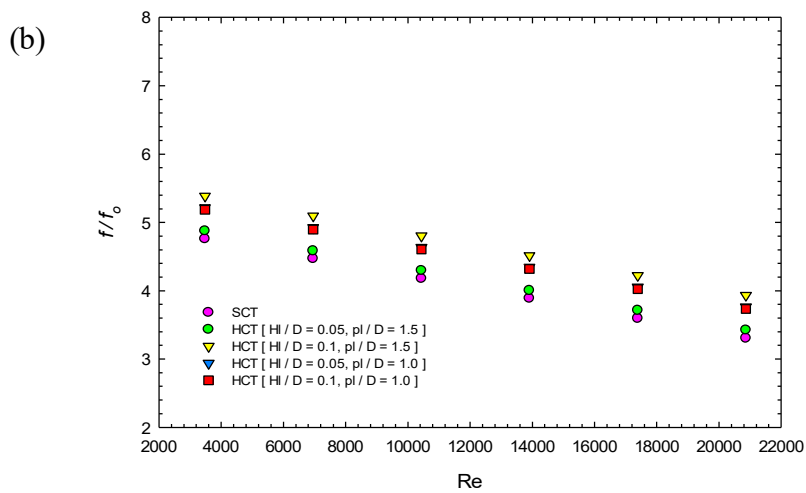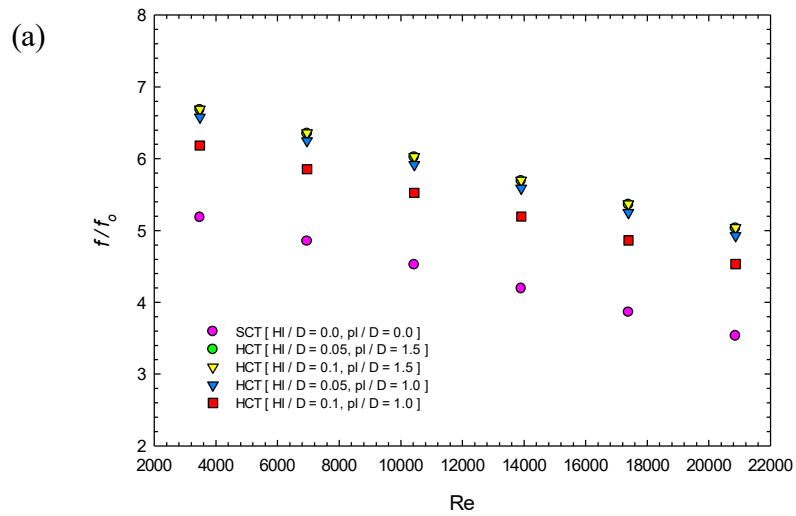
Fig. 5.3.4: Variation of normalized friction factor with Reynolds number for different twisted tape inserts; (a) Twisted tape $(y/w) = 5$, $(\theta) = 0°$; (b) Twisted tape $(y/w) = 5$, $(\theta) = 0.3°$; (c) Twisted tape $(y/w) = 5$, $(\theta) = 0.5°$.

Fig. 5.3.5, depicts the variation of normalized friction factor in terms of Reynolds number, where the normalized friction factor for the straight circular tube decreases with the increase of Reynolds number. This indicates that with the increasing turbulence in the fluid flow, the pressure drop reduces. From Fig. 5.3.5, it can be comprehended that the insertion of twisted tapes as turbulator in the straight circular tube (SCT), enhances the pressure drop in fluid flow compared to the straight circular tube without any turbulator. This enhancement in pressure drop has been denoted as the normalized friction factor. The maximum friction factor has found for the twisted tape with $(y/w) = 3.5$ and $(\theta) = 0°$, is close to 5.6. Whilst the normalized friction factor dropped to 5.2, for the same Reynolds number, when the twisted tape with $(y/w) = 5$ and $(\theta) = 0°$ is inserted into the straight circular tube. An increase in the twist ratio refers to the lower number of twists in the twisted tape. The secondary flow generation has decreased since the number of twists in the twisted tape reduced, so less swirling is induced inside the tube. All these results in reduced normalized friction factor. Besides, it has been found from Fig. 5.3.5, that increasing the tapered angle (θ) assisted in reducing the normalized friction factor. The width of the twisted tape gradually reduced along the flow path according to its tapered angle. Since the width of the twisted tape has reduced, the turbulent fluid flow gets more flow area. Therefore, the pressure drop in terms of normalized friction factor has decreased for increasing the tapered angle of the twisted tape inserts. It has seen from Fig. 5.3.5 that the minimum normalized friction factor 2.35, has been found for the twisted tape with $(y/w) = 5$ and $(\theta) = 0.5°$.
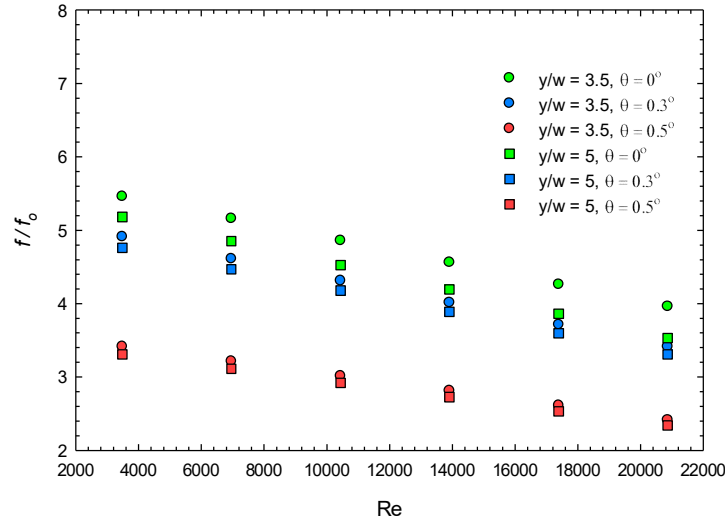
Fig. 5.3.5: Variation of normalized friction factor with Reynolds number in Straight Circular Tube (SCT), $(Hl/D) = 0.0$, $(pl/D) = 0.0$.

Fig. 5.3.6, illustrates the variation of normalized friction factor in terms of Reynolds number for the helically corrugated tube with $(Hl/D) = 0.05$, $(pl/D) = 1.5$. From this Fig. 5.3.6, it has been seen that all the studied twisted tape inserts which are inserted into the tube (HCT-1), are showing an identical trend. The normalized friction factor is decreasing with the increase of turbulence in the fluid flow in terms of Reynolds number. It can be significantly distinguished the effect of different tapered angles of twisted tapes in the normalized friction factor in the present study. With the increase of tapered angle of the twisted tape inserts, the normalized friction factor has significantly dropped, whether the twist ratio has been kept unaltered. The highest normalized friction factor, 6.9 has achieved by the twisted tape insert $(y/w) = 3.5$, $(\theta) = 0°$; (Re = 3477). Moreover, changing the tapered angle from 0° to 0.3° the normalized friction factor 5.1 has been found for the same Reynolds number (Re = 3477). The normalized friction factor of 3.6 has found for the twisted tape insert $(y/w) = 3.5$, $(\theta) = 0.5°$, keeping the same Reynolds number. Besides, changing the twist ratio of the twisted tape has less effect on reducing pressure drop in fluid flow in terms of normalized friction factor compared to the tapered angle. The normalized friction factor of nearly 6.7 has found for twisted tape insert $(y/w) = 5$, $(\theta) = 0°$; (Re = 3477), which is less than the twisted tape with twist ratio $(y/w) = 3.5$, $(\theta) = 0°$. Similarly in other cases which are illustrated in this figure, have found that the normalized friction factor has decreased with the increase of twist ratio of the twisted tape. The minimum amount of normalized friction factor has found 2.4 for the twisted tape insert $(y/w) = 5$, $(\theta) = 0.5°$; for the maximum Reynolds number 20,866.

Fig. 5.3.7, shows the variation of normalized friction factor with Reynolds number for the helically corrugated tube with $(Hl/D) = 0.1$, $(pl/D) = 1.5$. Here, the highest normalized friction factor, 6.7 has achieved by the twisted tape insert $(y/w) = 3.5$, $(\theta) = 0°$; (Re = 3477). Moreover, changing the tapered angle from 0° to 0.3° the normalized friction factor 5.6 has been found for the same Reynolds number (Re = 3477). The normalized friction factor of 5.1 has found for the twisted tape insert $(y/w) = 3.5$, $(\theta) = 0.5°$, keeping the same Reynolds number. Besides, the normalized friction factor of nearly 6.5 has been found for twisted tape insert $(y/w) = 5$, $(\theta) = 0°$; (Re = 3477), which is less than the twisted tape with a twist ratio of 3.5. Whilst the minimum amount of normalized friction factor has found 3 for the twisted tape insert $(y/w) = 5$, $(\theta) = 0.5°$; for the maximum Reynolds number of 20,866.

Fig. 5.3.6: Variation of normalized friction factor with Reynolds number in Helically Corrugated Tube (HCT-1), $(Hl/D = 0.05$, $pl/D = 1.5)$.

Fig. 5.3.7: Variation of normalized friction factor with Reynolds number in Helically Corrugated Tube (HCT-2), ($Hl/D = 0.1$, $pl/D = 1.5$).

Fig. 5.3.8, depicts the variation of normalized friction factor with Reynolds number for the helically corrugated tube (HCT-3) with (Hl/D) = 0.05, (pl/D) = 1.0. From this Fig. 5.3.8, the highest normalized friction factor, 6.9 has achieved by the twisted tape insert (y/w) = 3.5, (θ) = 0°; (Re = 3477). Moreover, changing the tapered angle from 0° to 0.3° the normalized friction factor 5.4 has found for the same Reynolds number (Re = 3477). The normalized friction factor of 3.95 has found for the twisted tape insert (y/w) = 3.5, (θ) = 0.5°, keeping the same Reynolds number. In addition, the normalized friction factor of nearly 6.7 has found for twisted tape insert (y/w) = 5, (θ) = 0°; (Re = 3477), which is less than the twisted tape (y/w) = 3.5, (θ) = 0°. The minimum amount of normalized friction factor has found 2.9 for the twisted tape insert (y/w) = 5, (θ) = 0.5°; for the maximum Reynolds number of 20,866.

Fig. 5.3.9, presents the variation of normalized friction factor in terms of Reynolds number for the helically corrugated tube (HCT-4) with (Hl/D) = 0.1, (pl/D) = 1.0. From Fig. 5.3.9, it has seen that the highest normalized friction factor, 6.4 is obtained by the twisted tape insert (y/w) = 3.5, (θ) =

$0°$; (Re = 3477). Moreover, changing the tapered angle from $0°$ to $0.3°$ the normalized friction factor 5.4 has found for the same Reynolds number (Re = 3477). The normalized friction factor of 3.8 has found for the twisted tape insert $(y/w) = 3.5$, $(\theta) = 0.5°$, without altering the Reynolds number. Besides, he normalized friction factor of nearly 6.2 has found for twisted tape insert $(y/w) = 5$, $(\theta) = 0°$; (Re = 3477), which is less than the twisted tape $(y/w) = 3.5$, $(\theta) = 0°$. The minimum amount of normalized friction factor has found 3.0 for the twisted tape insert $(y/w) = 5$, $(\theta) = 0.5°$; while the Reynolds number is 20,866.
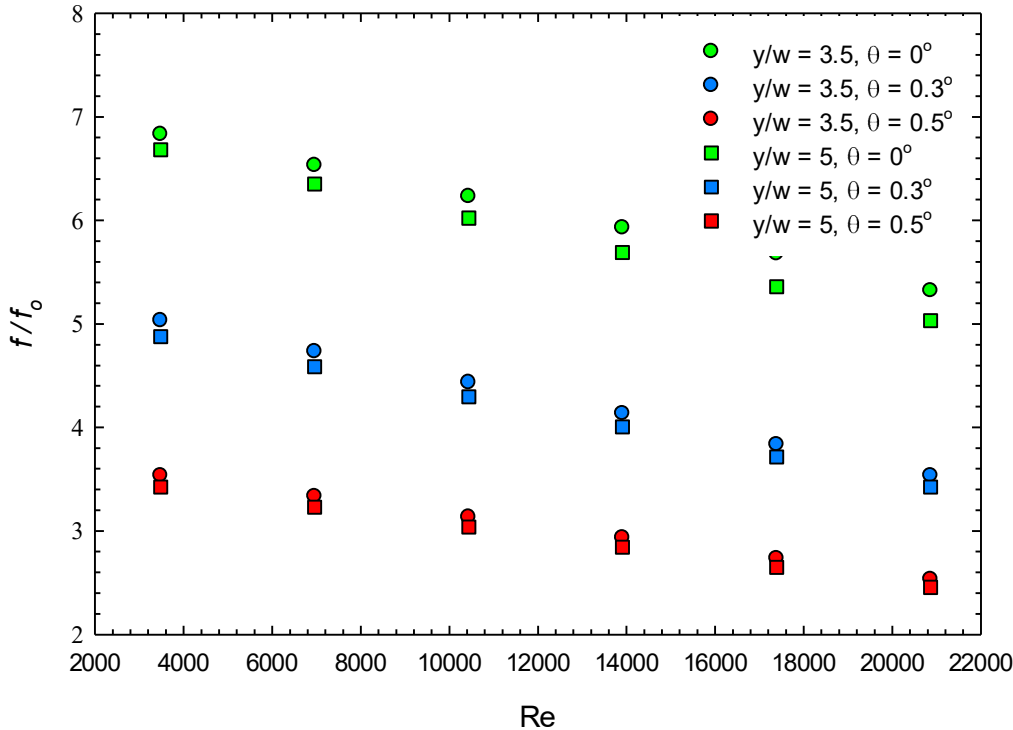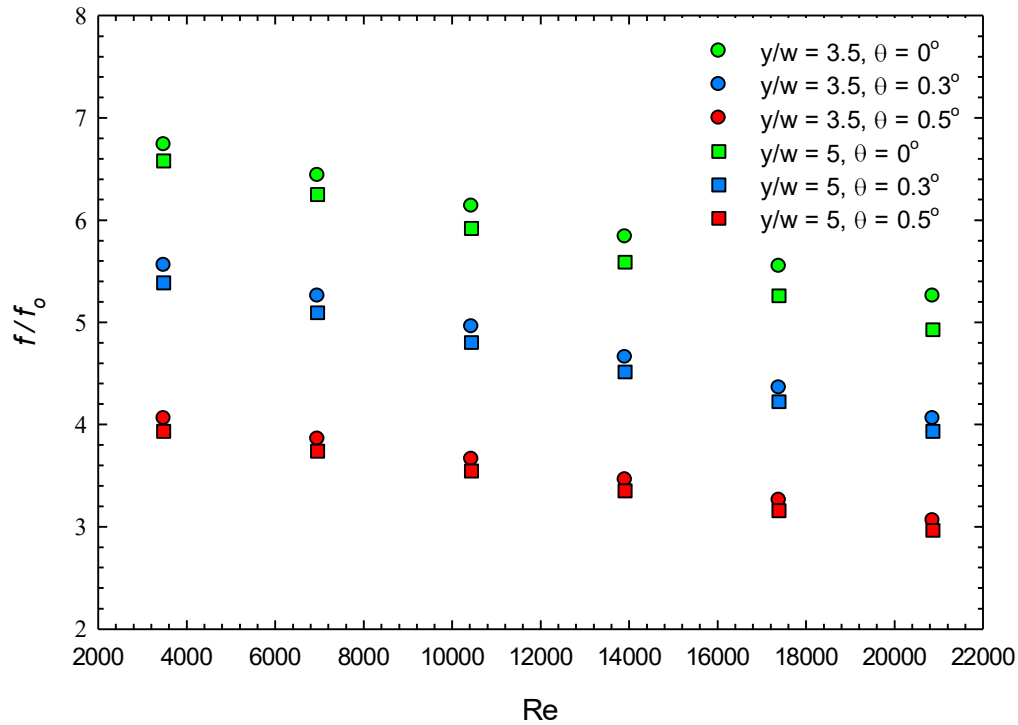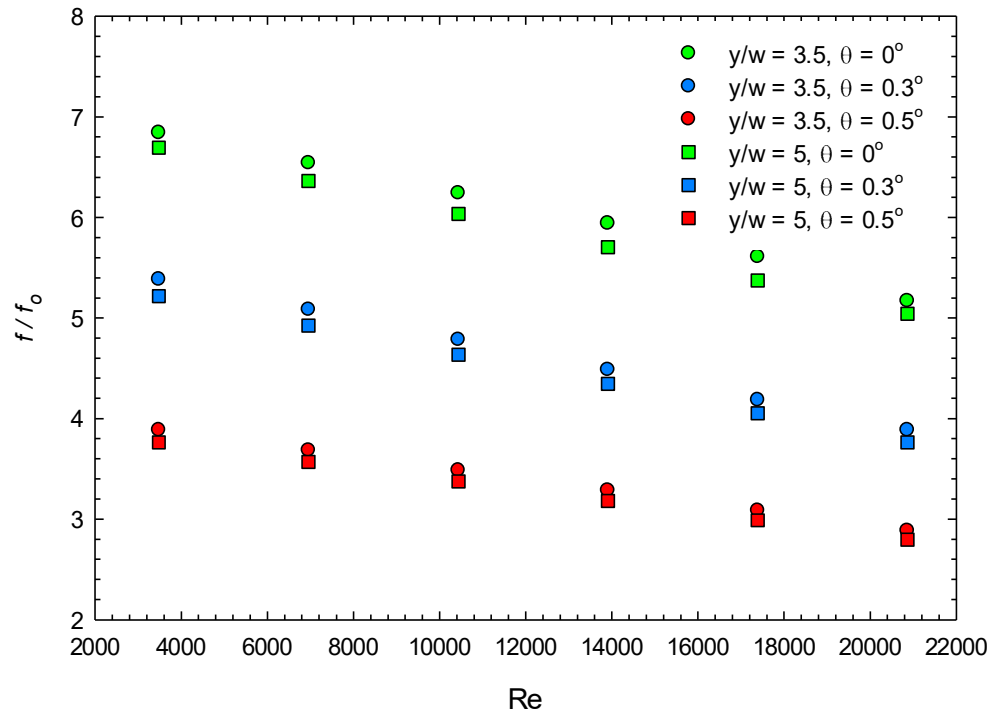
Fig. 5.3.8: Variation of normalized friction factor with Reynolds number in Helically Corrugated Tube (HCT-3), ($Hl/D = 0.05$, $pl/D = 1.0$).
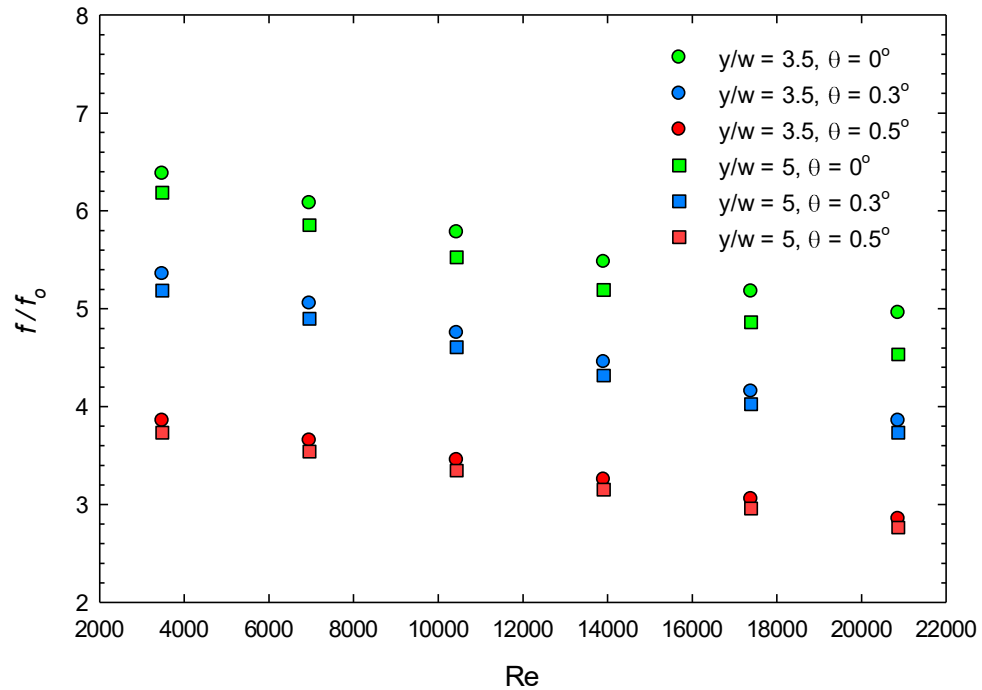

Fig. 5.3.9: Variation of normalized friction factor with Reynolds number in Helically Corrugated Tube (HCT-4), ($Hl/D = 0.1$, $pl/D = 1.0$).

5.4 Overall Performance Enhancement Characteristics

The thermal performance factor (η) is defined as the key assessment for using the twisted tape inserts, and its different twist ratios and tapered angles, and the corrugated tubes, and its different pitch-length-to-tube-diameter ratios and height-length-to-tube-diameter ratios [61,62]. Adopting twisted tapes and corrugated tubes have enhanced the heat transfer at the cost of pressure drop along the tube. This performance parameter (η) considers both the heat transfer enhancement and the pumping pressure to give its evaluation, Equation (36), which is discussed in chapter 3.

Fig. 5.5.1 illustrates the relationship between thermal performance factor and Reynolds number for different studied configurations of twisted tapes with twist ratio 3.5. In this study, twisted tapes with different tapered angles of 0°, 0.3°, and 0.5°, are introduced inside the straight circular tube and the helically corrugated tubes. From all the figures of Fig. 5.5.1 (a), (b), and (c), it is observed that the corrugated tube of ($Hl/D = 0.1$, $pl/D = 1$), exhibits maximum thermal performance factor in all these cases. Considering Fig. 5.5.1 (a), here the minimum range of thermal performance factor 0.96-0.98 has been found for the corrugated tube with ($Hl/D = 0.05$, $pl/D = 1.5$). Thermal performance below the unity indicates that the modification of the corrugated tubes and the adoption of the twisted tape inserts causes more pressure drop inside the tube than the augmentation of heat transfer. In this case, the pressure drop inside the tube is significant compared to the heat transfer enhancement for the corrugated tube with the pitch-length-to-tube-diameter ratio of 1.5, and the height-length-to-tube-diameter ratio of 0.05. The straight circular tube performs better since it has a low friction factor compared to the corrugated tube ($Hl/D = 0.05$, $pl/D = 1.5$). With the increase of Reynolds number, the thermal performance factor of all the helically corrugated tubes and the straight circular tube slightly reduces but at the maximum Reynolds number of this investigation, a higher thermal performance factor has been found. The maximum range of thermal performance factor (1.08-1.09) has been found for the helically corrugated tube of ($Hl/D = 0.1$, $pl/D = 1$). From the comparison of Fig. 5.5.1 (a) and (b), the effect of the tapered twisted tape inserts can be understood. Fig. 5.5.1 (b) shows the variation of thermal performance factor concerning Reynolds number, for the twisted tape inserts with the twist ratio of 3.5, and the tapered angle of 0.3°, for all the studied tubes. Here, the maximum range of thermal performance factor of 1.2-1.22 has been observed for the helically corrugated tube ($Hl/D = 0.1$, $pl/D = 1$). Insertion of slightly tapered twisted tape, compared to the twisted tape with the tapered angle of 0°, in Fig. 5.5.1 (a), the performance of the device has enhanced nearly 12%.

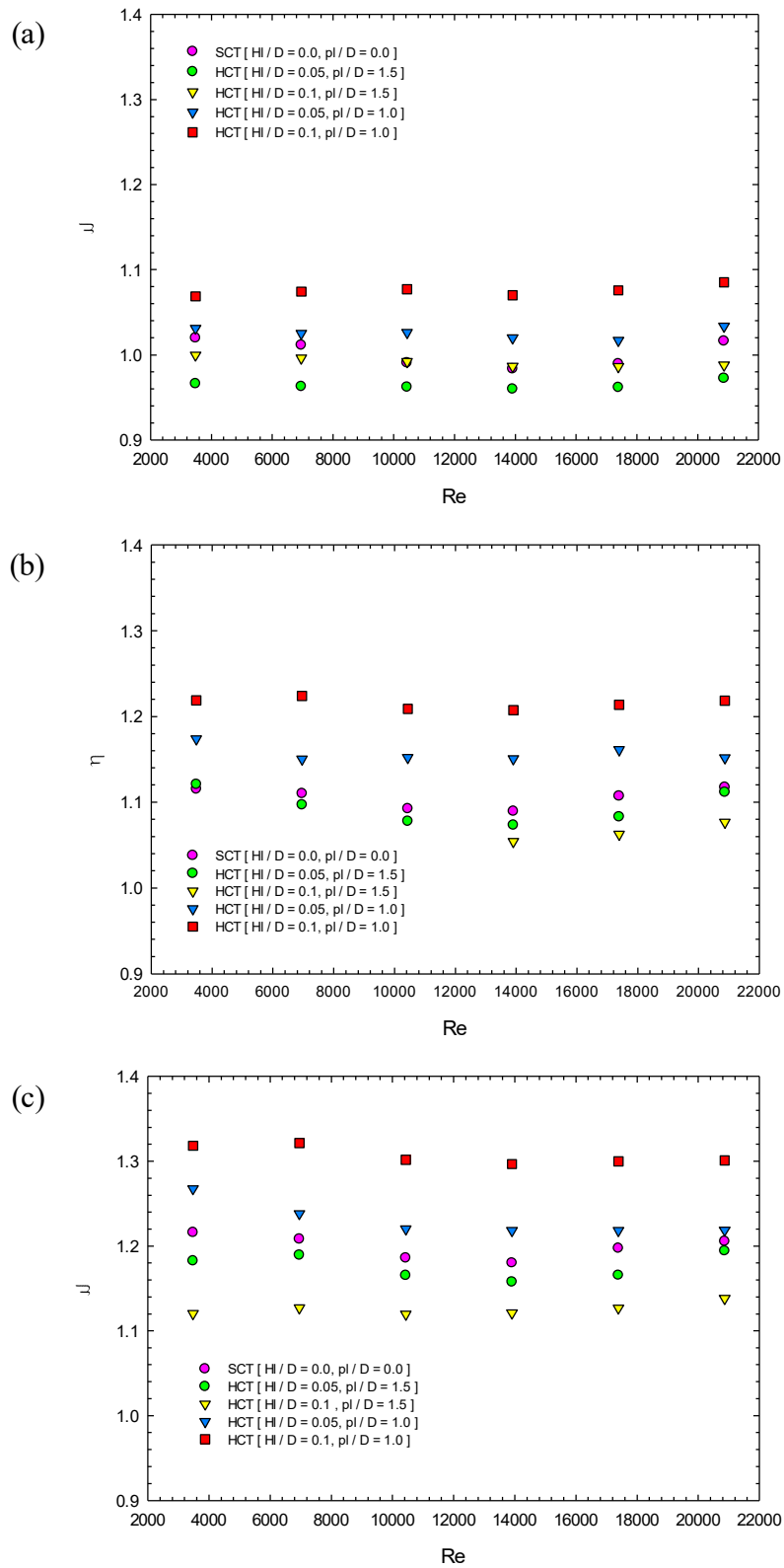Fig. 5.5.1: Variation of Thermal performance factor with Reynolds number for different twisted tape inserts; (a) Twisted tape (*y/w*) = 3.5, (*θ*) = 0°; (b) Twisted tape (*y/w*) = 3.5, (*θ*) = 0.3°; (c) Twisted tape (*y/w*) = 3.5, (*θ*) = 0.5°.

The minimum range of thermal performance factor of 1.04-1.06 has been found for the helically corrugated tube ($Hl/D = 0.1$, $pl/D = 1.5$), from Fig. 5.5.1 (b). On the other hand, the maximum range of thermal performance factor (1.08-1.09) has been found for the helically corrugated tube of ($Hl/D = 0.1$, $pl/D = 1$), from Fig. 5.5.1 (a), which is close to the minimum thermal performance providing helically corrugated tube with the tapered twisted tape of twist ratio 3.5, and the tapered angle of 0.3°. The variation of thermal performance factor concerning Reynolds number, for the twisted tape inserts with the twist ratio of 3.5, and the tapered angle of 0.5°, for all the studied helically corrugated tubes and the straight circular tube, are depicted in Fig. 5.5.1 (c). The minimum range of thermal performance factor of 1.12-1.14 is found for the helically corrugated tube of ($Hl/D = 0.1$, $pl/D = 1.5$). In all these studied tubes, a similar trend is observed that with an increase of Reynolds number the thermal performance of the tubes has decreased slightly. The maximum range of thermal performance factor of 1.32-1.325 has been observed for the helically corrugated tube of ($Hl/D = 0.1$, $pl/D = 1.0$), which is nearly 21.56% higher than the twisted tape inserts with the twist ratio of 3.5, and the tapered angle of 0°, with the helically corrugated tube of ($Hl/D = 0.1$, $pl/D = 1.0$), and close to 8.6% higher than the twisted tape inserts with the twist ratio of 3.5, and the tapered angle of 0.3°, with the helically corrugated tube of ($Hl/D = 0.1$, $pl/D = 1.0$).

Fig. 5.5.2 shows the variation of thermal performance factor with Reynolds number for different studied configurations of twisted tapes with twist ratio 5. In this study, twisted tapes with different tapered angles of 0°, 0.3°, and 0.5°, are introduced inside the straight circular tube and the helically corrugated tubes. From all the figures of Fig. 5.5.2 (a), (b), and (c), it is observed that the corrugated tube of ($Hl/D = 0.1$, $pl/D = 1$), exhibits maximum thermal performance factor in all these cases. Considering Fig. 5.5.2(a), here the minimum range of thermal performance factor 0.92-0.94 has been found for the corrugated tube with ($Hl/D = 0.05$, $pl/D = 1.5$). Thermal performance below the unity indicates that the modification of the corrugated tubes and the adoption of the heat transfer enhancement techniques causes more pressure drop inside the tube than the augmentation of heat transfer. In this case, the pressure drop inside the tube is significant compared to the heat transfer enhancement for the corrugated tube with a pitch to diameter ratio of 1.5, and a height-to-diameter ratio of 0.05. The straight circular tube performs better since it has a low friction factor compared to the corrugated tube ($Hl/D = 0.05$, $pl/D = 1.5$). With the increase of Reynolds number, the thermal performance factor of all the helically corrugated tube and the
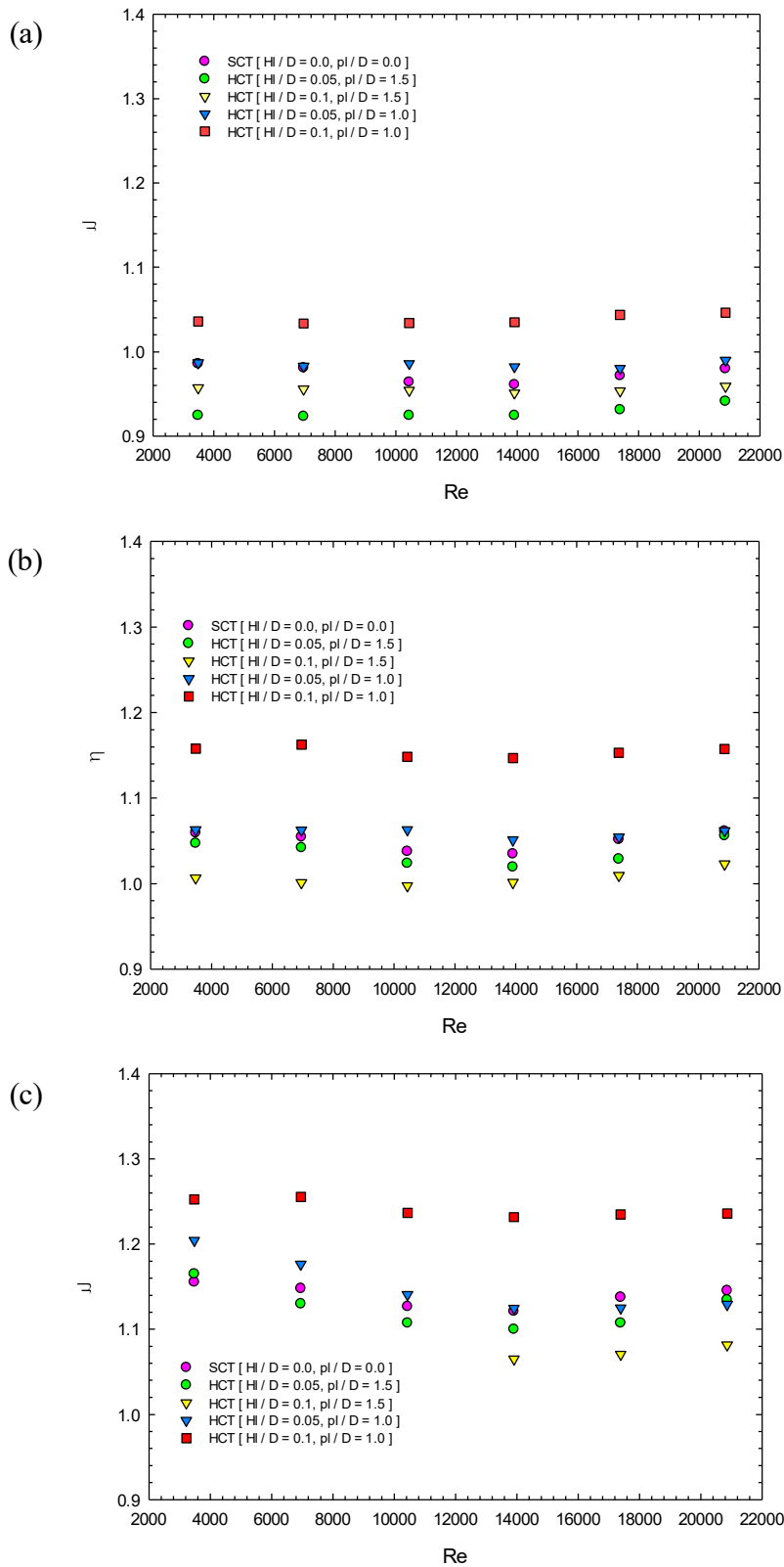
Fig. 5.5.2: Variation of Thermal performance factor with Reynolds number for different twisted tape inserts; (a) Twisted tape (*y/w*) = 5, (*θ*) = 0°; (b) Twisted tape (*y/w*) = 5, (*θ*) = 0.3°; (c) Twisted tape (*y/w*) = 5, (*θ*) = 0.5°.

straight circular tube slightly reduces but at the maximum Reynolds number of this investigation, a higher thermal performance factor has been found. The maximum range of thermal performance factor (1.04-1.05) has been found for the helically corrugated tube of ($Hl/D = 0.1$, $pl/D = 1$). From the comparison of Fig. 5.5.2 (a) and (b), the effect of the tapered twisted tape inserts can be understood. Fig. 5.5.2 (b) shows the variation of thermal performance factor concerning Reynolds number, for the twisted tape inserts with the twist ratio of 5, and the tapered angle of 0.3°, for all the studied helically corrugated tubes and the straight circular tube. Here, the maximum range of thermal performance factor of 1.16-1.17 has been observed for the helically corrugated tube ($Hl/D = 0.1$, $pl/D = 1$). Insertion of slightly tapered twisted tape, compared to the twisted tape with the tapered angle of 0°, in Fig. 5.5.2 (a), the performance of the device has enhanced nearly 11.5%. The minimum range of thermal performance factor of 1.00-1.02 has been found for the helically corrugated tube ($Hl/D = 0.1$, $pl/D = 1.5$), from Fig. 5.5.2 (b). On the other hand, the maximum range of thermal performance factor (1.04-1.05) has been found for the helically corrugated tube of ($Hl/D = 0.1$, $pl/D = 1$), from Fig. 5.5.2 (a), which is close to the minimum thermal performance providing helically corrugated tube with the tapered twisted tape of twist ratio 5, and the tapered angle of 0.3°. The variation of thermal performance factor to Reynolds number, for the twisted tape inserts with the twist ratio of 5, and the tapered angle of 0.5°, for all the studied helically corrugated tubes and the straight circular tube, are depicted in Fig. 5.5.2 (c). The minimum range of thermal performance factor of 1.08-1.09 is found for the helically corrugated tube of ($Hl/D = 0.1$, $pl/D = 1.5$). In all these studied tubes, a similar trend is observed that with the increase of Reynolds number the thermal performance of the tubes has decreased slightly. The maximum range of thermal performance factor of 1.25-1.27 has been observed for the helically corrugated tube of ($Hl/D = 0.1$, $pl/D = 1.0$), which is nearly 21% higher than the twisted tape inserts with the twist ratio of 5, and the tapered angle of 0°, with the helically corrugated tube of ($Hl/D = 0.1$, $pl/D = 1.0$), and close to 8.55% higher than the twisted tape inserts with the twist ratio of 5, and the tapered angle of 0.3°, with the helically corrugated tube of ($Hl/D = 0.1$, $pl/D = 1.0$).

Analyzing all the figures from Fig. 5.5.1 and Fig. 5.5.2, it is observed that insertion of tapered twisted tapes with the tapered angle of 0.5°, has enhanced the overall performance in terms of thermal performance factor by ~21%, and ~9%, compared to the twisted tapes with the tapered angle of 0°, and 0.3°, respectively, according to the twist ratios of 3.5 and 5, respectively. However, the twist ratio has a significant effect on the augmentation of the thermal performance factor. The

twisted tapes with the twist ratio of 3.5, have induced ~5.25% ($\theta = 0°$), ~5.3% ($\theta = 0.3°$), and ~5.35% ($\theta = 0.5°$), higher thermal performance factor than the twisted tapes with the twist ratio of 5. From these figures, it is evident that the helically corrugated tube with the height-to-diameter ratio of 0.1 and the pitch-length-to-diameter ratio of 1.0, exhibits the highest thermal performance factor, compared to all other tubes.

Fig. 5.5.3 depicts the variation of thermal performance factor with Reynolds number in the straight circular tube (SCT). It has been seen from Fig. 5.5.3 that the thermal performance factor slightly reduces with the increase of Reynolds number, but it increases with the increase of Reynolds number. All the investigated twisted tape inserts varying twist ratio and tapered angle, exhibit a similar trend for the relation of thermal performance factor with the Reynolds number. It has been observed from the figure that the highest thermal performance factor 1.22 has been achieved for the twisted tape insert with (y/w) = 3.5 and (θ) = 0.5°. The second highest thermal performance factor 1.18 is achieved by the twisted tape insert with (y/w) = 5 and (θ) = 0.5°. In these two cases, the tapered angle (θ) is the same but the twist ratio (y/w) is different. Moreover, the twisted tapes with a lower twist ratio achieved a higher thermal performance factor over the twisted tapes with a higher twist ratio, corresponding to respective tapered angles. The lowest thermal performance factor 0.9 is achieved by the twisted tape inserts with (y/w) = 5 and (θ) = 0°. Observing all these
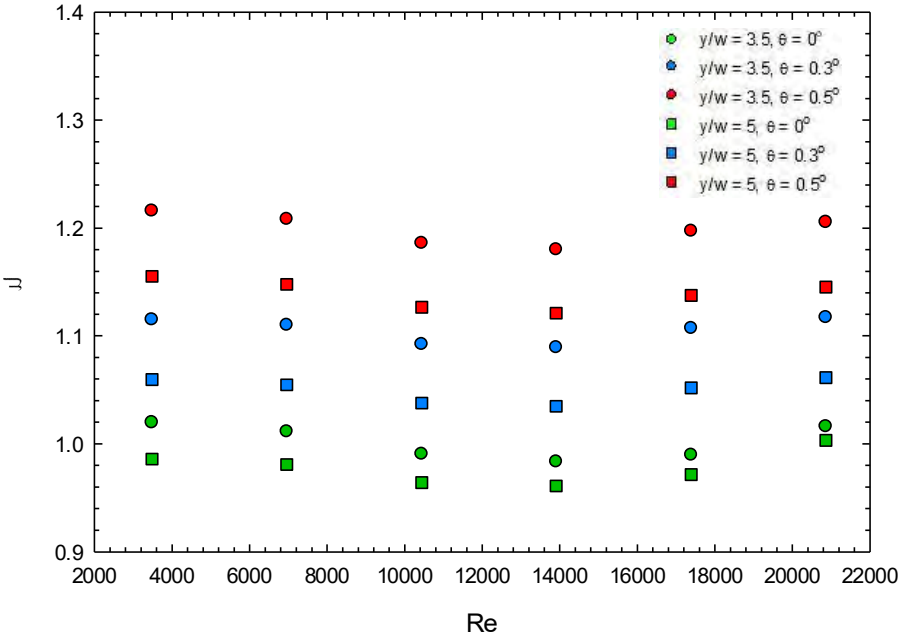

Fig. 5.5.3: Variation of Thermal Performance Factor with Reynolds number in Straight Circular Tube, (SCT): (Hl/D) = 0.0, (pl/D) = 0.0.

cases in a straight circular tube can be stated that with the increase of tapered angle of the twisted tape insert, the thermal performance factor increases. From the previous discussion, it has been found that the twisted tape with a lower twist ratio and tapered angle exhibited higher heat transfer enhancement. However, the cost of a higher normalized friction factor has dropped their overall thermal performance. On the contrary, the twisted tape with higher tapered angles does not perform well in heat transfer enhancement but the gain in pumping pressure boosted the performance of the gradually tapered twisted tapes with higher tapered angles.

The variation of the thermal performance factor with Reynolds number is illustrated in Fig. 5.5.4. It has been observed from this figure that the thermal performance factor reduces gradually with the increase of turbulence in fluid, flowing through the helically corrugated tube (HCT-1) (Hl/D = 0.05, pl/D = 1.5). However, there are very small differences among the thermal performance factors, investigated for different Reynolds numbers. The insertion of twisted tape inserts into the corrugated tube induces a thermal performance factor for that tube. Twisted tapes with different twist ratios and tapered angles have a different impact on thermal performance factors individually. The maximum thermal performance of 1.23 has been found for the twisted tape with (y/w) = 3.5, and (θ) = 0.5°. Later the closest thermal performance factor 1.18 has achieved for the twisted tape with (y/w) = 5, and (θ) = 0.5°. Here, the variation between highest thermal performance providing twisted tapes, in the twist ratio whilst the tapered angle remained same. It is seen from this figure that the lower twist ratio provides a higher thermal performance factor. Moreover, the tapered angle of twisted tapes has a significant effect in enhancing the thermal performance factor. It is observed that the higher tapered angle shifted upward the thermal performance line in the figure compared to the lower tapered angle. The higher thermal performance factors are found for the twisted tape with the tapered angle of 0.5° and the lower thermal performance factors are found for the twisted tape with the tapered angle of 0°. The minimum thermal performance factor of 0.97 has found for the twisted tape with (y/w) = 5, and (θ) = 0°. The thermal performance factor below the unity denotes that the required pumping power for fluid flow is significant compared to the heat transfer enhancement. Therefore, the heat exchanger would perform poorly in this configuration.

Fig. 5.5.4: Variation of Thermal Performance Factor with Reynolds number in Helically Corrugated Tube, (HCT-1): (Hl/D = 0.05, pl/D = 1.5).

Fig. 5.5.5: Variation of Thermal Performance Factor with Reynolds number in Helically Corrugated Tube, (HCT-2): (Hl/D = 0.1, pl/D = 1.5).

Figure 5.5.5, shows the variation of thermal performance factor with Reynolds number for helically corrugated tube (HCT-2) ($Hl/D = 0.1$, $pl/D = 1.5$). The maximum thermal performance of 1.15 has been found for the twisted tape with (y/w) = 3.5, and (θ) = 0.5°. Later the closest thermal performance factor 1.08 has been achieved for the twisted tape with (y/w) = 5, and (θ) = 0.5°. The lowest thermal performance factor 0.95 has been found for the twisted tape with (y/w) = 5, and (θ) = 0°.

Figure 5.5.6, shows the variation of thermal performance factor with Reynolds number for helically corrugated tube (HCT-3) ($Hl/D = 0.05$, $pl/D = 1.0$). The maximum thermal performance of 1.28 has found for the twisted tape with (y/w) = 3.5, and (θ) = 0.5°. Then, the closest thermal performance factor 1.2 has been achieved for the twisted tape with (y/w) = 5, and (θ) = 0.5°. The minimum thermal performance factor of 1.02 has found for the twisted tape with (y/w) = 5, and (θ) = 0°.

Figure 5.5.7, shows the variation of thermal performance factor with Reynolds number for helically corrugated tube (HCT-4) ($Hl/D = 0.1$, $pl/D = 1.0$). The minimum thermal performance factor of 1.08 has been found for the twisted tape with (y/w) = 5, and (θ) = 0°. On the contrary, the maximum thermal performance of 1.32 has been found for the twisted tape with (y/w) = 3.5, and (θ) = 0.5°. Later the closest thermal performance factor 1.26 has been achieved for the twisted tape with (y/w) = 5, and (θ) = 0.5°.
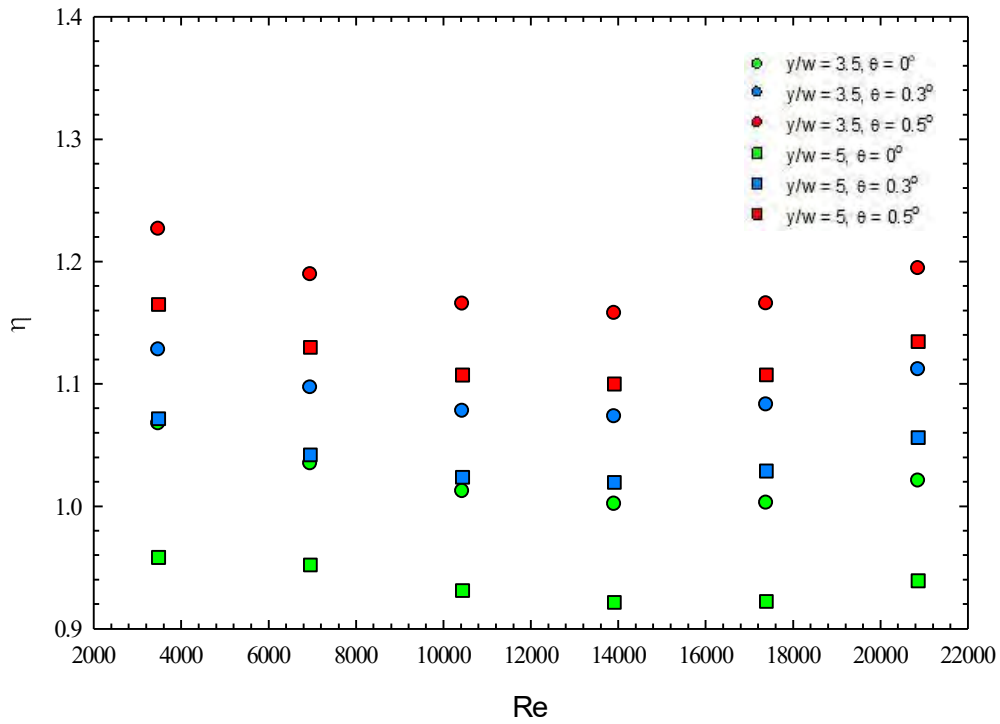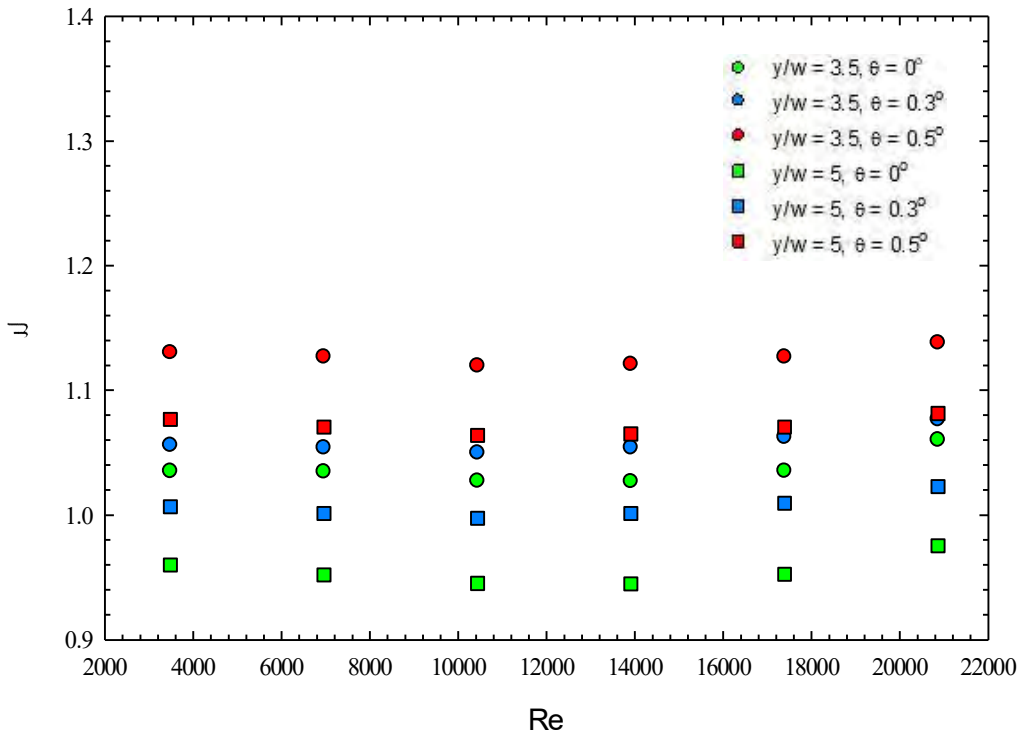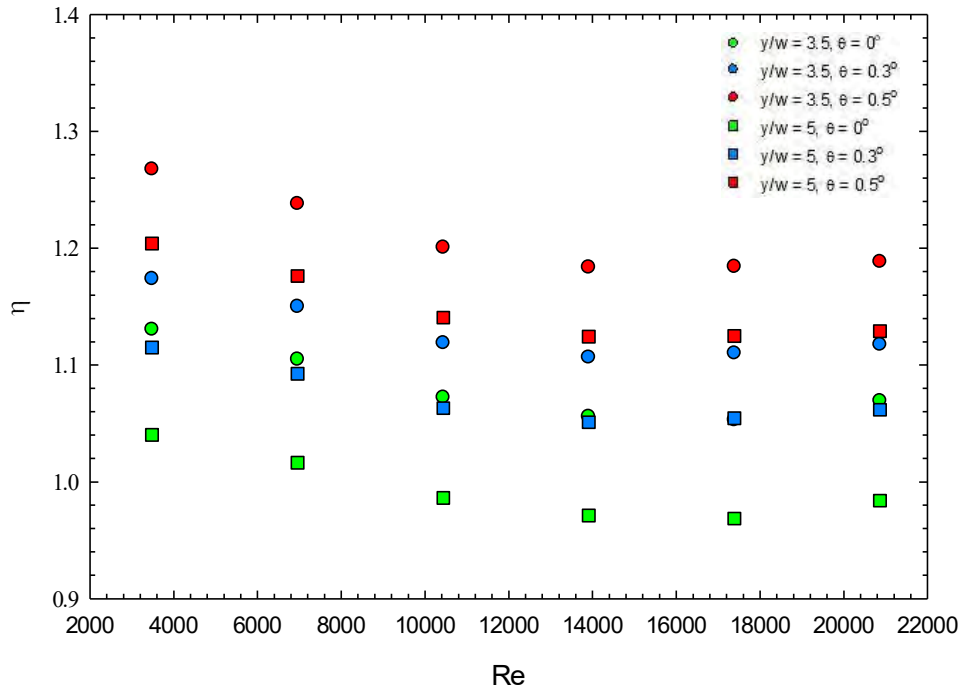
Fig. 5.5.6: Variation of Thermal Performance Factor with Reynolds number in Helically Corrugated Tube, (HCT-3): ($Hl/D = 0.05$, $pl/D = 1.0$).
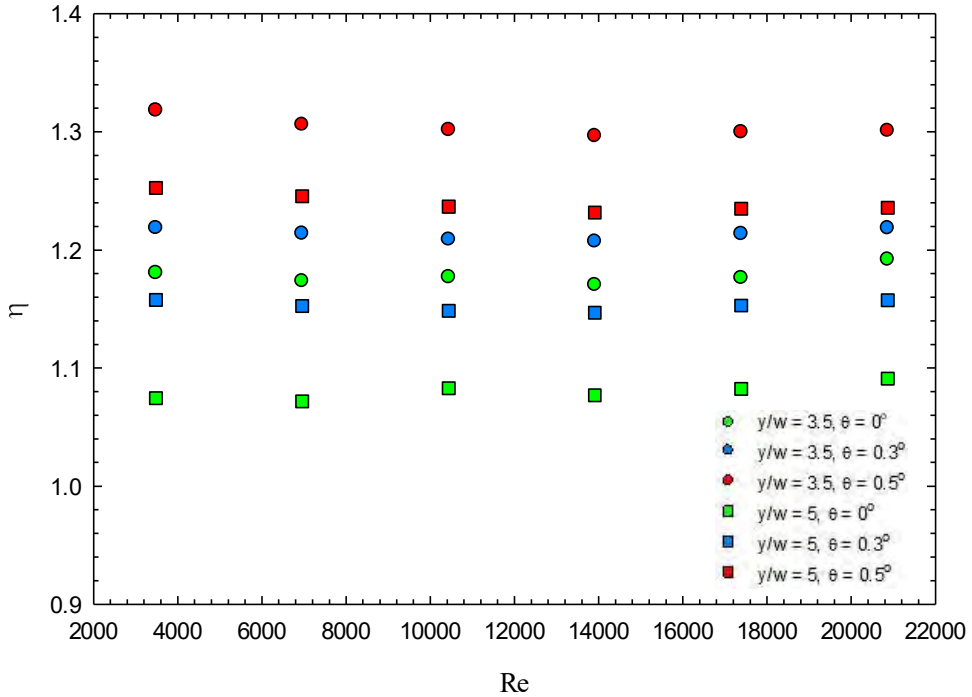

Fig. 5.5.7: Variation of Thermal Performance Factor with Reynolds number in Helically Corrugated Tube, (HCT-4): ($Hl/D = 0.1$, $pl/D = 1.0$).

CHAPTER 6

Predictive Modeling Using Artificial Neural Network

In the present study, simulated data from a total of 180 investigated cases have been presented. Furthermore, to get a better insight into the effect of different geometric parameters of the twisted tape and corrugated tube on the investigated performance parameters, the computational intelligence technique has been applied in the present investigation.

6.1 Introduction

The Computational Intelligence (CI) techniques, such as Artificial Neural Networks (ANNs), have been successfully applied in many scientific types of research and engineering practices. ANNs have been developed for about three decades and are now widely used in various application areas such as pattern recognition, system identification, dynamic control, and so on. ANN offers a new way to simulate nonlinear, or uncertain, or unknown complex systems without requiring any explicit knowledge about input/output relationships. ANN has more attractive advantages. It can approximate any continuous or nonlinear function by using a certain network configuration. It can be used to learn complex nonlinear relationships from a set of associated input/output vectors. It can be implemented to dynamically simulate and control unknown or uncertain processes. In recent years, Artificial Neural Network (ANN) has been implemented to various heat transfer problems based on a database available from numerical simulations or experiments [66-68]. Typically, ANN, in presence of a sufficient amount of training data can reach the superhuman level of accuracy to predict complex systems and phenomena. ANN is particularly advantageous since once it is trained it can predict a complex and dynamic system with little to no computational cost. In the field of modeling enhanced heat-exchangers, researchers and engineers were more willing to reduce their either experimental or modeling data into one tangible heat transfer correlation. Unlike simple geometries, twisted tape inserts and corrugated tubes, have so many influential parameters that they could not be gathered and simplified as a correlation. This is not very easy to extract a proper correlation covering all of the data, and even the results of the correlation do not show accuracy in the range of defined conditions in terms of twist ratios (y/w) and tapered angles (θ) for the twisted tape, and pitch-to-diameter ratios (pl/D) and height-to-diameter ratios (Hl/D) for the helically outward corrugated tubes. To overcome this shortage, some

scientists highly recommended the use of computational intelligence techniques such as artificial neural networks (ANNs).

Xie et al. [68] used an Artificial Neural Network (ANN) to simulate heat transfer in shell-and-tube heat exchangers with segmental or continuous helical baffles. In their study, three heat exchangers were experimentally investigated. They only had a limited amount of experimental data to use for training and testing neural network configurations. The maximum difference between predicted and experimental results.

Sablani et *al.* [69] investigated two ANN models for a cube with constant thermophysical properties and a semi-infinite plate with temperature-dependent thermal conductivity, resulting in linear and nonlinear problems. Furthermore, they transformed the training data sets using a trigonometric function to improve the ANN model's prediction performance.

Gupta et *al.* [70] conducted training, testing, and validation of an ANN using the experimentally obtained data from a counter-flow plate-fin heat exchanger. The objective of their work was to predict the performance of the heat exchanger. After validation of the predicted data with the experimental data, they found about 80-90% accuracy. Furthermore, they examined two well-known global search techniques, simulated annealing, and the genetic algorithm.

Wang et *al.* [71] used an artificial neural network (ANN) to predict the heat transfer rates of shell-and-tube heat exchangers with segmental baffles or continuous helical baffles, based on limited experimental data. Moreover, they used The Back Propagation (BP) algorithm in training the networks. Different network configurations were also studied. The deviation between the predicted results and experimental data was less than 2%. Comparison with correlation for prediction ANN had shown superiority.

Kumra et *al.* [72] carried out a study to predict the rate of heat transfer of a wire-on-tube type heat exchanger by utilizing the support vector machine model. They developed an algorithm in MATLAB to formulate an equation for the total heat transfer which gave a minimal error when compared to traditional techniques. Their model exhibited inherent advantages due to its use of the structural risk minimization principle in formulating cost functions and of quadratic programming during model optimization.

Thubalut and Grandjean [73] conducted a study to introduce computing with neural networks. To evaluate the potential of neural networks for correlating heat transfer data, three different examples were solved, using a three-layer feedforward neural network in their research. They concluded that neural networks could be used to adequately correlate heat transfer data.

Verma et *al.* [74] investigated the heat transfer performance of the proposed fabricated heat exchanger using corrugated and non-corrugated pipes. Pitch and depths were varied in the case of corrugated pipe in their study. In addition, they modeled an artificial neural network (ANN) for predicting heat transfer coefficient, Nusselt number, and Reynolds number.

Devi et *al.* [75] were experimentally conducted an investigation to predict the Nusselt number of a counter flow concentric heat exchanger with Plain Swirl Tapes of different swirl ratios y = 2.0, y = 4.4, and y = 6.0. Their study concentrated on the MLP-ANN with 3-layer feed-forward neural network is adopted to obtain Nusselt number (Nu) based on the three inputs such as Prandtl number (Pr), twist ratios (y), and Reynolds number (Re) as input variables for heat exchanger.

Aasi and Mishra [76] experimentally investigated a compact cross-flow three-fluid heat exchanger with plain rectangular fins for both thermal and hydraulic efficacy under steady-state conditions. In addition, the investigation was assisted with the ANN modeling for the prediction of the thermo-hydraulic efficacy with two inputs (Reynolds number and flow arrangement type) and four output performance parameters (Colburn factor, friction factor, and effectiveness ratios). In their study, a fraction of 77% and 23% of data was considered for training and testing the neural network respectively.

Liu et *al.* [77] conducted an experimental study on pulsed spray cooling heat transfer on a vertical surface under controlled nozzle pressure. They developed an ANN model for pulsed spray cooling heat transfer on a vertical surface and compared the results with the empirical correlations. The ANN model had shown much higher accuracy in predicting the pulsed spray cooling heat transfer.

Islam et *al.* [78] implemented an approach based on a multi-fidelity physics-informed neural network (MPINN) to achieve long-range MD simulation results over a large sample space with significantly less computational cost. The fidelity of their multi-fidelity study was based on the integration timestep size of MD simulations. Besides, they performed two benchmark studies, involving one and two-component Lennard-Jones systems, to determine the optimum percentage of high-fidelity training data required to achieve accurate results with high computational saving.

In the interest of investigating the combined effects of the twisted tape, and the corrugated tubes, on the enhanced heat transfer with pressure drop characteristics and finally the thermal performance factor, the present study aims to get better insight into using twisted tape inserts with twist ratios (y/w = 3.5 and 5) and tapered angles (θ = 0°, 0.3°, and 0.5°) inside the helically outward corrugated tubes with pitch-length-to-tube-diameter ratios (pl/D = 1 and 1.5) and height-length-to-tube-diameter ratios (Hl/D = 0.05 and 0.1). Since the present work has dealt with a complex heat transfer phenomenon inside the tubes, inspired by the biological network of neurons in the brain, ANN can be applied to provide accurate prediction (both qualitative and quantitative) of the combined effects of different geometric parameters.

6.2 Principles of Artificial Neural Network

In the early age of machine learning, Warren McCullock and Walter Pitts tried to understand the working mechanism of the biological brain to design artificial intelligence. In 1943, they published the first concept of a simplified brain cell called the *McCullock-Pitts* (*MCP*) *neuron* [79].

6.2.1 Biological Neuron

A human brain has billions of neurons. Neurons are interconnected nerve cells in the human brain that are involved in the processing and transmitting of chemical and electrical signals. A real neuron is composed of a cell body, dendrites, and a tubular axon, which terminates with end buttons called synapses, shown in Fig. 6.2.1. A neuron's dendritic tree is connected to a thousand neighboring neurons. When one of those neurons fire, a positive or negative charge is received by one of the dendrites. The strengths of all the received charges are added together through the processes of spatial and temporal summation. Signals transmit via electrochemical signals. The synapses release a chemical transmitter the sum of which can cause a threshold to be reached causing the neuron to "fire".
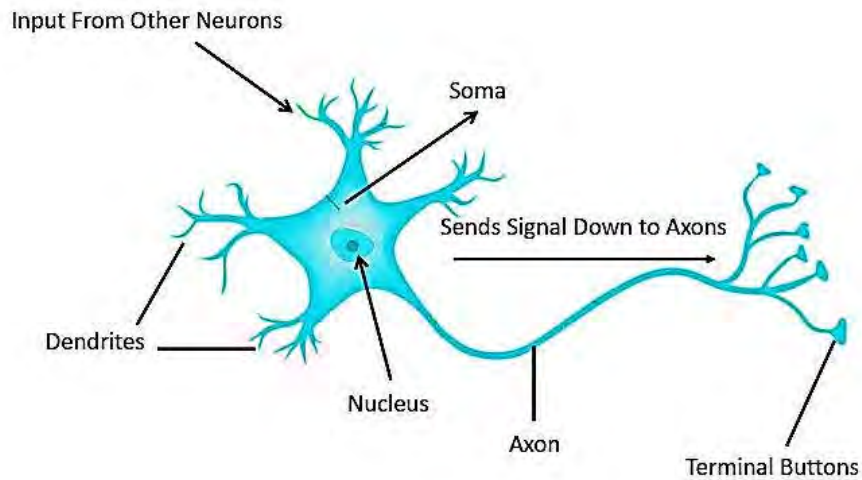
Fig. 6.2.1: A biological neuron.

6.2.2 Artificial Neuron

An artificial neuron is a mathematical function based on a model of biological neurons, where each neuron takes inputs, weighs them separately, sums them up, and passes this sum through a nonlinear function to produce output, shown in Fig. 6.2.2. Every neuron holds an internal state called activation signal and each connection link carries information about the input signal. Every neuron is connected to another neuron via a connection link.

Fig. 6.2.2: An artificial neuron.

6.2.3 Perceptron

Perceptron was introduced by Frank Rosenblatt in 1957. He proposed a Perceptron learning rule based on the original *MCP neuron* [80]. A Perceptron is an algorithm for supervised learning of binary classifiers. This algorithm enables neurons to learn and process elements in the training set one at a time, shown in Fig. 6.2.3.
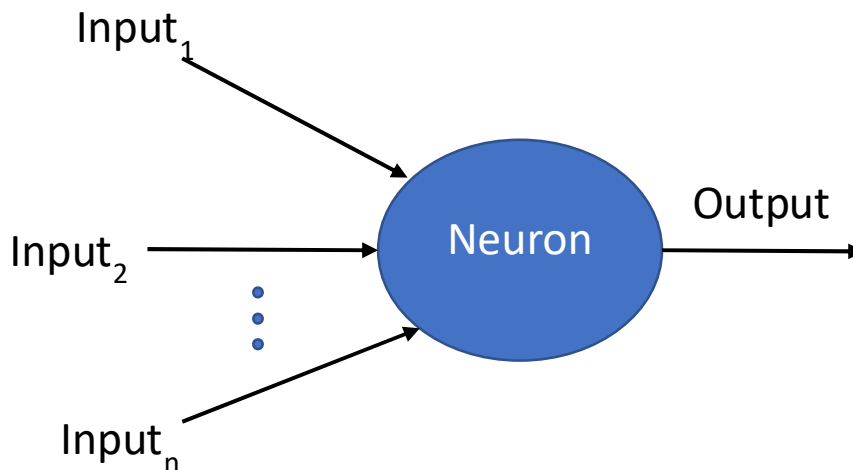

$$y = f\left(\sum_{i=1}^{n} x_i * w_i + b\right)$$
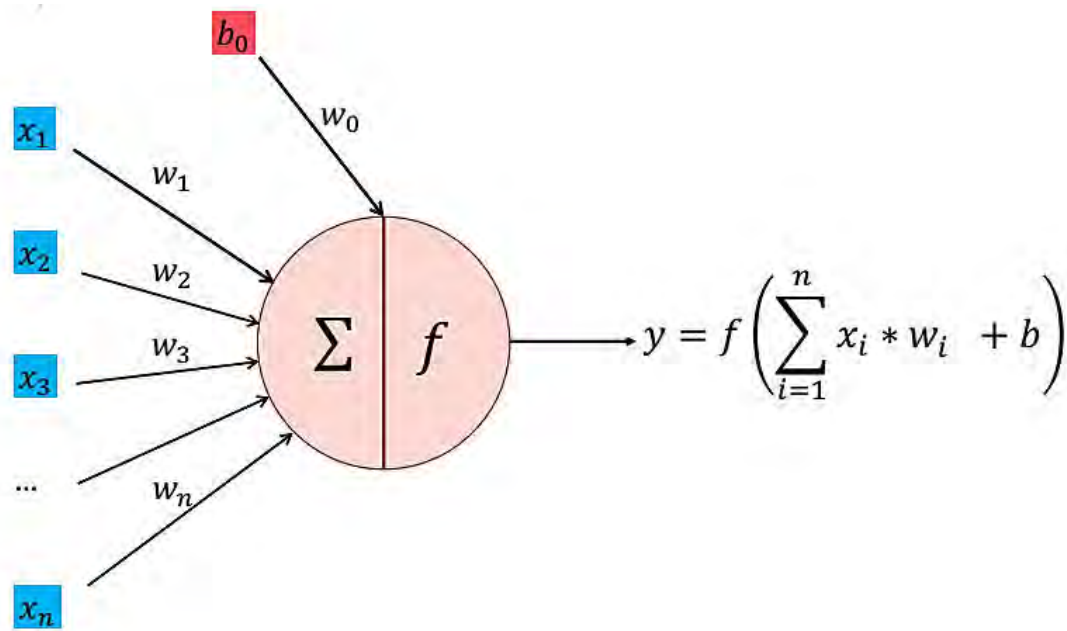
Fig. 6.2.3: A basic model of Perceptron

There are two types of perceptron: Single layer and Multilayer.

1. Single-layer - Single layer perceptron can learn only linearly separable patterns
2. Multilayer - Multilayer perceptron or feedforward neural networks with two or more layers have the greater processing power

The Perceptron algorithm learns the weights for the input signals to draw a linear decision boundary.

6.2.4 Activation Functions

Activation functions are decision-making units of neural networks. Different activation functions are discussed as follows:

6.2.4.1 Step Function

An arbitrary step function is shown in figure Fig. 6.2.4.1. This function outputs a value *a* if *net* is less than a threshold value *c* and a value *b* if net is greater than the threshold value:

$$F(net) = \begin{cases} a & if \quad net < c \\ b & if \quad net > c \end{cases} \tag{39}$$

The output at *net* = *c* is sometimes *a*, sometimes *b*, or the average of the two. The step function is suitable for binary applications. For example, digital processes need inputs and outputs that can be represented with only two numbers, 0 and 1.
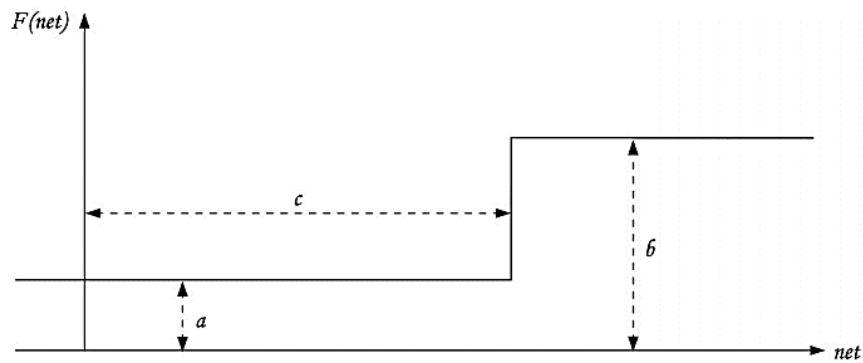
Fig. 6.2.4.1: An arbitrary step function.

A potential disadvantage of step function is that it is discontinuous, making it sensitive to noise. Moreover, non-differentiability of this function constrains the number of learning algorithms that can be applied to the network.

6.2.4.2 Ramp Function

The ramp function is an evolution of the step function that overcomes the discontinuity problem by introducing a linear "ramp" between the high and low output values. The ramp function is illustrated in Fig. 6.2.4.2 and is defined by the following set of equations:

$$F(net) = \begin{cases} a & if \ net < c \\ b & if \ net > d \\ a + \frac{(net-c)(b-a)}{c-d} & otherwise \end{cases} \tag{40}$$

Fig. 6.2.4.2: An arbitrary Ramp function.

By continuity, the ramp function has no binary attribute, but still saturates at a high and low output value. Even though the ramp function is continuous, it is non-differentiable at *net* = *c* and *net* = *d*. The ramp function is an example of a simple piecewise linear function. More elaborate functions can be created by combining even more linear functions.
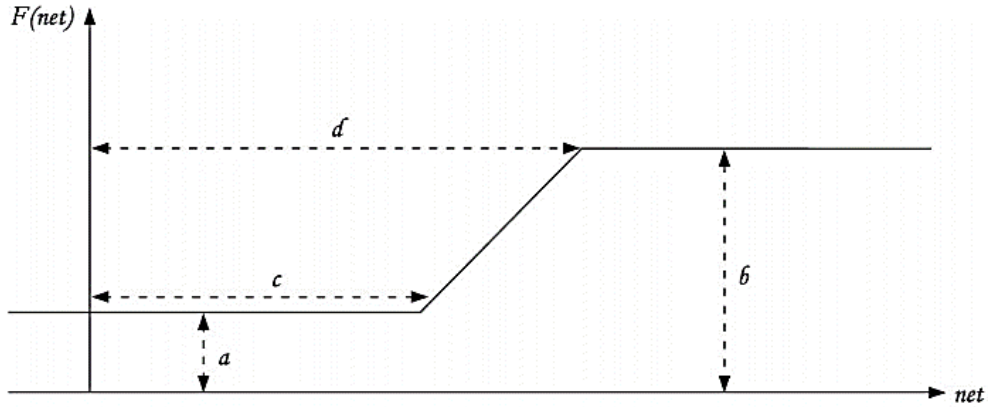
6.2.4.3 Sigmoid Function

Sigmoid functions are S-shaped functions that are smooth (continuous and differentiable), symmetric about a point, and asymptotically approach a low and high value. Because of these characteristics, effective learning algorithms are easier to apply and, as a result, sigmoid functions are the most common functions in neural network applications. In addition, experimental observation suggests that the firing rate of a biological neuron is approximately a sigmoidal function of the net input [81]. Fig. 6.2.4.3 shows an arbitrary sigmoid function. The limits of this function are as follows:

$$\lim_{net \to \infty} F(net) = b$$

$$\lim_{net \to -\infty} F(net) = a$$

Common choices are *a* = -1 or *a* = 0, *b* = 1, and *c* = 0. Two examples of sigmoid functions are:

$$F(net) = \frac{1}{1 + \exp(-net)}$$ (Logistic sigmoid function) (41)

and, $F(net) = \tanh(net)$ (Hyperbolic Tangent function) (42)
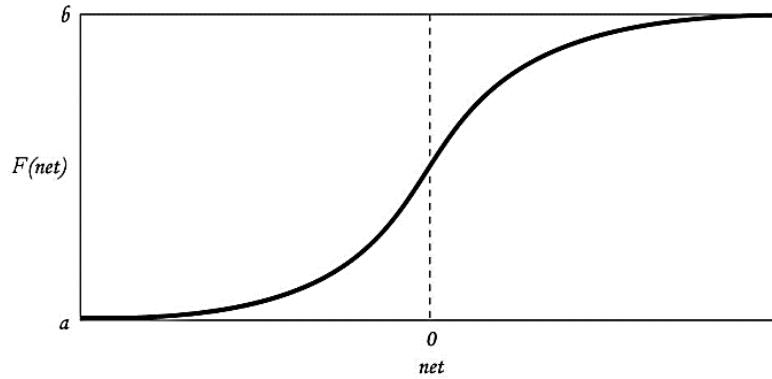
Fig. 6.2.4.3: An arbitrary Sigmoid function.

These two example functions can be scaled, translated, and rotated according to the application without losing the characteristics of a sigmoid function.

6.2.4.4 Gaussian Function

Bell-shaped curves such as the one illustrated in Fig. 6.2.4.4 are known as Gaussian or radial-basis functions. Gaussian functions are also continuous, differentiable, and have asymptotes but they are not monotonic. Gaussian functions are used in radial-basis function networks. Algebraically, a Gaussian function may be described with the following expression:

$$F(net) = \frac{1}{\sqrt{2\pi}\sigma} \exp\left[-\frac{1}{2}\left(\frac{net-\mu}{\sigma}\right)^2\right] \tag{43}$$

where μ and σ are the mean and standard deviation, respectively.

Fig. 6.2.4.4: An arbitrary Gaussian Function

6.3 Neural Network Architecture

ANNs are made up of at least two physical components, one of which is the processing elements, while the other is the connection between the processing elements. Generally, the processing elements are neurons and the connections are links. The neurons are also known as nodes, and an ANN consists of a series of layers with several nodes. Besides, Nodes are gathered together into a layer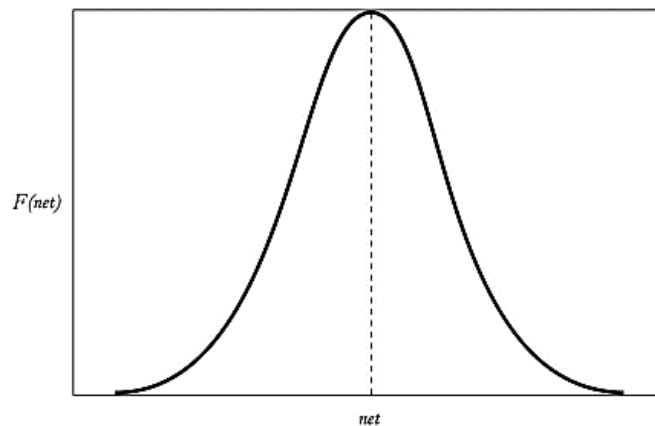. Each link has a specific weight coefficient associated with it. For each node, there exists an activation function and a bias associated with it. Every node receives information from its neighboring nodes and after manipulating the information delivers it to the other nodes connected to it. Those neurons which receive data from outside of the network are the input layer and those which produce final data are the output layer. The others are categorized as hidden layers. There exist different ways of connecting the neurons, and information can be processed by several methods. The structure of neural networks is shaped depending upon the method of processing and how they are linked. Of various types of ANNs methods, the feed-forward neural network is the

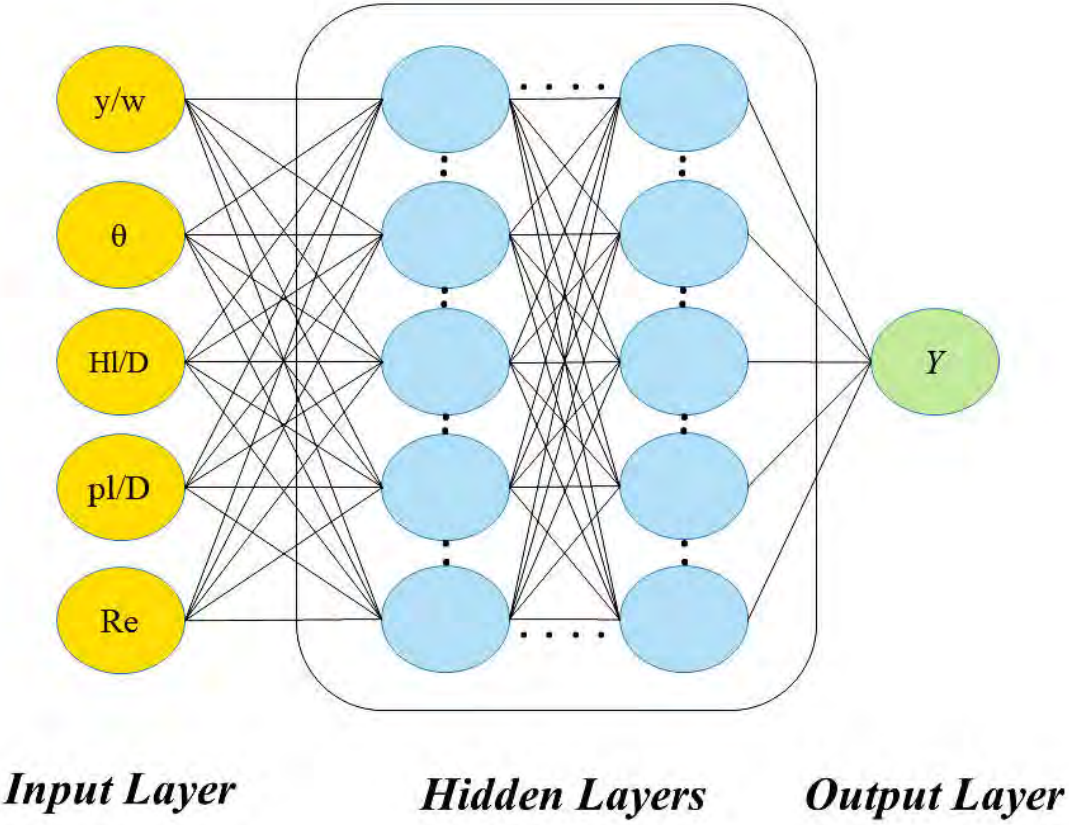**Input Layer**   **Hidden Layers**   **Output Layer**

Fig 6.3.1: Artificial neural network architecture used in the present study

favorite method for engineers working on static systems. In the feed-forward method, the information is delivered using forward transportation through the network. The main duty of a neural network is to find the best set of weight coefficients so that the output neurons could closely represent the original problem behavior. These weight coefficients are found through a process called the training step. Among algorithms used to train the network, the backpropagation training approach has a high reputation in the neural network area. During training, the offset between actual neural network outputs and desired outputs for all the training samples is computed several times for the performance of the neural network to be evaluated and then to be modified. The iteration is continued until a stopping criterion is satisfied.

In this present study, using the ANN, the performance factors of a heat exchanger are predicted for the twisted tape inserts with the range of twist ratio from 2 to 6. The tapered angles of the twisted tape are kept unchanged compared to the computational study. In the case of the design parameters of the helically corrugated tubes, the range of height-length-to-tube-diameter ratio (Hl/D) is from 0 to 0.1, and the range of pitch-length-to-tube-diameter ratio (pl/D) is from 0 to 1.5, are considered to predict the values of the performance factors.

In the proceedings, the required steps for training, testing, and taking results through ANN is described in detail:

- Selecting input and output parameters for the neurons in the input and output layer, respectively. Herein, twist ratio (y/w), tapered angle (θ), height-to-diameter ratio (Hl/D), pitch-to-diameter ratio (pl/D), and Reynolds Number (Re) have been considered as input parameters. employed for the input layer. This study has aimed to predict the Nusselt number (Nu), friction factor (f), Normalized Nusselt number (Nu/Nu_o), normalized friction factor (f/f_o) and thermal performance factor (η) using present constructed ANN. One of these parameters is used as the output parameter of the ANN.
- Dividing available data collected from the simulation into two types of training and testing data sets. 180 sets of data produced by Fluent were used as input in the network, 120 of which were allocated to the training area, and 50 sets of data for trial and validation, while 10 sets of data were employed to test the present artificial neural network. The training and testing data were arbitrarily selected.
- Normalization of the collected data was done in the range of [-1 1].

- Developing the network body by setting the number of hidden layers and the number of hidden neurons. To find the best construction, the network should be examined through trial and error. Here, the four hidden layers consist of 20 neurons in each layer [83-84], which is deep enough to train complex relationships between input and output units.

- Implementation of regularization criterion. In present work L_2 regularization has been implemented, where the regularization rate is set to $\lambda = 10^{-2}$ with a learning rate of 0.001.

- To train the ANN, the Mean-squared error function (MSE) (Equation 44) has been minimized. The equation of the loss functions is shown below:

$$J_{MSE} = \frac{1}{N} \sum_{n=1}^{N} \left[(Y_n - \bar{Y}_n)^2 \right] \tag{44}$$

  Here, Y_n is the predicted output, $\bar{Y}_n$ is the actual output obtained from numerical simulations and N is the total number of elements in the output unit.

- The loss function is minimized using the L-BFGS [63] method together with Xavier's initialization method [64]. The sigmoid function is chosen as an activation function except for the output layer, where no activation function has been included.

- Extraction of data from the trained network and validating the performance of the network against the sets of test data by using the statistical criteria.

6.4 Validation of the developed ANN model

With the aid of artificial neural network (ANN), using the obtained numerical data of the present study, a significant amount of data for Nusselt number (Nu), friction factor (f), Normalized Nusselt number (Nu/Nu_o), Normalized friction factor (f/f_o), and thermal performance factor (η), for a heat exchanger, can be generated varying a wide range of design parameters i.e., the twist ratio and the tapered angle of the twisted tapes, and the height-length-to-tube-diameter ratio and the pitch-length-to-tube-diameter ratio of the helically corrugated tubes. Here, an effort has been made to compare the obtained computational values of the Nusselt number, friction factor, normalized Nusselt number, normalized friction factor, and thermal performance factor, to the ANN predicted values of those performance parameters, which are depicted in Fig. 6.4.1 (a), Fig. 6.4.1 (b), Fig. 6.4.1 (c), Fig. 6.4.1 (d) and Fig. 6.4.1 (e), respectively. It is observed that the predicted data from the ANN, are in a 2% error band with the obtained computational data of Nusselt number and friction factor. Whilst the error band is 1% for the normalized Nusselt number, normalized friction factor, and thermal performance factor. This indicated the validation of the accuracy of the developed artificial neural network with the present analogy. A similar pattern of test accuracy has also been found by Souayeh et al. [83] is 97%, Bhattacharyya et al. [84] is more than 97%, and Nasr et al. [85] is about 98%.
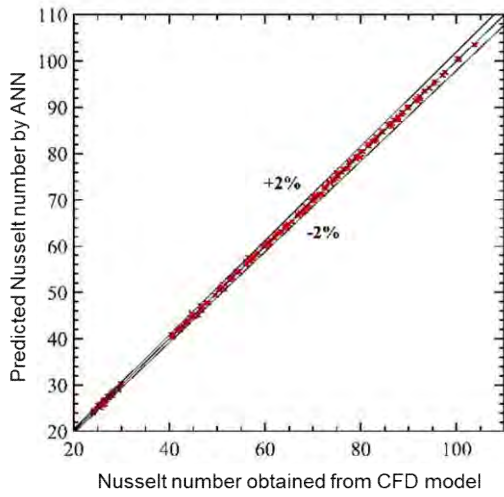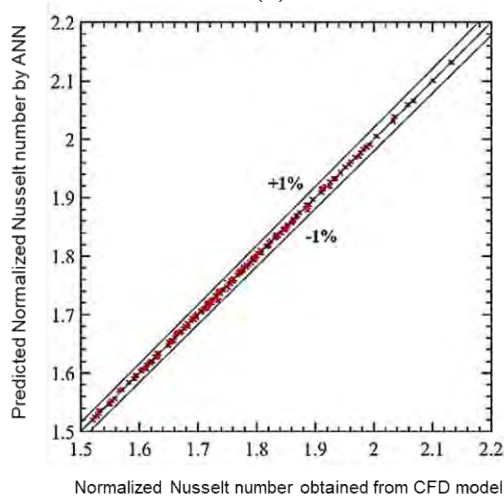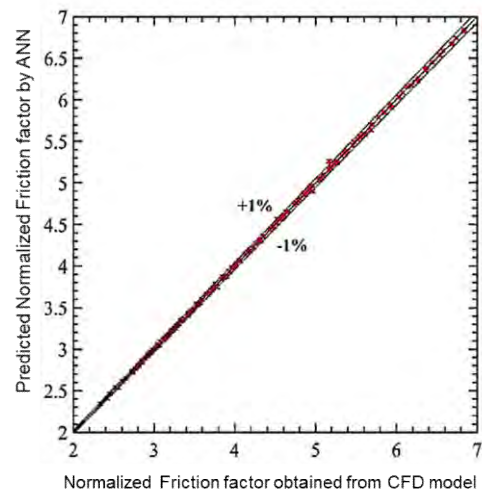
(a)
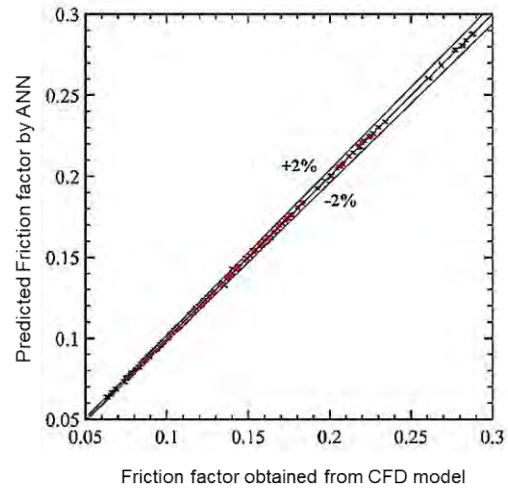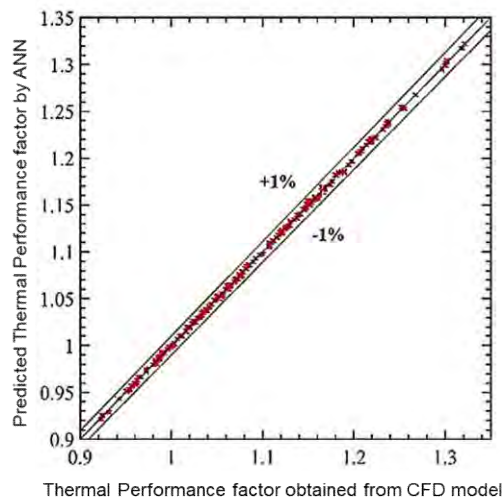

(b)

(c)

(d)

(e)

Fig. 6.4.1: Comparison between ANN predicted and computational (a) Nusselt number (Nu), (b) Friction factor (f), (c) Normalized Nusselt number (Nu/Nu_o), (d) Normalized friction factor (f/f_o), and (e) thermal performance factor (η).

6.5 Artificial Neural Network Results

6.5.1 Heat transfer analysis

The surface contours for normalized Nusselt number at Reynolds numbers 3477,10000, and 20866, are depicted in Fig. 6.5.1.1, Fig. 6.5.1.2, and 6.5.1.3, respectively. This figure represents the combined effect of different twisted tube parameters (y/w) and θ, and different helically corrugated tube parameters (Hl/D) and (pl/D) on the heat transfer enhancement in terms of normalized Nusselt number are visualized from Fig. 6.5.1.1, Fig. 6.5.1.2, and 6.5.1.3. All these figures are illustrated from the output of the developed ANN model. Comparing the figures between (y/w) = 3.5 and (y/w) = 5 in Fig. 6.5.1.1, Fig. 6.5.1.2, and 6.5.1.3, it can be observed that the surface contours are more highlighted for twisted tape with (y/w) = 3.5, for all tapered angles than the twisted tape with (y/w) = 5, for all tapered angle, respectively. The surface contours for tapered angle (θ) = 0°, for both twist ratios, the higher normalized Nusselt number have found in the region, where (pl/D) ranges from 0.5 to 1.0, and (Hl/D) ranges from 0.075 to 0.1 at three different Reynolds number. Similarly, the surface contours for tapered angle (θ) = 0.3°, for both twist ratios, the higher Normalized Nusselt number have found in the region, where (pl/D) ranges from 0.5 to 1.0, and (Hl/D) ranges from 0.07 to 0.1. An identical scene has also been observed for the surface contours for tapered angle (θ) = 0.5°, for both twist ratios, the higher normalized Nusselt numbers have found in the region, where (pl/D) ranges from 0.5 to 1.0, and (Hl/D) ranges from 0.085 to 0.1, at Reynolds number 3477 and 10000. However, at Reynolds number 20866, the higher normalized Nusselt number has been found in the region where (pl/D) ranges from 0.0 to 0.5, and (Hl/D) ranges from 0.09 to 0.1. It is evident from analyzing all the figures that the lower pitch-length-to-diameter ratio and higher height length-to-diameter ratio induces higher heat transfer enhancement in terms of normalized Nusselt number. On the contrary, for the higher pitch-length-to-diameter ratio and lower height length-to-diameter ratio, the minimum normalized Nusselt numbers are found in all the investigated cases. This means that the height of the grooves of the helically corrugated tubes has a significant effect on enhancing the heat transfer in heat exchangers. Besides, the pitch of the grooves of the corrugated tubes has less effect on enhancing the heat transfer. Moreover, Besides, it can be observed that with the increase of tapered angle of the twisted tape insert, the normalized Nusselt number for each case has decreased.
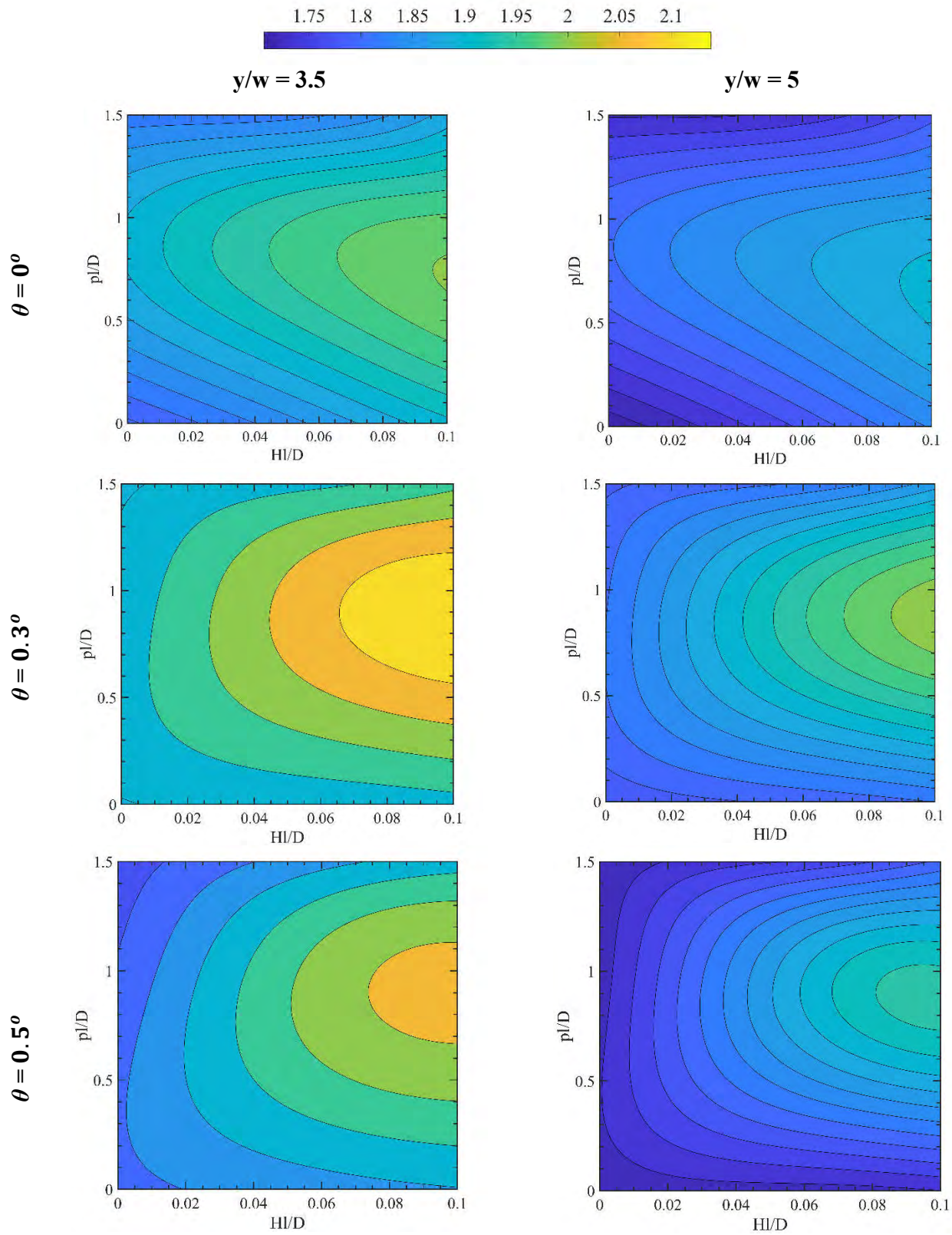
Fig. 6.5.1.1: Normalized Nusselt Number contour for different values of *y/w* and *θ* (Re = 3477)
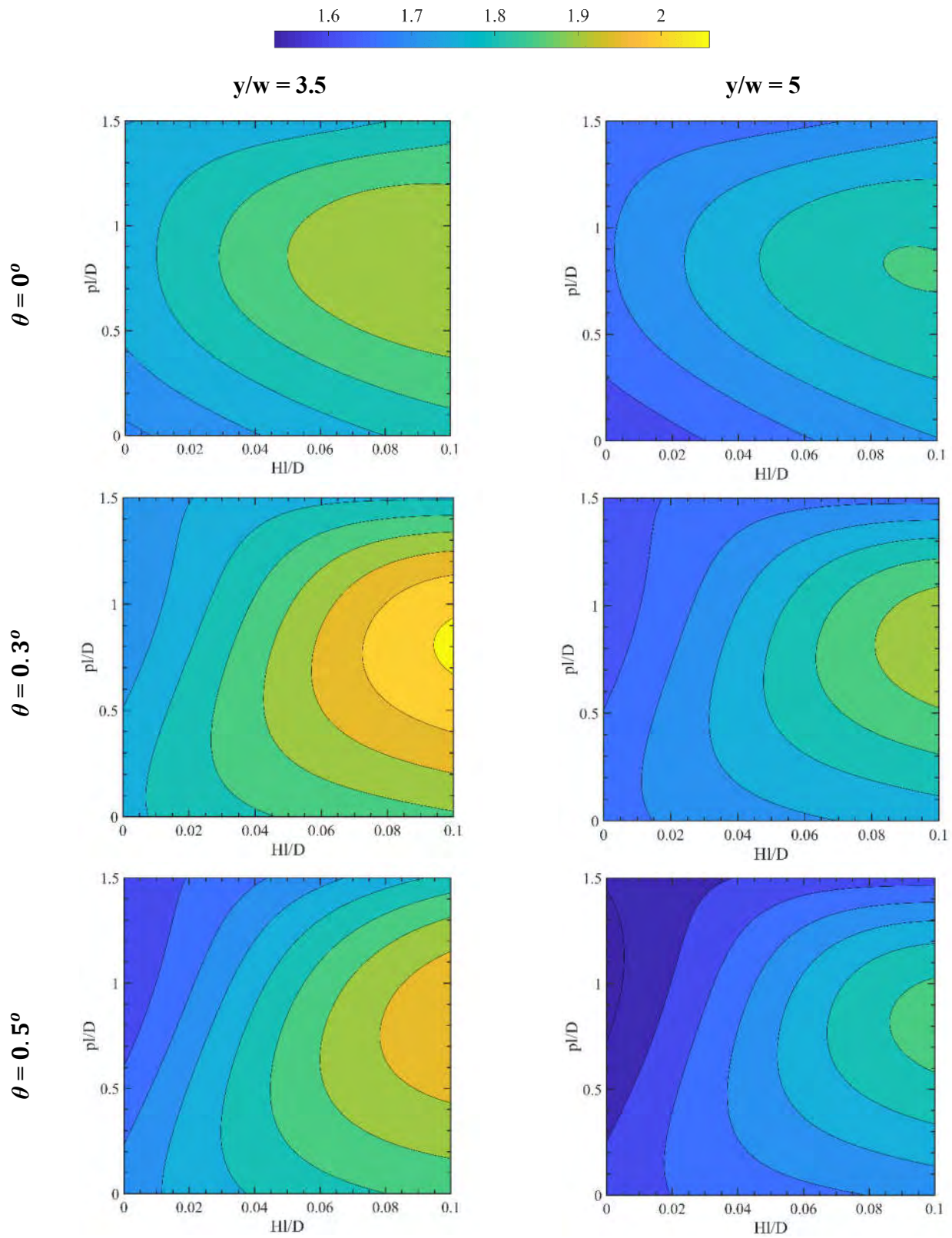
Fig. 6.5.1.2: Normalized Nusselt Number contour for different values of *y/w* and *θ* (Re = 10000)
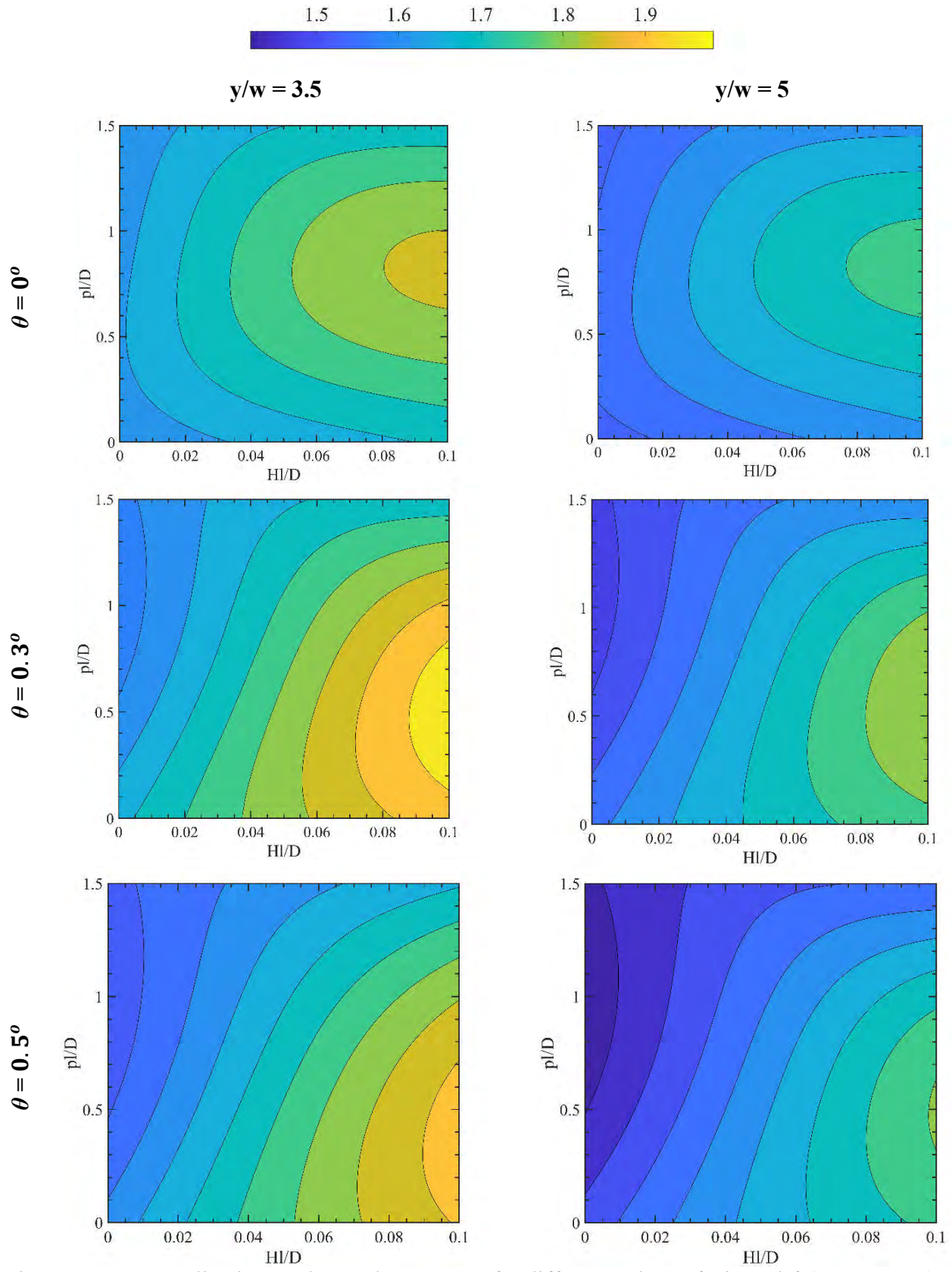
Fig. 6.5.1.3: Normalized Nusselt Number contour for different values of *y/w* and *θ* (Re = 20866)

Fig. 6.5.1.4 shows the normalized Nusselt number contours for different Reynolds numbers of 3477, 10000, and 20866. For each case, it has been seen that the higher normalized Nusselt number regions are located where the *Hl/D* is in the range of 0.08-0.1, and the *pl/D* is in the range of 0.5-1.0. In addition, it has been observed that with the increase of Reynolds number the heat transfer rate in terms of normalized Nusselt number has also increased.

Fig. 6.5.1.4: Normalized Nusselt number contours for twisted tape inserts [y/w = 3.5, θ = 0.3°] varying Reynolds number

6.5.2 Pressure drop analysis

Fig. 6.5.2.1, Fig. 6.5.2.2, and Fig. 6.5.2.3 depict the surface contours of normalized friction factor at Reynolds number 3477, 10000, and 20866, respectively, which represent the combined effect of different twisted tube parameters (y/w) and θ, and different helically corrugated tube parameters (Hl/D) and (pl/D) on the increased pressure drop across the tube in terms of normalized friction factor. All these figures are illustrated from the output of the ANN. Comparing the figures between (y/w) = 3.5 and (y/w) = 5, it can be observed that the surface contours are more highlighted for the twisted tape of (y/w) = 3.5, for all tapered angles than the twisted tape of (y/w) = 5, for all tapered angle, respectively. This indicates that the friction factor is higher for the twisted tape inserts with a twist ratio of 3.6. The surface contours for tapered angle (θ) = 0°, for both twist ratios, the maximum normalized friction factor have found in the region, where (pl/D) ranges from 0.5 to 1.5, and (Hl/D) ranges from 0.0 to 0.1. Similarly, the surface contours for tapered angle (θ) = 0.3°, for both twist ratios, the maximum normalized Nusselt number have found in the region, where (pl/D) ranges from 1.0 to 1.5, and (Hl/D) ranges from 0.05 to 0.1. An identical scene has also been observed for the surface contours for tapered angle (θ) = 0.5°, for both twist ratios at three different Reynolds numbers, the maximum normalized Nusselt numbers have found in the region, where (pl/D) ranges from 1.0 to 1.5, and (Hl/D) ranges from 0.05 to 0.1. Both the height of the grooves of the helically corrugated tubes and the pitch of the grooves has significant effects on enhancing the friction factor in heat exchangers. Besides, it can be observed that with the increase of the tapered angle of the twisted tape insert, the friction factor for each case has decreased.
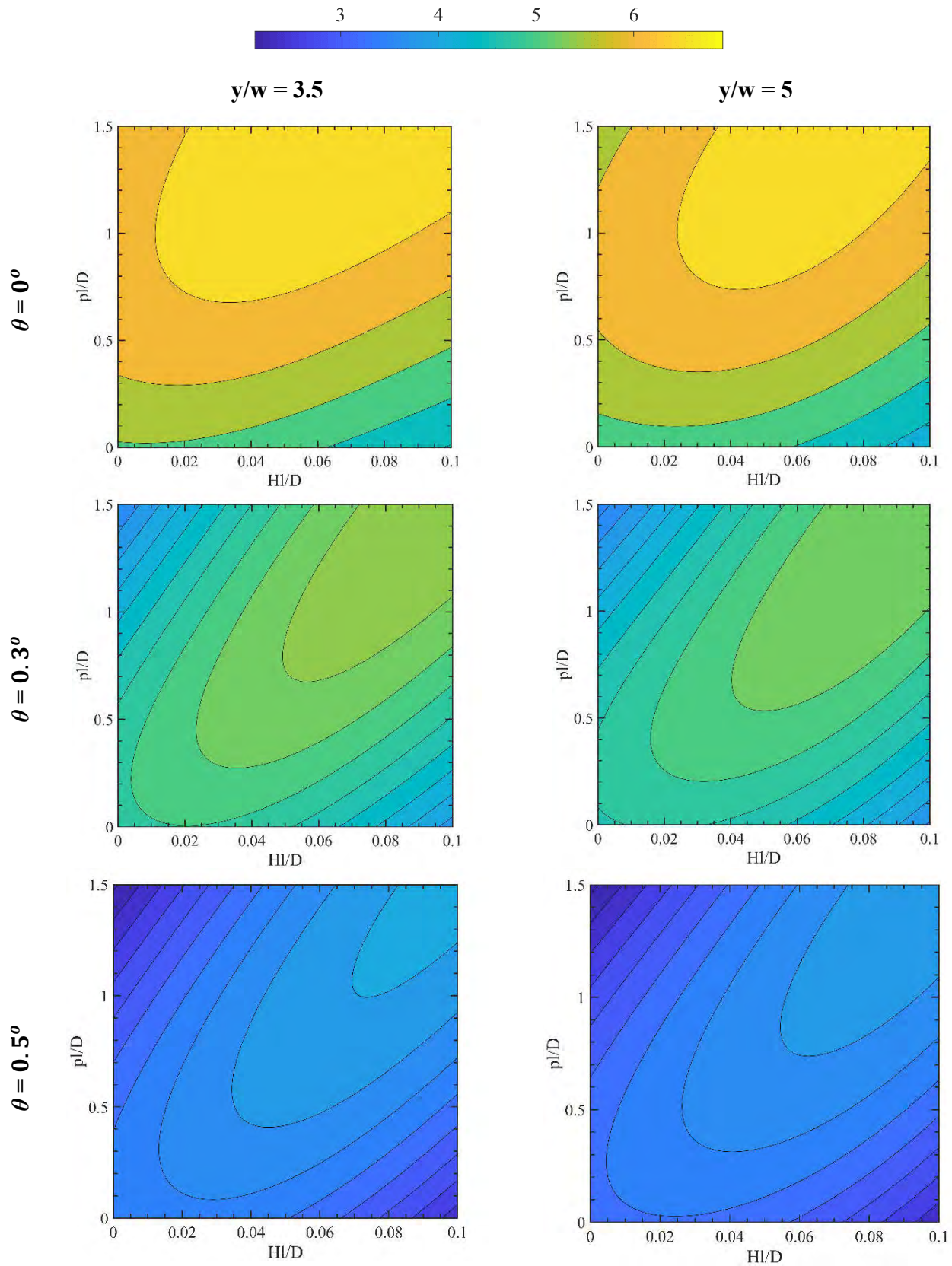
Fig. 6.5.2.1: Normalized friction factor contour for different values of *y/w* and θ (Re = 3477)
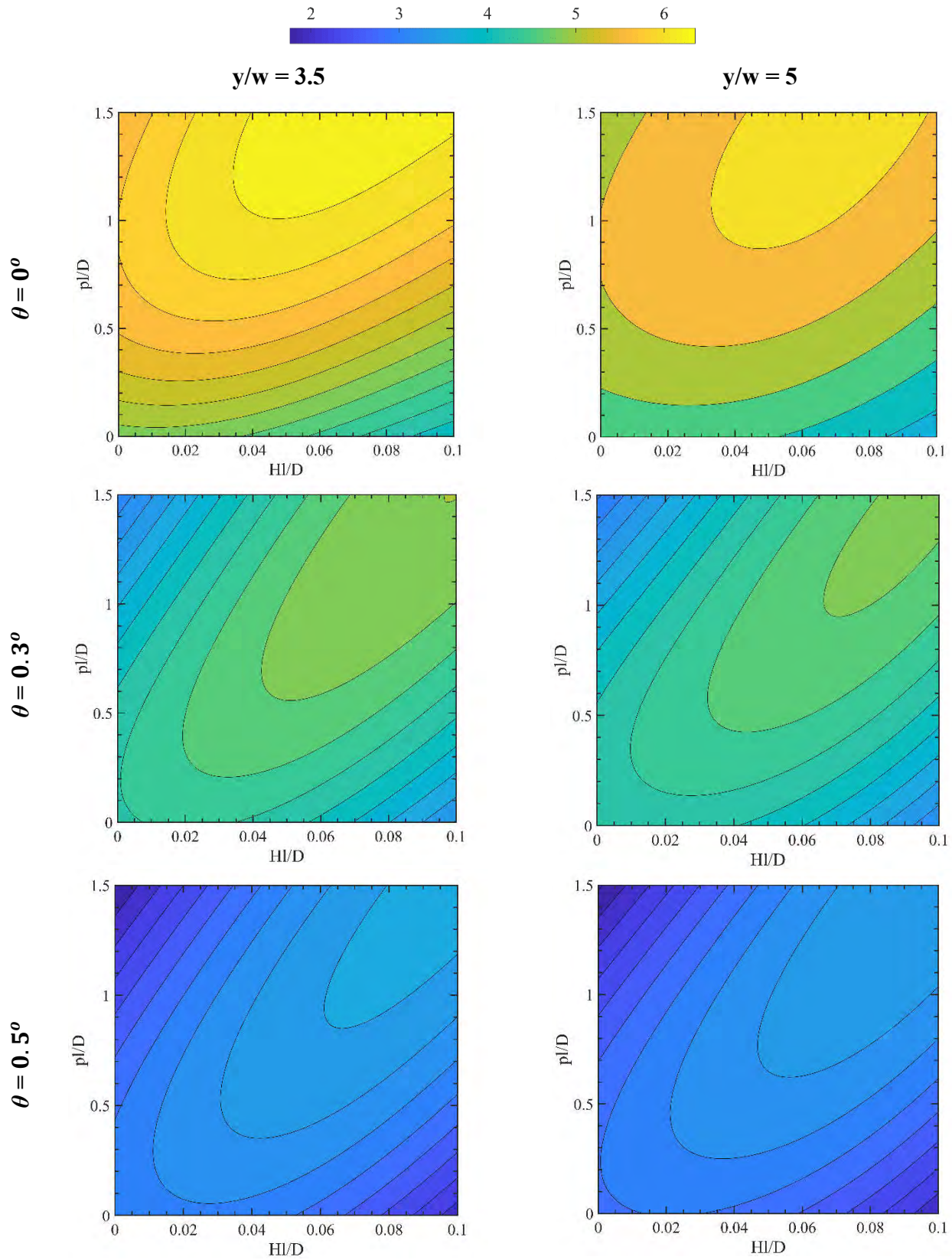
Fig. 6.5.2.3: Normalized friction factor contour for different values of *y/w* and *θ* (Re = 10000)

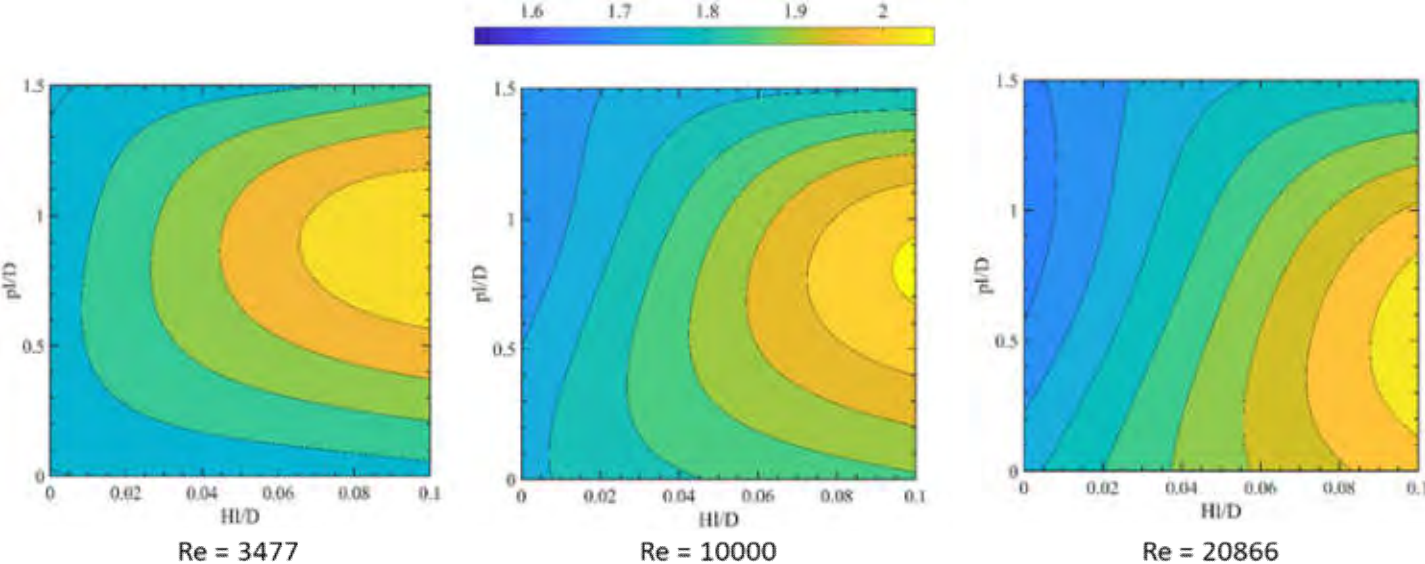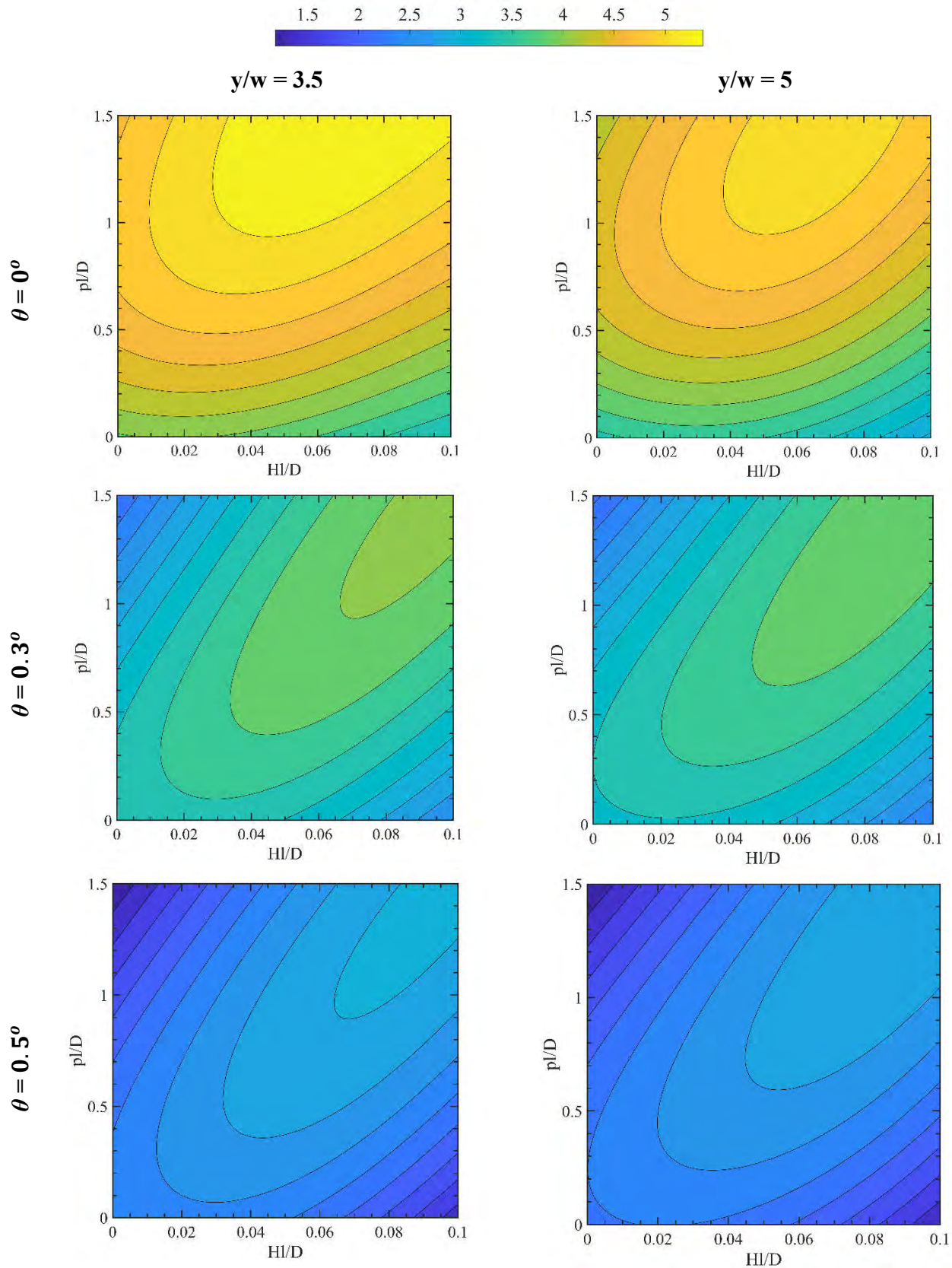Fig. 6.5.2.3: Normalized friction factor contour for different values of *y/w* and *θ* (Re = 20866.2121)

Fig. 6.5.2.4 illustrates the normalized friction factor contours for three different Reynolds numbers of 3477, 10000, and 20866. It has been found in all three cases, with the increase of *Hl/D* and *pl/D*, the normalized friction factor increases. The higher normalized friction factor region has been found in the range 0.05-0.1 of *Hl/D*, and 1.0-1.5 of *pl/D*. On the contrary, lower normalized friction factor regions have been found where either the *Hl/D* is minimum or the *pl/D* is minimum. Moreover, varying the Reynolds numbers, it has been observed that all the contours have shown a similar pattern for the normalized friction factor.

Fig. 6.5.2.4: Normalized Friction factor contours for twisted tape inserts [y/w = 3.5, θ = 0.3°] varying Reynolds number

6.5.3 Thermal performance factor analysis

From the artificial neural network (ANN), the surface contours of the thermal performance factor for the helically corrugated tubes, and the straight circular tube, with the different twisted tapes with the twist ratios of 3.5, and 5, and the tapered angles of 0°, 0.3°, and 0.5°, are illustrated in Fig. 6.5.3.1, Fig. 6.5.3.2, and Fig. 6.5.3.3, at Reynolds number 3477, 10000, and 20866, respectively. The more highlighted region indicates a higher thermal performance factor in these contours. The region located at the (pl/D) from 0 to 0.5, and the (Hl/D) of 0.1, shows maximum thermal performance factor for the twisted tapes with $y/w = 3.5$ and 5, at $\theta = 0°$, for all the studied cases. A similar pattern of surface contours of the thermal performance factor is observed for the twisted tape inserts with the same tapered angle of 0.3°, but different twist ratios of 3.5 and 5. In these cases, the relatively higher region of thermal performance factor is located where the pitch-length-to-diameter ratio lies in between 0.4 to 0.9, for ($y/w = 3.5$), and 0.4 to 1.05, for ($y/w = 5$) at three different Reynolds numbers. For these cases, the height-to-diameter ratio of the helically corrugated tubes lies between 0.08 to 0.1. From the surface contours for the twisted tapes with y/w = 3.5 and 5, at $\theta = 0.5°$, the region of relatively higher thermal performance factor is located at the $pl/D = 0.5$-1.0, and the $Hl/D = 0.1$ at all three Reynolds numbers of 3477, 10000, and 20866. From the figures of Fig. 6.5.3.1, Fig. 6.5.3.2, and Fig. 6.5.3.3, it is observed that with the increase of the pitch-length-to-tube-diameter ratio, and the decrease of the height-length-to-tube-diameter ratio of the corrugated tubes, the thermal performance factor for all the studied cases has decreased. Besides, with the decrease of the twist ratio of the twisted tape, the thermal performance factor increases. For instance, the surface contours of the twisted tape with the twist ratio of 3.5, are more highlighted compared to the twisted tape with the twist ratio of 5, for all the tapered angles ($\theta = 0°$, 0.3°, and 0.5°) of the twisted tape inserts.
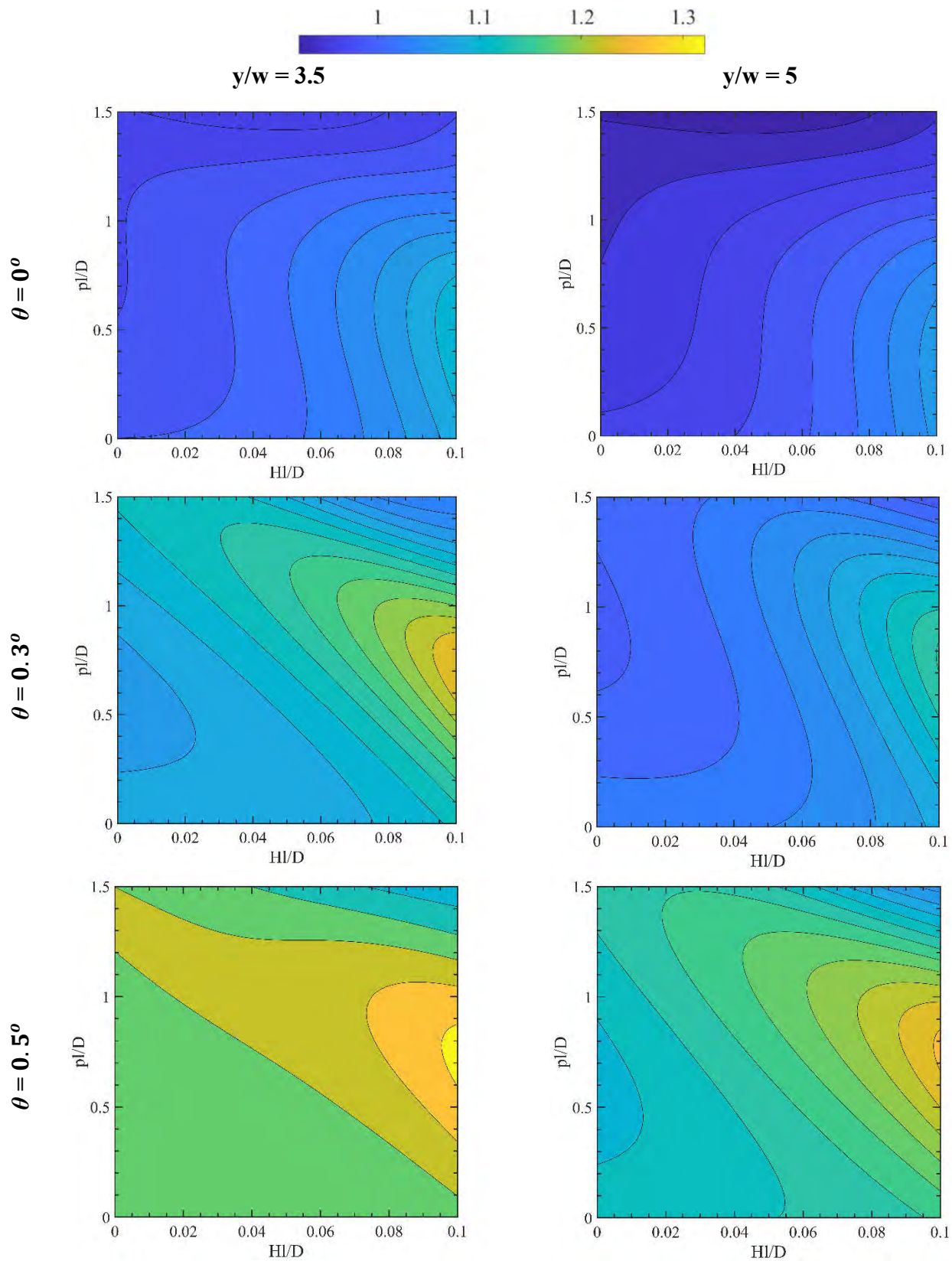
Fig. 6.5.3.1: Thermal performance factor contour for different values of *y/w* and *θ* (Re = 3477.702)

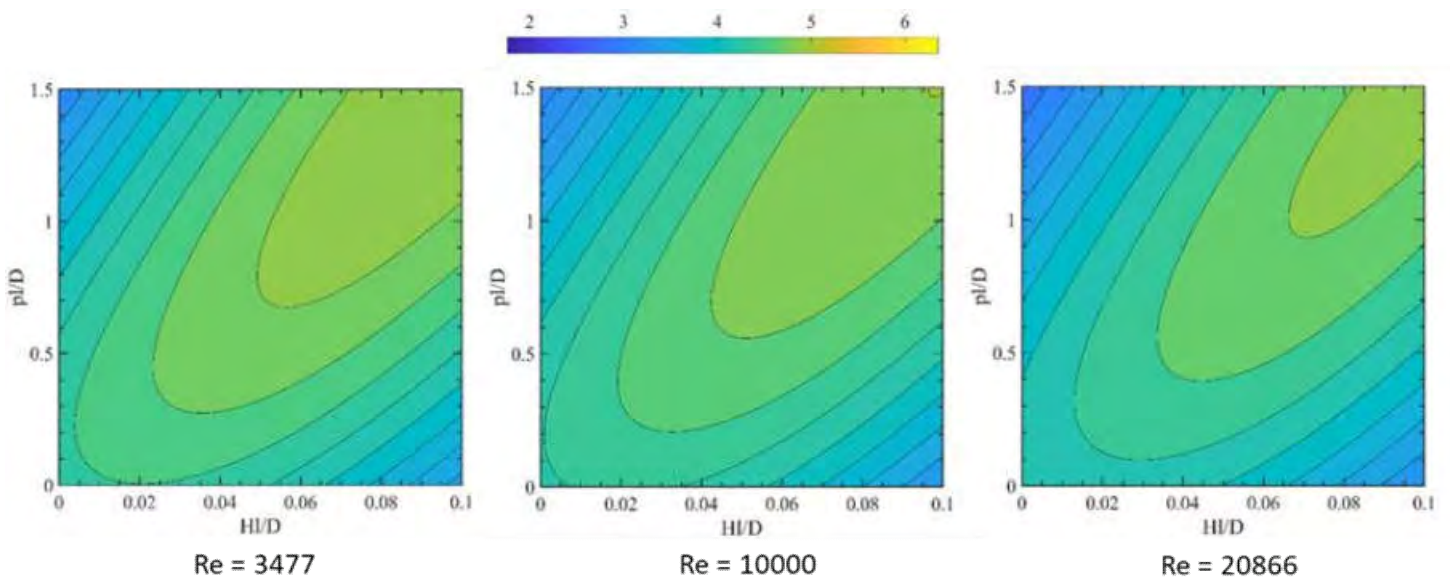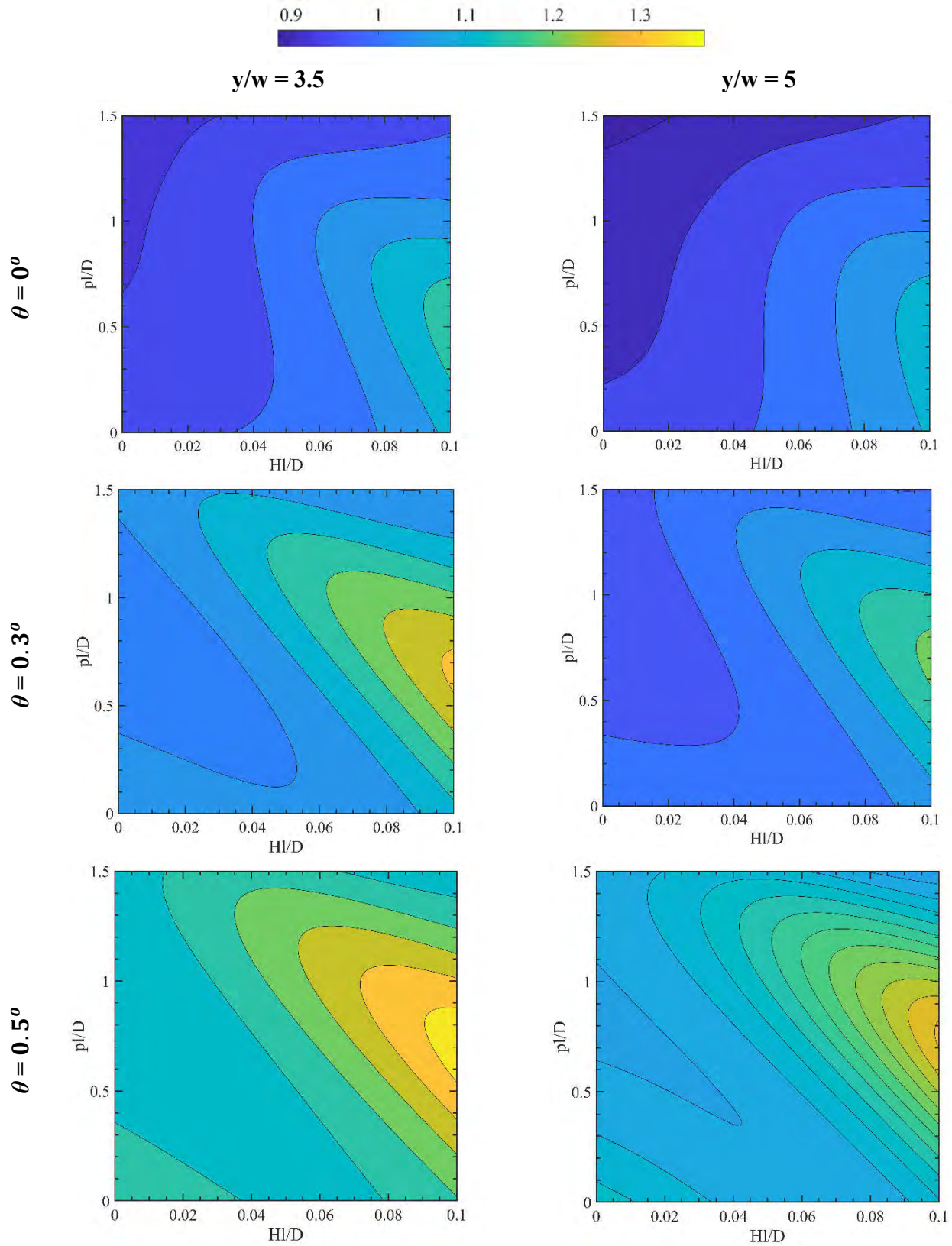Fig. 6.5.3.2: Thermal performance factor contour for different values of y/w and θ (Re = 10000)
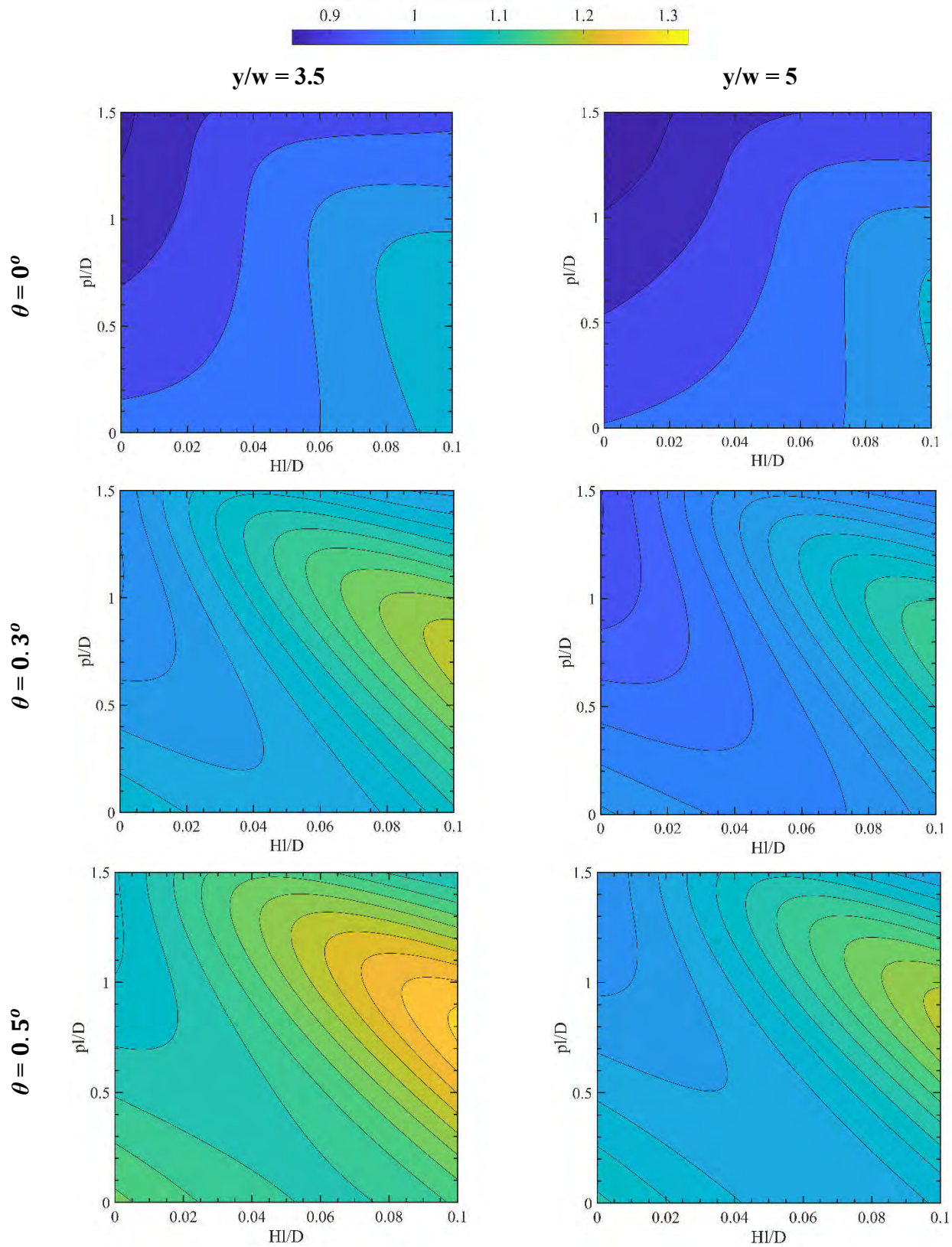
Fig. 6.5.3.3: Thermal performance factor contour for different values of *y/w* and *θ* (Re = 20866)

Fig. 6.5.3.4 depicts the thermal performance factor contours for three different Reynolds numbers 3477, 10000, and 20866. A similar pattern of contours has been found for different Reynolds numbers. In each case (see Fig. 6.5.3.4), a higher thermal performance factor region has been found for Hl/D in the range of 0.09-0.1, and pl/D in the range of 0.5-1.0. In addition, it has been observed that with the increase of Reynolds number, the thermal performance factor increases.
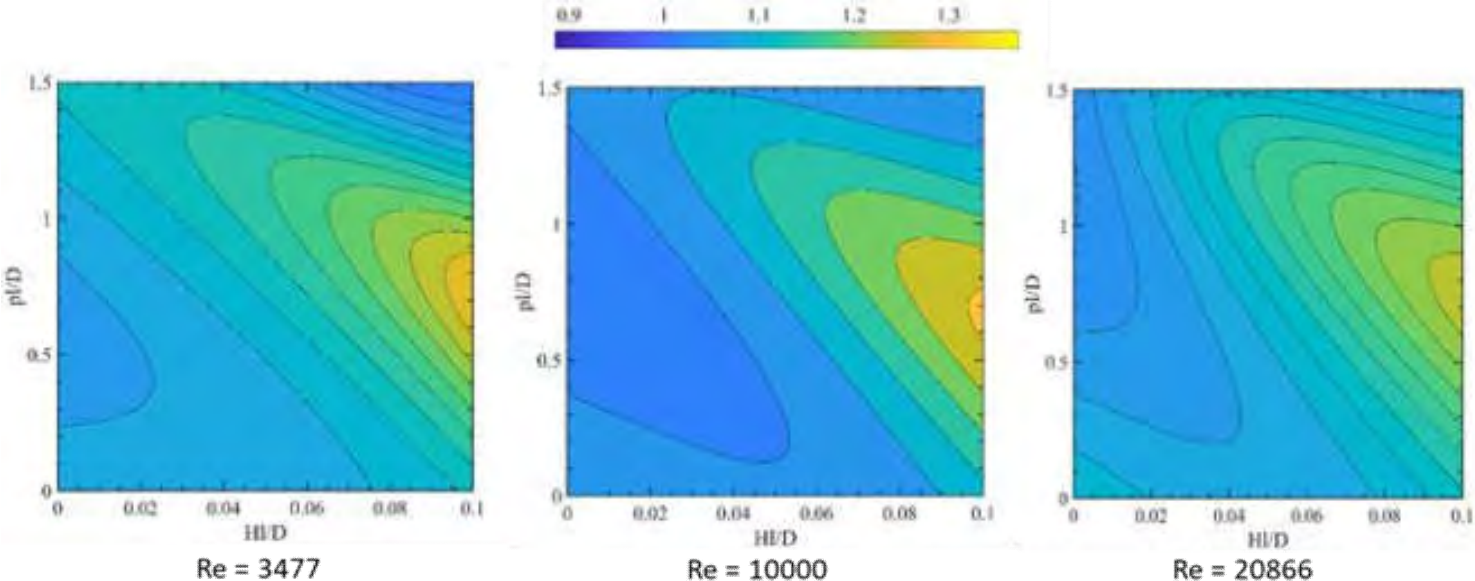
Fig. 6.5.3.4: Thermal performance factor contours for twisted tape inserts [y/w = 3.5, θ = 0.3°] varying Reynolds number

6.6 Non-Linear Correlations from ANN model

Numerous studies have been reported that consider various turbulent promoters of different shapes and types, and various designs of corrugated tubes, to enhance the heat transfer rate. Several correlations have been proposed to evaluate the Nusselt number, friction factor, and thermal performance factor in dif0oferent studies [21,22,28,29,40,46]. In this present study, an effort has been made to obtain empirical correlations to predict the Nusselt number, friction factor, and thermal performance factor of the tapered twisted tape inserted into the corrugated tube, where $3400 < \text{Re} < 21000$.

$$Nu = 0.1806\, \text{Re}^{0.6699} \left(\frac{y}{w}\right)^{-0.1714} (1 + sin\theta)^{-1.8146} \left(\frac{Hl}{D}\right)^{0.0577} \left(\frac{pl}{D}\right)^{-0.1853} \tag{45}$$

$$f = 9.5561\, \text{Re}^{-0.3949} \left(\frac{y}{w}\right)^{-0.0985} (1 + sin\theta)^{-64.9921} \left(\frac{Hl}{D}\right)^{0.0422} \left(\frac{pl}{D}\right)^{-0.0035} \tag{46}$$

$$\eta = 1.4384\, \text{Re}^{-0.0042} \left(\frac{y}{w}\right)^{-0.1414} (1 + sin\theta)^{19.2084} \left(\frac{Hl}{D}\right)^{0.0330} \left(\frac{pl}{D}\right)^{-0.2068} \tag{47}$$

The relations are fitted using a normal equation [82]. Total 140 sets of data obtained from the simulations have been used to fit the equations. Normal Equation is an analytic approach to linear regression with a least square loss function. It is implemented by setting equal to zero the partial derivatives of the sum of squared errors, which in the present case, is the loss function. Following, this approach is an effective and time-saving option for working with a dataset with small features. However, our present relations are in the form of an Equation. 45 are not linear.

$$Y = A \left(\frac{y}{w}\right)^{\theta_1} (1 + sin\theta)^{\theta_2} \left(\frac{Hl}{D}\right)^{\theta_3} \left(\frac{pl}{D}\right)^{\theta_4} \text{Re}^{\theta_5} \tag{48}$$

Here, Y is the output value such as Nusselt number, friction factor, etc. θ_n (n = 1,2…) and A are unknown parameters. Eqn. 48 has been transformed into a linear form using logarithmic operation.

$$\log(Y) = \theta_o + \theta_1 log\left(\frac{y}{w}\right) + \theta_2 log(1 + sin\theta) + \theta_3 log\left(\frac{Hl}{D}\right) + \theta_4 log\left(\frac{pl}{D}\right) + \theta_5 log\,(Re) \tag{49}$$

Here, θ_0 is equal to log(A). After converting the non-linear Equation. 48 to linear Equation. 49, normal equation has been used to obtain the values of θ_n (n = 0,1,2…). The form of normal equation used in the present study is:

$$\theta_n = (X^T X)^{-1}(X^T y) \tag{50}$$

Here,

$$X = \begin{bmatrix} 1 & log\left(\frac{y}{w}\right) & log(1+sin\theta) & log\left(\frac{Hl}{D}\right) & log\left(\frac{pl}{D}\right) & log\left(Re\right) \\ \cdot & \cdot & \cdot & \cdot & \cdot & \cdot \\ \cdot & \cdot & \cdot & \cdot & \cdot & \cdot \end{bmatrix} \qquad (51)$$

$$Y = \begin{bmatrix} log(Y) \\ \cdot \\ \cdot \end{bmatrix} \qquad (52)$$

The exponent of Reynolds number in the proposed correlation Equation (45) is found to vary significantly based on the design of the turbulence promoters. Turbulent promoters were found to disrupt the boundary layer by generating recirculation inside the flow regime and increase the turbulent intensity. These turbulent promoters provide higher heat transfer surface area and were found to affect the heat transfer rate significantly. Because of this, the exponent of the Reynolds number is higher in the present proposed correlations Equation (45). Earlier researchers have reported similar observations in their investigation [22,30,36,37]. The friction factor correlation Equation (46) is found to be the weak function of the Reynolds number. The exponent of Reynolds number for the present correlation is similar to the previous correlations [22,30,32,37] for the turbulators. While using the twisted tape insert in the corrugated tube, the friction factor strongly depends on the Reynolds number. This may be the reason that the friction factor is a weak function for the present proposed correlation for the designed heat exchanger.

To evaluate the validity of the proposed empirical correlations, an effort has been made to compare the predicted Nusselt number, friction factor, and thermal performance factor, against the Nusselt number, friction factor, and thermal performance factor determined from the computational analysis, in Fig. 6.6.1, 6.6.2, and 6.6.3. As seen in Fig. 6.6.1, the proposed correlation for the Nusselt number Equation (45) can predict the values within an error band of ±4%. While from Fig. 6.6.2, it is observed that the proposed correlation for the friction factor Equation (46) can predict data within an error band of ±5%. While in the case of the thermal performance factor of the studied model, from Fig. 6.6.3, it is seen that the proposed correlation Equation (47) can predict the test data within an error band of ±5%. The error bands of the empirical correlation are in good agreement with the previously reported studies [32, 37].

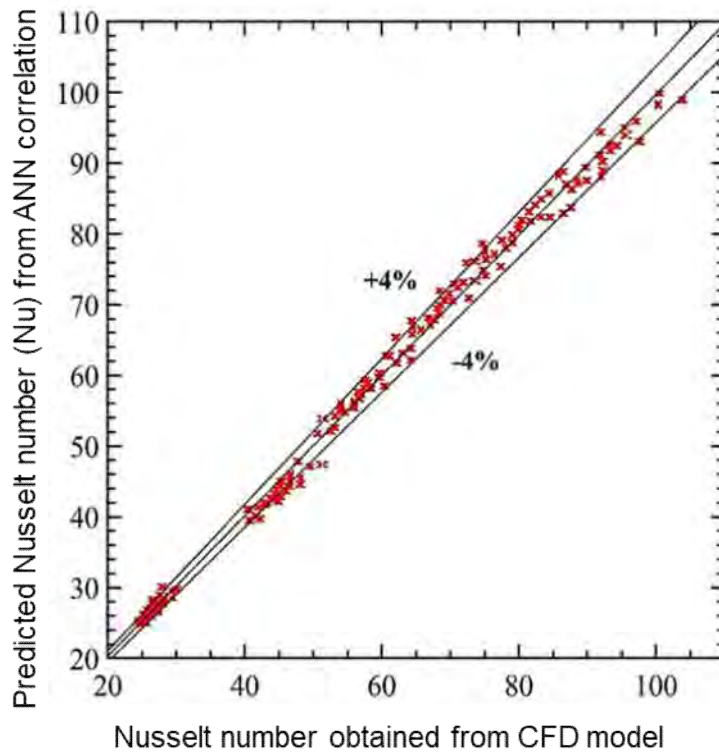Fig. 6.6.1: Comparison of the obtained correlation [Equation 45] predicted Nusselt number against the computational Nusselt number.
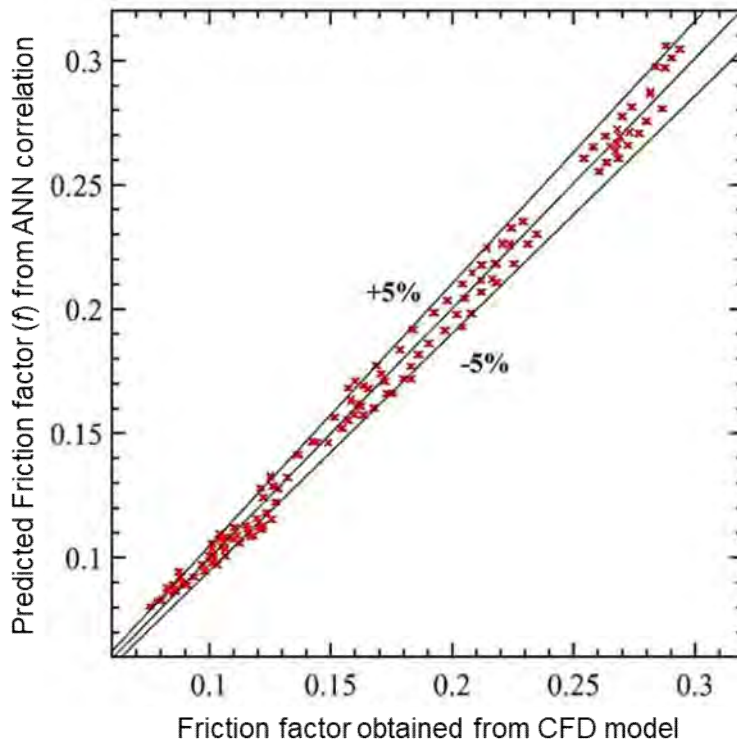

Fig. 6.6.2: Comparison of the obtained correlation [Equation 46] predicted friction factor against the computational friction factor.
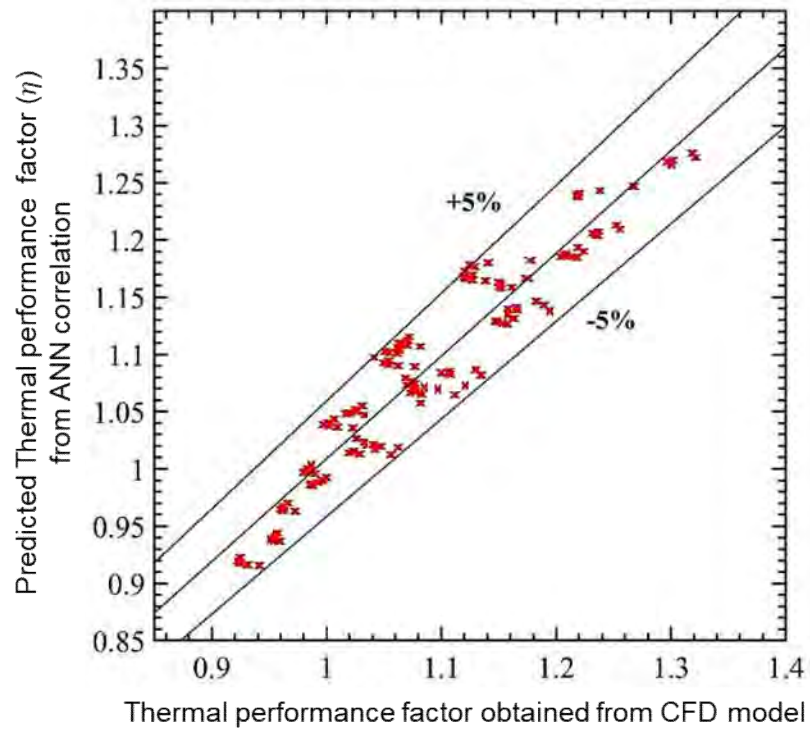
Fig. 6.6.3: Comparison of the obtained correlation [Equation 47] predicted thermal performance factor against the computational thermal performance factor.

CHAPTER 7

Conclusion and Future Recommendations

7.1 Conclusion

The heat transfer, friction factor, and thermal performance factor characteristics of turbulent flow inside the straight circular tube (SCT), and the helically corrugated tubes (HCT) with two different pitch-to-diameter ratios (pl/D = 1 and 1.5), and two different height-to-diameter ratios (Hl/D = 0.05 and 0.1), inserted with tapered twisted tapes at two different twist ratios (y/w = 3.5 and 5) and three different tapered angles (θ = 0°, 0.3°, and 0.5°) have numerically investigated for Reynolds number ranging from 3400 to 21000 in this study. Subsequently, the validation has been conducted with the heat transfer and the friction factor characteristics for the straight circular tube, helically corrugated tube, and straight circular tube with tapered twisted tape inserts with the empirical correlations, respectively, reported in current literature. The numerical study has been performed using the shear stress transport (SST) k-ω turbulence model in the ANSYS Fluent software. The main conclusions that are drawn from the investigation are summarized as follows:

1. A comparative study has been conducted among the SST k-ω, Standard k-ω, Standard k-ϵ, and RNG k-ϵ turbulence models against standard empirical correlations for Nu and f. The results obtained from the SST k-ω turbulence model have been found more conforming to the correlations compared to other turbulence models. Therefore, for the present study, the SST k-ω turbulence model has been selected.

2. From the heat transfer enhancement point of view, twisted tape with the lower twist ratio and tapered angle has exhibited a higher heat transfer rate as it has induced higher swirl in the fluid domain, disturbing the thermal boundary layer which has resulted in higher heat transfer compared to other twisted tapes. In the current study, the tapered twisted tape (y/w = 3.5 and θ = 0°) inserted in the helically corrugated tube (pl/D = 1.0, Hl/D = 0.1) has exhibited comparatively higher heat transfer enhancement than the other corrugated tubes and the straight circular tube.

3. The pressure-drop has been dropped significantly with the increase in the tapered angle of the twisted tape. Moreover, the higher twist ratio of the tapered twisted tape has decreased the pressure-drop inside the tubes. In the present investigation, the pressure drop in terms

of normalized friction factor has been found minimum for the tapered twisted tape ($y/w = 5$ and $\theta = 0.5°$) and the helically corrugated tube ($pl/D = 1.5$, $Hl/D = 0.05$).

4. The ultimate performance evaluation parameter the thermal performance factor has been found maximum for the case 25 (TTT: $y/w = 3.5$ and $\theta = 0.5°$; HCT: $Hl/D = 0.1$, $pl/D = 1.0$). For this case, the thermal performance factor has increased about 32% than the straight circular tube without any insertion of twisted tapes.

5. Using helically corrugated tube ($Hl/D = 0.1$, $pl/D = 1.0$) with tapered twisted tape insert ($y/w = 3.5$ and $\theta = 0.5°$), the present study has found about 48% more enhanced thermal performance factor compared to a study with tapered twisted tape inserted ($y/w = 3.5$ and $\theta = 0.5°$) into a straight circular tube reported in the current literature.

6. The predicted values of the performance factors from the trained artificial neural network (ANN) are in good agreement with the results of the computational investigation, with error bands of 2% for the Nusselt number, friction factor, and 1% for the normalized Nusselt number, normalized friction factor and thermal performance factor, respectively.

7. The obtained empirical correlations have shown good accuracy in predicting the Nusselt number, friction factor, and thermal performance factor, with error bands of ±4%, ±5%, and ±5%, respectively, against the computationally analyzed Nusselt number, friction factor, and thermal performance factor.

Thus, from the consideration of enhanced heat transfer, the tapered twisted tape inserts inside the corrugated tubes are seen to be attractive for enhancing the turbulent flow heat transfer in the heat exchanger.

7.2 Future Recommendations

The principal objective of the present study was to computationally analyze the overall performance characteristics and design a model of an optimized heat exchanger which can be used as a compact heat exchanger in different industries. Besides, there are more scopes to improve the present work in terms of enhancing the overall performance of the developed model of the heat exchanger to get more insight into the study. In this regard some recommendations are given below:

a) In this study, the air was considered as the working fluid. Using different refrigerants or nanofluids can be used as working fluid to assess the performance of the developed model. Since different refrigerants are being used as working fluids in refrigeration industries and waste heat recovery systems.

b) The current investigation was conducted for a certain range of turbulent flow, so in the future, the study can be conducted for laminar flow region as well as extended turbulent flow region with multi-channels twisted tape inserts working as turbulators inside micro-structured surface tubes

c) Moreover, any numerical and artificial neural network predicted investigation is incomplete without experimental verification. Therefore, the verification of the present study can be done by experimental testing of the study.

REFERENCES

[1] Li, L., Li, Y., & Sun, J. (2017). Prospective fully-coupled multi-level analytical methodology for concentrated solar power plants: Applications. Applied Thermal Engineering, 118, 159–170. https://doi.org/10.1016/j.applthermaleng.2017.02.094

[2] Li, L., Sun, J., & Li, Y. (2017). Prospective fully-coupled multi-level analytical methodology for concentrated solar power plants: General modelling. Applied Thermal Engineering, 118, 171–187. https://doi.org/10.1016/j.applthermaleng.2017.02.086

[3] Cheppudira Thimmaiah, P., Sharafian, A., Huttema, W., Osterman, C., Ismail, A., Dhillon, A., & Bahrami, M. (2016). Performance of finned tubes used in low-pressure capillary-assisted evaporator of adsorption cooling system. Applied Thermal Engineering, 106, 371–380. https://doi.org/10.1016/j.applthermaleng.2016.06.038

[4] Bhuiya, M. M. K., Azad, A. K., Chowdhury, M. S. U., & Saha, M. (2016). Heat transfer augmentation in a circular tube with perforated double counter twisted tape inserts. International Communications in Heat and Mass Transfer, 74, 18–26. https://doi.org/10.1016/j.icheatmasstransfer.2016.03.001

[5] Soltanimehr, M., & Afrand, M. (2016). Thermal conductivity enhancement of COOH-functionalized MWCNTs/ethylene glycol–water nanofluid for application in heating and cooling systems. Applied Thermal Engineering, 105, 716–723. https://doi.org/10.1016/j.applthermaleng.2016.03.089

[6] Chen, X., Su, Y., Reay, D., & Riffat, S. (2016). Recent research developments in polymer heat exchangers – A review. Renewable and Sustainable Energy Reviews, 60, 1367–1386. https://doi.org/10.1016/j.rser.2016.03.024

[7] Kurtulmuş, N., & Sahin, B. (2019). A review of hydrodynamics and heat transfer through corrugated channels. International Communications in Heat and Mass Transfer, 108, 104307. https://doi.org/10.1016/j.icheatmasstransfer.2019.104307

[8] Li, L., Li, Y., & Sun, J. (2017). Prospective fully-coupled multi-level analytical methodology for concentrated solar power plants: Applications. Applied Thermal Engineering, 118, 159–170. https://doi.org/10.1016/j.applthermaleng.2017.02.094

[9] Cheppudira Thimmaiah, P., Sharafian, A., Huttema, W., Osterman, C., Ismail, A., Dhillon, A., & Bahrami, M. (2016). Performance of finned tubes used in low-pressure capillary-assisted evaporator of adsorption cooling system. Applied Thermal Engineering, 106, 371–380. https://doi.org/10.1016/j.applthermaleng.2016.06.038

[10] A. E. Bergles, Techniques to augment heat transfer, in Handbook of Heat Transfer Applications, 2nd edition (McGraw-Hill, New York, 1985), ch.1.

[11] Panahi, D., & Zamzamian, K. (2017). Heat transfer enhancement of shell-and-coiled tube heat exchanger utilizing helical wire turbulator. Applied Thermal Engineering, 115, 607–615. https://doi.org/10.1016/j.applthermaleng.2016.12.128

[12] Feng, Z., Luo, X., Guo, F., Li, H., & Zhang, J. (2017). Numerical investigation on laminar flow and heat transfer in rectangular microchannel heat sink with wire coil inserts. Applied Thermal Engineering, 116, 597–609. https://doi.org/10.1016/j.applthermaleng.2017.01.091

[13] Sajadi, B., Najafizadeh, M. M., Soleimani, M., Akhavan Behabadi, M. A., & Naserinejad, J. (2019). The effect of wire-coil inserts on the heat transfer and pressure drop of R1234yf flow boiling. Applied Thermal Engineering, 152, 615–623. https://doi.org/10.1016/j.applthermaleng.2019.02.115

[14] Yan, H., Feng, S., Lu, T., & Xie, G. (2017). Experimental and numerical study of turbulent flow and enhanced heat transfer by cross-drilled holes in a pin-finned brake disc. International Journal of Thermal Sciences, 118, 355–366. https://doi.org/10.1016/j.ijthermalsci.2017.04.024

[15] Aziz, A., Alsaedi, A., Muhammad, T., & Hayat, T. (2018). Numerical study for heat generation/absorption in flow of nanofluid by a rotating disk. Results in Physics, 8, 785–792. https://doi.org/10.1016/j.rinp.2018.01.009

[16] Capata, R., & Beyene, A. (2017). Experimental evaluation of three different configurations of constructal disc-shaped heat exchangers. International Journal of Heat and Mass Transfer, 115, 92–101. https://doi.org/10.1016/j.ijheatmasstransfer.2017.06.096

[17] Ahmed, J. A., (2007). Heat transfer in turbulent flow through tube with porous twisted tape insert, Master of Science in Mechanical Engineering, Department of Mechanical Engineering, Bangladesh University of Engineering and Technology.

[18] Ambreen, T., Saleem, A., & Park, C. W. (2019). Pin-fin shape-dependent heat transfer and fluid flow characteristics of water- and nanofluid-cooled micropin-fin heat sinks: Square, circular and triangular fin cross-sections. Applied Thermal Engineering, 158, 113781. https://doi.org/10.1016/j.applthermaleng.2019.113781

[19] Haque, M. R., (2016). Numerical study of forced convection heat transfer over circular and oval tube banks using vortex generators, Master of Science in Mechanical Engineering, Department of Mechanical Engineering, Bangladesh University of Engineering and Technology.

[20] Sadeghianjahromi, A., Kheradmand, S., Nemati, H., & Wang, C.-C. (2020). Heat transfer enhancement of wavy fin-and-tube heat exchangers via innovative compound designs. International Journal of Thermal Sciences, 149, 106211. https://doi.org/10.1016/j.ijthermalsci.2019.106211

[21] Omidi, M., Farhadi, M., & Ali Rabienataj Darzi, A. (2018). Numerical study of heat transfer on using lobed cross sections in helical coil heat exchangers: Effect of physical and geometrical parameters. Energy Conversion and Management, 176, 236–245. https://doi.org/10.1016/j.enconman.2018.09.034

[22] Yadav, S., & Sahu, S. K. (2019). Heat transfer augmentation in double pipe water to air counter flow heat exchanger with helical surface disc turbulators. Chemical Engineering and Processing - Process Intensification, 135, 120–132. https://doi.org/10.1016/j.cep.2018.11.018

[23] Cui, W., Mao, D., Lin, B., & Yang, J. (2019). Field synergy analysis on the mechanism of heat transfer enhancement by using nanofluids. Case Studies in Thermal Engineering, 16, 100554. https://doi.org/10.1016/j.csite.2019.100554

[24] Baba, M. S., Raju, A. V. S. R., & Rao, M. B. (2018). Heat transfer enhancement and pressure drop of Fe3O4 -water nanofluid in a double tube counter flow heat exchanger with internal

longitudinal fins. Case Studies in Thermal Engineering, 12, 600–607. https://doi.org/10.1016/j.csite.2018.08.001

[25] Said, Z., Rahman, S. M. A., El Haj Assad, M., & Alami, A. H. (2019). Heat transfer enhancement and life cycle analysis of a Shell-and-Tube Heat Exchanger using stable CuO/water nanofluid. Sustainable Energy Technologies and Assessments, 31, 306–317. https://doi.org/10.1016/j.seta.2018.12.020

[26] Han, D., He, W. F., & Asif, F. Z. (2017). Experimental study of heat transfer enhancement using nanofluid in double tube heat exchanger. Energy Procedia, 142, 2547–2553. https://doi.org/10.1016/j.egypro.2017.12.090

[27] Ravi Kumar, N. T., Bhramara, P., Kirubeil, A., Syam Sundar, L., Singh, M. K., & Sousa, A. C. M. (2018). Effect of twisted tape inserts on heat transfer, friction factor of Fe3O4 nanofluids flow in a double pipe U-bend heat exchanger. International Communications in Heat and Mass Transfer, 95, 53–62. https://doi.org/10.1016/j.icheatmasstransfer.2018.03.020

[28] Eiamsa-ard, S., Wongcharee, K., & Sripattanapipat, S. (2009). 3-D Numerical simulation of swirling flow and convective heat transfer in a circular tube induced by means of loose-fit twisted tapes. International Communications in Heat and Mass Transfer, 36(9), 947–955. https://doi.org/10.1016/j.icheatmasstransfer.2009.06.014

[29] Sarada, S. N., Raju, A. V. S. R., Radha, K. K., & Sunder, L. S. (2011). Enhancement of heat transfer using varying width twisted tape inserts. International Journal of Engineering, Science and Technology, 2(6), 107–111. https://doi.org/10.4314/ijest.v2i6.63702

[30] Eiamsa-ard, S., & Promvonge, P. (2018). Performance assessment in a heat exchanger tube with alternate clockwise and counter-clockwise twisted-tape inserts. International Journal of Heat and Mass Transfer, 53(7–8), 1364–1372. https://doi.org/10.1016/j.compfluid.2010.12.034

[31] Bas, H., & Ozceyhan, V. (2012). Heat transfer enhancement in a tube with twisted tape inserts placed separately from the tube wall. Experimental Thermal and Fluid Science, 41, 51–58. https://doi.org/10.1016/j.expthermflusci.2012.03.008

[32] Eiamsa-ard, S., Yongsiri, K., Nanan, K., & Thianpong, C. (2012). Heat transfer augmentation by helically twisted tapes as swirl and turbulence promoters. Chemical Engineering and Processing: Process Intensification, 60, 42–48. https://doi.org/10.1016/j.cep.2012.06.001

[33] Chowdhury, M. S., (2019). Numerical study of heat transfer performance of nanofluid in circular pipe with combined rib and rotating twisted tape, Master of Science in Mechanical Engineering, Department of Mechanical Engineering, Bangladesh University of Engineering and Technology.

[34] Ji, W.-T., Jacobi, A. M., He, Y.-L., & Tao, W.-Q. (2015). Summary and evaluation on single-phase heat transfer enhancement techniques of liquid laminar and turbulent pipe flow. International Journal of Heat and Mass Transfer, 88, 735–754. https://doi.org/10.1016/j.ijheatmasstransfer.2015.04.008

[35] Mashoofi, N., Pourahmad, S., & Pesteei, S. M. (2017). Study the effect of axially perforated twisted tapes on the thermal performance enhancement factor of a double tube heat exchanger.

Case Studies in Thermal Engineering, 10, 161–168. https://doi.org/10.1016/j.csite.2017.06.001

[36] Kunlabud, S., Chuwattanakul, V., Kongkaitpaiboon, V., Promthaisong, P., & Eiamsa-ard, S. (2017). Heat transfer in turbulent tube flow inserted with loose-fit multi-channel twisted tapes as swirl generators. Theoretical and Applied Mechanics Letters, 7(6), 372–378. https://doi.org/10.1016/j.taml.2017.11.011

[37] Promvonge, P. (2008). Thermal augmentation in circular tube with twisted tape and wire coil turbulators. Energy Conversion and Management, *49*(11), 2949–2955. https://doi.org/10.1016/j.enconman.2008.06.022

[38] Tusar, M., Noman, A., Islam, M., Yarlagadda, P., & Salam, B. (2019). CFD study of heat transfer enhancement and fluid flow characteristics of turbulent flow through tube with twisted tape inserts. Energy Procedia, 160, 715–722. https://doi.org/10.1016/j.egypro.2019.02.188

[39] Saysroy, A., & Eiamsa-ard, S. (2017). Enhancing convective heat transfer in laminar and turbulent flow regions using multi-channel twisted tape inserts. International Journal of Thermal Sciences, 121, 55–74. https://doi.org/10.1016/j.ijthermalsci.2017.07.002

[40] Abolarin, S. M., Everts, M., & Meyer, J. P. (2019). Heat transfer and pressure drop characteristics of alternating clockwise and counter clockwise twisted tape inserts in the transitional flow regime. International Journal of Heat and Mass Transfer, 133, 203–217. https://doi.org/10.1016/j.ijheatmasstransfer.2018.12.107

[41] Ramakumar, B. V. N., Arsha, J. D., & Tayal, P. (2015). Tapered Twisted Tape Inserts for Enhanced Heat Transfer. Journal of Heat Transfer, 138(1), 1–9. https://doi.org/10.1115/1.4031207

[42] Zhang, Z.-B., & Xu, Z.-M. (2010). Experimental Investigation of the Applied Performance of Several Typical Enhanced Tubes. Journal of Enhanced Heat Transfer, 17(4), 331–341. https://doi.org/10.1615/jenhheattransf.v17.i4.40

[43] Manca, O., Nardini, S., & Ricci, D. (2011). Numerical Analysis of Water Forced Convection in Channels with Differently Shaped Transverse Ribs. Journal of Applied Mathematics, 2011, 1–25. https://doi.org/10.1155/2011/323485

[44] Mohammed, H. A., Abbas, A. K., & Sheriff, J. M. (2013). Influence of geometrical parameters and forced convective heat transfer in transversely corrugated circular tubes. International Communications in Heat and Mass Transfer, 44, 116–126. https://doi.org/10.1016/j.icheatmasstransfer.2013.02.005

[45] Dong, J., Chen, J., Zhang, W., & Hu, J. (2010). Experimental and numerical investigation of thermal -hydraulic performance in wavy fin-and-flat tube heat exchangers. Applied Thermal Engineering, 30(11–12), 1377–1386. https://doi.org/10.1016/j.applthermaleng.2010.02.027

[46] Stel, H., Franco, A. T., Junqueira, S. L. M., Erthal, R. H., Mendes, R., Gonçalves, M. A. L., & Morales, R. E. M. (2012). Turbulent Flow in D-Type Corrugated Pipes: Flow Pattern and Friction Factor. Journal of Fluids Engineering, 134(12), 121–202. https://doi.org/10.1115/1.4007899

[47] Li, X., Meng, J., & Li, Z. (2011). Roughness enhanced mechanism for turbulent convective heat transfer. International Journal of Heat and Mass Transfer, 54(9–10), 1775–1781. https://doi.org/10.1016/j.ijheatmasstransfer.2010.12.039

[48] Meng, J.-A., Liang, X.-G., Chen, Z.-J., & Li, Z.-X. (2005). Experimental study on convective heat transfer in alternating elliptical axis tubes. Experimental Thermal and Fluid Science, 29(4), 457–465. https://doi.org/10.1016/j.expthermflusci.2004.04.006

[49] Khoeini, D., Akhavan-Behabadi, M. A., & Saboonchi, A. (2012). Experimental study of condensation heat transfer of R-134a flow in corrugated tubes with different inclinations. International Communications in Heat and Mass Transfer, 39(1), 138–143. https://doi.org/10.1016/j.icheatmasstransfer.2011.09.011

[50] Rozzi, S., Massini, R., Paciello, G., Pagliarini, G., Rainieri, S., & Trifirò, A. (2007). Heat treatment of fluid foods in a shell and tube heat exchanger: Comparison between smooth and helically corrugated wall tubes. Journal of Food Engineering, 79(1), 249–254. https://doi.org/10.1016/j.jfoodeng.2006.01.050

[51] Vicente, P. G., García, A., & Viedma, A. (2004). Experimental investigation on heat transfer and frictional characteristics of spirally corrugated tubes in turbulent flow at different Prandtl numbers. International Journal of Heat and Mass Transfer, 47(4), 671–681. https://doi.org/10.1016/j.ijheatmasstransfer.2003.08.005

[52] Harleß, A., Franz, E., & Breuer, M. (2017). Heat transfer and friction characteristics of fully developed gas flow in cross-corrugated tubes. International Journal of Heat and Mass Transfer, 107, 1076–1084. https://doi.org/10.1016/j.ijheatmasstransfer.2016.10.129

[53] Stel, H., Morales, R. E. M., Franco, A. T., Junqueira, S. L. M., Erthal, R. H., & Gonçalves, M. A. L. (2010). Numerical and Experimental Analysis of Turbulent Flow in Corrugated Pipes. Journal of Fluids Engineering, 132(7), 071–203. https://doi.org/10.1115/1.4002035

[54] Zachár, A. (2010). Analysis of coiled-tube heat exchangers to improve heat transfer rate with spirally corrugated wall. International Journal of Heat and Mass Transfer, 53(19–20), 3928–3939. https://doi.org/10.1016/j.ijheatmasstransfer.2010.05.011

[55] Hærvig, J., Sørensen, K., & Condra, T. J. (2017). On the fully-developed heat transfer enhancing flow field in sinusoidally, spirally corrugated tubes using computational fluid dynamics. International Journal of Heat and Mass Transfer, 106, 1051–1062. https://doi.org/10.1016/j.ijheatmasstransfer.2016.10.080

[56] Wu, G., Song, J. H., Chen, J. F., & Deng, C. Q. (2014). Research on Waste Heat Recovery and Utilization of Hydrogen Production Industry Based on Heat Pipe Heat Exchanger Technology. Advanced Materials Research, 1033–1034, 1362–1365. https://doi.org/10.4028/www.scientific.net/amr.1033-1034.1362

[57] Sivakumar, K., Rajan, K., Mohankumar, T., & Naveenchnadran, P. (2020). Analysis of heat transfer characteristics with triangular cut twisted tape (TCTT) and circular cut twisted tape (CCTT) inserts. Materials Today: Proceedings, 22, 375–382. https://doi.org/10.1016/j.matpr.2019.07.212

[58] F. P. Incropera, D. P. DeWitt, Introduction to heat transfer, Fourth Edition, ISBN:0-471-38649-9.

[59] Piriyarungrod, N., Eiamsa-ard, S., Thianpong, C., Pimsarn, M., & Nanan, K. (2015). Heat transfer enhancement by tapered twisted tape inserts. Chemical Engineering and Processing: Process Intensification, 96, 62–71. https://doi.org/10.1016/j.cep.2015.08.002

[60] Wang, W., Zhang, Y., Li, B., & Li, Y. (2018). Numerical investigation of tube-side fully developed turbulent flow and heat transfer in outward corrugated tubes. International Journal of Heat and Mass Transfer, 116, 115–126. https://doi.org/10.1016/j.ijheatmasstransfer.2017.09.003

[61] Webb, R. L. (1981). Performance evaluation criteria for use of enhanced heat transfer surfaces in heat exchanger design. International Journal of Heat and Mass Transfer, 24(4), 715–726. https://doi.org/10.1016/0017-9310(81)90015-6

[62] Zhang, C., Wang, D., Ren, K., Han, Y., Zhu, Y., Peng, X., Deng, J., & Zhang, X. (2016). A comparative review of self-rotating and stationary twisted tape inserts in heat exchanger. Renewable and Sustainable Energy Reviews, 53, 433–449. https://doi.org/10.1016/j.rser.2015.08.048

[63] Liu, D. C., & Nocedal, J. (1989). On the limited memory BFGS method for large scale optimization. *Mathematical Programming*, *45*(1–3), 503–528. https://doi.org/10.1007/bf01589116

[64] Trung, L. H. (2019). https://euroasia-science.ru/pdf-arxiv/the-controllability-function-of-polynomial-for-descriptor-systems-23-31/. *Eurasian Union Scientists*, *4*(65). https://doi.org/10.31618/esu.2413-9335.2019.4.65.275

[65] Xie, G., Wang, Q., Zeng, M., & Luo, L. (2007). Heat transfer analysis for shell-and-tube heat exchangers with experimental data by artificial neural networks approach. *Applied Thermal Engineering*, *27*(5–6), 1096–1104. https://doi.org/10.1016/j.applthermaleng.2006.07.036

[66] Ermis, K., Erek, A., & Dincer, I. (2007). Heat transfer analysis of phase change process in a finned-tube thermal energy storage system using artificial neural network. *International Journal of Heat and Mass Transfer*, *50*(15–16), 3163–3175. https://doi.org/10.1016/j.ijheatmasstransfer.2006.12.017

[67] Ermis, K., Erek, A., & Dincer, I. (2007b). Heat transfer analysis of phase change process in a finned-tube thermal energy storage system using artificial neural network. *International Journal of Heat and Mass Transfer*, *50*(15–16), 3163–3175. https://doi.org/10.1016/j.ijheatmasstransfer.2006.12.017

[68] Islam, M., Thakur, M. S. H., Mojumder, S., & Hasan, M. N. (2021). Extraction of material properties through multi-fidelity deep learning from molecular dynamics simulation. *Computational Materials Science*, *188*, 110187. https://doi.org/10.1016/j.commatsci.2020.110187

[69] Xie, G., Wang, Q., Zeng, M., & Luo, L. (2007b). Heat transfer analysis for shell-and-tube heat exchangers with experimental data by artificial neural networks approach. *Applied*

Thermal   Engineering,   27(5–6),   1096–1104.
https://doi.org/10.1016/j.applthermaleng.2006.07.036

[70] Sablani, S., Kacimov, A., Perret, J., Mujumdar, A., & Campo, A. (2005). Non-iterative
estimation of heat transfer coefficients using artificial neural network models. *International
Journal   of   Heat   and   Mass   Transfer*,   *48*(3–4),   665–679.
https://doi.org/10.1016/j.ijheatmasstransfer.2004.09.005

[71] Gupta, A., Kumar, P., Sahoo, R., Sahu, A., & Sarangi, S. (2016). Performance measurement
of plate fin heat exchanger by exploration: ANN, ANFIS, GA, and SA. *Journal of
Computational   Design   and   Engineering*,   *4*(1),   60–68.
https://doi.org/10.1016/j.jcde.2016.07.002

[72] Wang, Q., Xie, G., Zeng, M., & Luo, L. (2006). Prediction of heat transfer rates for shell-
and-tube heat exchangers by artificial neural networks approach. *Journal of Thermal
Science*, *15*(3), 257–262. https://doi.org/10.1007/s11630-006-0257-6

[73] Kumra, A., Rawal, N., & Samui, P. (2013). Prediction of Heat Transfer Rate of a Wire-on-
Tube Type Heat Exchanger: An Artificial Intelligence Approach. *Procedia Engineering*, *64*,
74–83. https://doi.org/10.1016/j.proeng.2013.09.078

[74] Thibault, J., & Grandjean, B. P. (1991). A neural network methodology for heat transfer data
analysis. *International Journal of Heat and Mass Transfer*, *34*(8), 2063–2070.
https://doi.org/10.1016/0017-9310(91)90217-3

[75] Verma, T. N., Nashine, P., Singh, D. V., Singh, T. S., & Panwar, D. (2017). ANN:
Prediction of an experimental heat transfer analysis of concentric tube heat exchanger with
corrugated   inner   tubes.   *Applied   Thermal   Engineering*,   *120*,   219–227.
https://doi.org/10.1016/j.applthermaleng.2017.03.126

[76] Manjula, D. R., Murugesan, P., Venkatesan, M., Keerthika, P., Sudha, K., Kannan, J., &
Suresh, P. (2021). Development of MLP-ANN model to predict the Nusselt number of plain
swirl tapes fixed in a counter flow heat exchanger. Materials Today: Proceedings. Published.
https://doi.org/10.1016/j.matpr.2021.04.433

[77] Aasi, H. K., & Mishra, M. (2021). Experimental investigation and ANN modelling on
thermo-hydraulic efficacy of cross-flow three-fluid plate-fin heat exchanger. *International
Journal   of   Thermal   Sciences,   164*,   106870.
https://doi.org/10.1016/j.ijthermalsci.2021.106870

[78] Liu, P., Kandasamy, R., & Wong, T. (2021). Experimental study and application of an
artificial neural network (ANN) model on pulsed spray cooling heat transfer on a vertical
surface.   Experimental   Thermal   and   Fluid   Science,   123,   110347.
https://doi.org/10.1016/j.expthermflusci.2021.110347

[79] McCulloch, W. S., & Pitts, W. (1943). A logical calculus of the ideas immanent in nervous activity. *The Bulletin of Mathematical Biophysics*, *5*(4), 115–133. https://doi.org/10.1007/bf02478259

[80] Cornell Aeronautical Laboratory, Inc. (1957). *Journal of Jet Propulsion*, *27*(2), 22. https://doi.org/10.2514/8.12665

[81] https://deepai.org/machine-learning-glossary-and-terms/sigmoid-function

[82] Normal Equations. (2008). *The Concise Encyclopedia of Statistics*, 380–382. https://doi.org/10.1007/978-0-387-32833-1_286

[83] Souayeh, B., Bhattacharyya, S., Hdhiri, N., & Waqas Alam, M. (2021). Heat and Fluid Flow Analysis and ANN-Based Prediction of A Novel Spring Corrugated Tape. *Sustainability*, *13*(6), 3023. https://doi.org/10.3390/su13063023

[84] Bhattacharyya, S.; Sarkar, D.; Roy, R.; Chakraborty, S.; Goel, V.; Almatrafi, E. (2021) Application of New Artificial Neural Network to Predict Heat Transfer and Thermal Performance of a Solar Air-Heater Tube. *Sustainability*, 13, 7477. https://doi.org/10.3390/su13137477

[85] Nasr, M. R. J., & Khalaj, A. H. (2010). Heat Transfer Coefficient and Friction Factor Prediction of Corrugated Tubes Combined with Twisted Tape Inserts Using Artificial Neural Network. *Heat Transfer Engineering*, *31*(1), 59–69. https://doi.org/10.1080/01457630903263440